Fachbereich 1
(Physik/Elektro- und Informationstechnik)

Applications of Earth's Field NMR to porous systems and polymer gels

Maarten Veevaete

Gutachter: Prof. Dr. J. Bleck-Neuhaus
Dr. habil. F. Stallmach

Eingereicht am 06.10.2008
Tag des mündliches Kolloqiums: 09.12.2008

Dissertation zur Erlangung des Grades
eines Doktors der Naturwissenschaften (Dr. rer. nat.)

Abstract

In this work, NMR relaxometry in the Earth's magnetic field is used to characterize porous systems and polymer gels. The used instrument is a home built Earth's field NMR (EFNMR) device (Goedecke [1993]) that is slightly modified for those applications. The EFNMR device is equipped with some unique features such as first order gradiometer polarization and detection coils, shimming coils and a shielding box that make it possible to directly derive the relaxation times from the Free Induction Decay (FID) signal inside a laboratory building with a signal to noise ratio of about 100. The strength of the Earth's magnetic field is about 50 μT, corresponding with Larmor frequencies of about 2 kHz. The experimental setup applying the measurement method of Packard and Varian [1954] using pre-polarization, compensates for the inherent low signal to noise ratio of NMR in the Earth's magnetic field. By the use of the field-cycling technique, the EFNMR device is also capable of measuring the longitudinal relaxation time at frequencies from 3 kHz up to 3 MHz.

With the EFNMR device it is possible to determine the transversal and longitudinal relaxation times of different kind of systems where the effect of the internal inhomogeneity is negligible, i.e. for samples with low amounts of paramagnetic impurities. A custom software allows flexible measurement controlling and advanced data analysis. Depending on the sample characteristics, the analysis of the decay of the measured FID envelope can be done by a model with a few discrete relaxation time constants or by a continuous distribution of relaxation times using the inverse Laplace transformation.

Different kinds of experiments show the dexterity of the EFNMR device in a broad range of applications. Since the signal amplitude depends linearly on the amount of protons in the sample, the water content of different kinds of samples can be determined in a very accurate way. By continuously determining the signal amplitude during drying experiments, the drying behavior of porous systems can be obtained easily and in non-invasive way and theoretical models describing the drying process are experimentally confirmed. From the analysis of the relaxation times, information about the environment of the protons is derived. Since the relaxation times of protons confined in porous material depend on the pore size, the relaxation time distribution can be used to characterize the pore structure. The pore size distributions

obtained by the non-destructive Earth's Field NMR relaxometry method are very similar to the data obtained from mercury intrusion porosimetry experiments. Due to the fact that the extra transversal decay due to internal inhomogeneities is not compensated by the method used in this work, the characterization of porous systems is only possible for samples with low amounts of paramagnetic impurities.

In a similar way as for porous systems, the protons of fluids surrounding polymer molecules depend on the polymer structure. Therefore, the analysis of the relaxation times of the surrounding fluid gives information about the polymer structure and about the processes playing a role in the polymerization reaction (e.g. irradiation processes inducing radical polymerization). The dependence of the relaxation time of gelous polymeric systems on the irradiation time is used for clinical gel dosimetry applications. For those experiments with polymer gels, the increased sensitivity due to the increased relaxation at low fields, shows to be a big advantage in comparison to high field applications.

Contents

Acknowledgments

Writing this thesis would not have been possible without the support of many people. I would like to express my thanks to:

Dr. Helmut Fischer for offering me the possibility to work on this project and for his guidance and help, also beyond the scientific aspects of this work. It has been a pleasure to be a member of his group for more than 3 years.

Prof. Dr. Jörn Bleck-Neuhaus and Dr. habil. Frank Stallmach for their detailed review and constructive criticism.

Dr. Rolf Goedecke for his catching enthusiasm about this project and for the many hours of technical support. Especially the many late-night brainstorm sessions were very motivating.

Dr. Volker Hormann for his theoretical support and expertise and for his numerous inspiring ideas.

Dr. Michaela Wilhelm for providing the silica gel samples and the freeze cast samples together with the scanning electron microscopy images and mercury intrusion porosimetry data.

Regine Braatz for her assistance in the chemical laboratory.

Bernd Hettwig for the nice working atmosphere, for organizing many sport activities and for the enjoyable time I had during my work in the radioactivity lab.

All the other members of the Terrestrial Environmental Physics group for providing such a pleasant working environment.

Jana Steinig for her support, confidence and everything else.

Chapter 1

Introduction

Since the first nuclear magnetic resonance (NMR) experiments by Bloch et al. [1946] and Purcell et al. [1946], for which they received the Nobel Prize in Physics in 1952, NMR has become a standard measurement tool in a broad range of scientific applications. Three different kinds of NMR applications can be distinguished: spectroscopy, tomography and relaxometry.

- Because every type of nucleus possessing the property of spin has a specific resonance frequency, NMR can be used for *spectroscopy*. The exact resonance frequency depends on the chemical environment of the nuclei, e.g. the chemical substituents. Therefore, NMR spectroscopy can be applied to obtain structural information about the molecules in the sample. For his contributions to the development of the methodology of NMR spectroscopy, R. Ernst received the Nobel Prize in Chemistry in 1991.

- By manipulating the spatial dependence of the magnetic induction and the frequency of the RF excitation, the NMR sensitive region within a voluminous sample can be varied. This provides a noninvasive measurement of the spatial distribution of a certain nucleus and its relaxation behavior and is called Magnetic Resonance Imaging (MRI) or *NMR tomography*. For their discoveries concerning magnetic resonance imaging, P. Mansfield and P. Lauterbur were awarded the Nobel Prize in Physiology or Medicine in 2003.

- In *NMR relaxometry*, the time constants of the magnetization decay itself are the subjects of interest. Those time constants will depend on the physical and chemical environment of the nuclei. Studying those relaxation times will therefore give information about the environment of the nuclei. Soon after the first NMR experiments, it was noticed that liquids confined in porous materials exhibit properties that are very different from those of the bulk fluid. The so-called longitudinal (T_1) and transversal (T_2) relaxation times of bulk fluids (e.g. water) can be up to three order of magnitudes larger than the relaxation times for the same fluid confined in porous materials. NMR relaxometry is

not limited to porous systems but can be applied on all kinds of (heterogeneous) systems containing nuclei that possess the property of spin.

In all three application fields, there has been a continuous trend for (super conducting) magnets that deliver ever-higher magnetic field strengths with excellent homogeneities to achieve higher resolution, chemical-shift dispersion, and sensitivities. Whether this aspiration is expedient, or if one could also do with much lower magnetic field strengths, depends strongly on the kind of application (Thiele [2007]). For spectroscopy applications, ultra low fields will be disadvantageous since the chemical shift, which results from a small change in the resonance frequency by local magnetic fields within the molecule, depends on the magnetic field strength, leading to hardly resolved chemical shifts in fields having the order of magnitude of the Earth's magnetic field. In imaging and relaxometry applications the inherent lower signal to noise ratio, will be the main drawback of using ultra low fields. However, the use of ever-stronger magnetic fields also brings along some important disadvantages, mainly high technical and financial expenses.

Despite its low cost and relatively moderate technical complexity, ultra low field NMR, and in particularly Earth's field NMR (EFNMR), is still an exotic branch in the broad range of NMR applications. Compared with the huge amount of literature about all kinds of high field NMR applications, research in the ultra low field is limited. Some recent literature however, indicates a renewed interest in this research topic (e.g. Thiele [2007]; Stepisnik [2006]; Appelt et al. [2006]; Robinson et al. [2006]; Halse et al. [2006]).

The aim of this work is to investigate the possibilities of NMR relaxometry performed in the Earth's magnetic field in the study of porous and gelous systems. It will be proved that for some applications, EFNMR relaxometry can be a complementary tool next to high field NMR methods. By an appropriate experimental setup the main drawback of using low magnetic fields, i.e. the low signal to noise ratio, can be canceled out and a signal to noise ratio comparable with high field applications can be obtained. The advantages and disadvantages, limitations and possibilities of this technique to analyze porous and gelous systems will be discussed in detail. The possibilities given by the advantages of very low fields, such as the low magnetic susceptibility differences in porous systems and the increased efficiency of dipolar relaxation due to the increased spectral amplitude of molecular motion at low Larmor frequencies, will be explored in order to find potential practical applications of Earth's field NMR relaxometry.

This work is organized in the following sections:

- The general NMR principles are explained in chapter 2. Particularly the theory relevant for the measurement method used in this work is covered. Also the general principles of relaxation in porous media are explained. A short overview of some theoretical models

from the literature is presented and the relation between the relaxation times and certain pore characteristics is described.

- A description of the Earth's field NMR method is given in chapter 3. After a brief description of the Earth's magnetic field itself, the specific characteristics of EFNMR, as well as the advantages and disadvantages are explained in some detail. Also the different components of the EFNMR measuring device used in this work are described in this chapter, especially those components diverging from the original design given in Goedecke [1993].

- Chapter 4 covers the mathematical background of the data analysis. The problems arising when deriving the relaxation times from the measurement data are explained in detail and possible solutions are given. Various analysis methods are validated and their reproducibility is tested.

- Chapter 5 shows the results of two different sets of EFNMR experiments and their applications to material analysis and gel dosimetry. The first set uses the amplitude of the NMR signal for the derivation of the fluid content of various samples. It is shown that it is possible to characterize the drying behavior of porous systems by analyzing the temporal variation of the fluid content via EFNMR. The relaxation times of fluids in various porous media are studied in the second set of experiments. These data are used to derive the pore size distribution of some porous materials. In the last section, the relaxation times of certain polymer gels after irradiation are studied. The usefulness of this method for dosimetric purposes is demonstrated.

- This work ends with the conclusions and outlook in chapter 6.

Chapter 2

NMR principles

In the first section of this chapter general principles of NMR are briefly explained. More detailed information can be found in text books such as Abragam [1973]; Fukushima and Roeder [1981]; Farrar and Becker [1974]. Especially topics related to NMR experiments performed in low magnetic fields will be treated in more detail. The second section contains the general theory about relaxation as well as some models explaining the relaxation behavior in porous systems.

2.1 General NMR principles

The nuclear magnetic moment is a quantum mechanical property of a nucleus. Due to quantum mechanical behavior, the properties of a single nucleus have to be characterized by states which belong to a discrete set of possibilities. However, when we are performing NMR experiments, we deal with exceedingly large numbers of nuclei acting largely independently, so that at the macroscopic level the observable quantities appear to be continuous.

All nuclei with odd and some nuclei with even mass number (e.g. ^{2}H) possess the property of spin. The spin angular momentum vector $\vec{S}$ can be expressed by the spin vector $\vec{I}$ in units of $\hbar$:

$$\vec{S} = \hbar \cdot \vec{I} \tag{2.1}$$

The size of the angular momentum is equal to

$$S = |\vec{S}| = \hbar \cdot \sqrt{I \cdot (I+1)} \tag{2.2}$$

The value of the spin quantum number I is an integral multiple of $\frac{1}{2}$. Under the influence of an external magnetic induction $\vec{B}_0 = \mu_0 \cdot \vec{H}_0$, a nucleus with a magnetic moment $\vec{\mu}$ and spin quantum number I can have $2I+1$ discrete energy states. For nuclei with spin quantum number $\frac{1}{2}$ (such as protons) the following energy states are possible: $I_+ = +\frac{1}{2}$ and $I_- = -\frac{1}{2}$.

Spin and magnetic moment are related as follows:

$$\vec{\mu} = \gamma \cdot \hbar \cdot \vec{I} \tag{2.3}$$

where γ is the gyromagnetic ratio of the nucleus. For protons this ratio is equal to:

$$\frac{\gamma}{2\pi} = 42,577 \ \frac{\text{MHz}}{\text{T}} \tag{2.4}$$

In the case of independent nuclei with quantum number $\frac{1}{2}$, such as protons, no quadrupole interactions are possible. In this case the motion of the ensemble of spins may always be described in terms of the precession of the magnetization vector about the field with a frequency f_L, the Larmor frequency

$$\vec{f_L} = -\frac{\gamma}{2\pi} \cdot \vec{B}_0 \tag{2.5}$$

In order to induce transitions between the two nuclear spin levels of the proton, an energy quantum has to be exchanged with the environment:

$$\Delta E = (I_+ - I_-) \cdot \hbar \cdot \omega_L = h \cdot f_L \tag{2.6}$$

A system containing N spins in the absence of an external magnetic field will have the same number of I_+ spins (N_+) and I_- spins (N_-). In the presence of an external magnetic field the distribution of spins over the two possible states is governed by the Boltzmann law:

$$\frac{N_+}{N_-} = e^{\frac{\Delta E}{kT}} = e^{\frac{\mu \cdot B_0}{kT}} \tag{2.7}$$

At ordinary temperatures and magnetic induction $B_0 << \frac{kT}{\mu}$, and Eq. 2.7 can be approximated by:

$$\frac{N_+}{N_-} \approx 1 + \frac{\mu \cdot B_0}{kT} \tag{2.8}$$

The populations of the spin states are almost equal and a simple calculation shows that

$$N_+ = \frac{N}{2} \cdot (1 + \frac{\mu \cdot B_0}{kT}) \tag{2.9}$$

$$N_- = \frac{N}{2} \cdot (1 - \frac{\mu \cdot B_0}{kT}) \tag{2.10}$$

and therefore we can write

$$N_+ - N_- = N \cdot \frac{\mu \cdot B_0}{kT} \tag{2.11}$$

Multiplying with the magnitude of the magnetic moment of a nucleus, we get the macroscopic magnetic moment M for N nuclei:

$$M = \mu \cdot (N_+ - N_-) \tag{2.12}$$

$$M = N \cdot \frac{\mu^2 \cdot B_0}{kT} \tag{2.13}$$

When $N = \rho_N \cdot V$ (with ρ_N the density of the nuclei in the sample material), the average magnetization in a volume V can be written as:

$$H = \frac{M}{V} = \frac{\rho_k \cdot \mu^2 \cdot B_0}{kT} \tag{2.14}$$

and the static magnetic succeptibility χ_0 can be written as:

$$\chi_0 = \frac{H}{H_0} = \frac{\rho_k \cdot \mu^2 \cdot \mu_0}{kT} = \frac{\rho_k \cdot \gamma^2 \cdot \hbar^2 \cdot \mu_0}{4 \cdot kT} \tag{2.15}$$

The macroscopic magnetic induction of an ensemble of nuclei in equilibrium is then

$$\vec{B}_k = \chi_0 \cdot \vec{B}_0 \tag{2.16}$$

For water at room temperature $\chi_0 \approx 4 \cdot 10^{-9}$.

On a macroscopic scale all the spin moments of an ensemble of nuclei add up to a magnetization vector

$$\vec{M} = \sum_i \vec{\mu}_i \tag{2.17}$$

so that we can write Eq. 2.3 as:

$$\vec{M} = \gamma \cdot \vec{L} \tag{2.18}$$

where $\vec{L}$ describes the macroscopic angular momentum.

Applying the theorem of the preservation of angular momentum to the resultant angular momentum of nuclear spins per unit volume of the sample

$$\frac{d\vec{L}}{dt} = \vec{T} = \vec{M} \times \vec{B}_0, \tag{2.19}$$

we get:

$$\frac{d\vec{M}}{dt} = \gamma \cdot (\vec{M} \times \vec{B}_0) \tag{2.20}$$

The solution of this equation corresponds to a precession of the magnetization vector about the field at rate $\omega_0 = \gamma B_0$ (see figure 2.1).

The resonance phenomenon results on application of a transverse magnetic induction $\vec{B}_1$ oscillating at ω_0. This resonant r.f. pulse disturbs the spin system from its thermal equilibrium state. The angle of rotation of $\vec{M}_0$ due to the resonance pulse can be written as:

$$\theta = -\gamma \cdot \int_0^t B_1 \mathrm{dt} \tag{2.21}$$

Most NMR devices at high magnetic fields use this pulse technique to disturb the equilibrium magnetization (e.g. 90° pulse) after which the precessing magnetic induction vector can be detected. But also adding a static magnetic induction $\vec{B}_p$ in a different direction than $\vec{B}_0$ (e.g. orthogonal to $\vec{B}_0$) can bring the magnetization vector out the equilibrium state. After

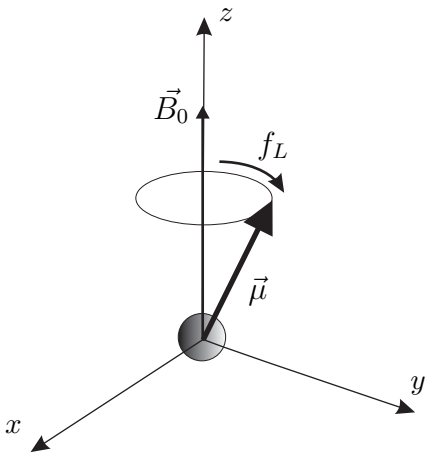

Figure 2.1: The nuclear magnetic moment of a nucleus precessing around $\vec{B}_0$ with the Larmor frequency f_L

polarizing the spins for a sufficiently long time, the nuclei will take their new equilibrium orientation and the induction vector will point in the direction of the vector sum of $\vec{B}_p$ and $\vec{B}_0$ with a magnitude proportional to $\vec{B}_p$ (see Eq. 2.16).

When the magnitude of $\vec{B}_p$ is chosen to be much larger than the magnitude of $\vec{B}_0$, this static magnetic induction not only brings the original magnetic induction out of the equilibrium state, but also increases the magnetic induction, leading to an increased signal amplitude and a higher signal to noise ratio (see section 3.1). Therefore, this method is very suitable for NMR experiments performed in the weak Earth's magnetic field. Packard and Varian [1954] were the first to perform such an experiment and it is this method that we will use in this work.

Although the method used in this work does not use the resonance phenomena (there is no external field oscillating at the Larmor frequency), we still use the term *Nuclear Magnetic Resonance* because it has become a general notation for a broad field of applications where magnetic induction of an ensemble of nuclei plays a role but in which the resonance phenomenon is not necessarily involved.

2.2 Relaxation

2.2.1 General relaxation principles

After excitation by a resonant pulse (in traditional high field NMR applications) or a static magnetic induction (in this work), the spin system will be disturbed from its equilibrium

state. The equilibrium will be restored by a process known as *relaxation*. The *longitudinal relaxation* describes the restoration of the magnetization $\vec{M}_0$ in the direction of the longitudinal magnetic induction $\vec{B}_0$. During this restoration, energy is exchanged between the spin system and the surrounding thermal reservoir, known as *lattice*, with which it is in equilibrium. The longitudinal relaxation is therefore alternatively named *spin-lattice relaxation*. The phenomenological description of this process is given by the equation (Bloch et al. [1946])

$$\frac{\mathrm{d}M_z}{\mathrm{d}t} = -\frac{1}{T_1}(\vec{M}_z - \vec{M}_z e) \tag{2.22}$$

with solution

$$M_z(t) = M_{ze} + (M_z(0) - M_{ze}) \cdot \exp(-\frac{t}{T_1}), \tag{2.23}$$

where $M_z(0)$ represents the magnetization at $t = 0$ and M_{ze} represents the magnetization at equilibrium ($t = \infty$). T_1 is known as the spin-lattice or longitudinal relaxation time.

Simultaneously with the longitudinal relaxation process, the spins also lose their coherence and the magnetization transverse to the direction of $\vec{B}_0$ decays. This process is described by the *transversal relaxation* time. During the transversal relaxation the spins come to thermal equilibrium among themselves and is also named *spin-spin relaxation*. While indirect energy exchange via the lattice may play a role, additional processes can also be responsible for the transversal relaxation. This leads to the result $T_2 \leq T_1$. Because transverse magnetization corresponds to a state of phase coherence between the nuclear spin states, the transverse relaxation, unlike longitudinal relaxation, is sensitive to interaction terms which cause the nuclear spins to dephase (such as field inhomogeneity, see section 2.3). The phenomenological description of transversal relaxation is given by the equation

$$\frac{\mathrm{d}M_{x,y}}{\mathrm{d}t} = -\frac{1}{T_2}(\vec{M}_{x,y}), \tag{2.24}$$

with solution

$$M_{x,y}(t) = M_{x,y}(0) \cdot \exp(-\frac{t}{T_2}) \tag{2.25}$$

Combining equations (2.20), (2.22) and (2.24) yields a set of equations known as the *Bloch equations* (Bloch et al. [1946]), in Cartesian coordinates with z the direction of $\vec{B}_0$:

$$\frac{\mathrm{d}M_x}{\mathrm{d}t} = \gamma \cdot (M_y B_z - M_z B_y) - \frac{1}{T_2} \cdot M_x \tag{2.26}$$

$$\frac{\mathrm{d}M_y}{\mathrm{d}t} = \gamma \cdot (M_z B_x - M_x B_z) - \frac{1}{T_2} \cdot M_y \tag{2.27}$$

$$\frac{\mathrm{d}M_z}{\mathrm{d}t} = \gamma \cdot (M_x B_y - M_y B_x) - \frac{1}{T_1} \cdot (M_z - M_{ze}) \tag{2.28}$$

The magnitudes of T_1 and T_2 depend on the interactions between the nuclei and their effective local magnetic environment in the sample, and therefore also on sample material, temperature and static magnetic induction. Because of the dependence of the sample material, NMR can

be used to characterize different media. This very important property will be used in this work and further explained in the next chapters. The temperature dependence makes it necessary to maintain constant temperature during the measurement and will lead to some restrictions for the experimental setup (see section 3.4.1.5). The dependence of the relaxation times on the static magnetic induction is a result of the fact that an energy quantum can only be exchanged between the nucleus and the environment when the right energy amount ΔE appears in the molecular translation-rotation spectrum (see Eq. 2.6).

The Bloembergen-Purcell-Pound (BPP) theory (Bloembergen et al. [1948]) explains the relaxation characteristics of simple systems such as bulk water in function of a correlation time τ_c, the Larmor frequency ω_0 and the distance r between the nuclei:

$$\frac{1}{T_1} = \frac{3}{10}\frac{\gamma^4\hbar^2}{r^6}\left[\frac{\tau_c}{1+\omega_0^2\tau_c^2} + \frac{4\tau_c}{1+4\omega_0^2\tau_c^2}\right] \tag{2.29}$$

$$\frac{1}{T_2} = \frac{3}{20}\frac{\gamma^4\hbar^2}{r^6}\left[3\tau_c + \frac{5\tau_c}{1+\omega_0^2\tau_c^2} + \frac{2\tau_c}{1+4\omega_0^2\tau_c^2}\right] \tag{2.30}$$

The correlation time τ_c describes the time a nucleus has to interact with a nucleus of a neighboring molecule, before it diffuses or rotates away by thermal motion of the corresponding molecules. For liquids this time is about 10^{-12} s and for solids it is about 10^{-5} s. In a relaxation dispersion diagram the relaxation rates ($R = \frac{1}{T}$) are represented in function of the magnetic induction B or the Larmor frequency f_L. By analyzing the field dependence of the relaxation times, information about the molecular dynamics of the system can be derived.

2.2.2 Relaxation in porous media

There are several physical mechanisms forming the basis of relaxation such as dipolar, quadrupolar and magnetic coupling, spin rotation, etc. For simple systems containing protons, the dipole-dipole interaction is the most important relaxation mechanism. This interaction depends on the strength of the dipolar coupling (depends on γ), on the orientation/distance between the interacting nuclei and on the motion (see Eqn. 2.29 and 2.30).

In bulk water at room temperature, the longitudinal and transversal relaxation times will be in the order of a few seconds ($T_1 \approx 2.4$ s, $T_2 \approx 1.8$ s). However, the relaxation times for water confined in the pore space of a porous medium will be much shorter, due to the additional interaction of the protons at the pore-grain interface with paramagnetic impurities in the grains and the hindered motion of the water molecule in the layer adjacent to the pore-grain interface (Wilkinson et al. [1991]). The strength of the surface relaxation is assumed to be constant and is characterized by the *surface relaxivity* ρ (with dimension [m/s]) which is equal to the product of a fluid-surface relaxation rate ($1/T_s$) and the thickness (λ) of the fluid layer

interacting with the surface:

$$\rho = \frac{\lambda}{T_{\text{surface}}} \tag{2.31}$$

The theoretical models describing the relaxation mechanisms of fluids confined in porous systems are based on the work of Brownstein and Tarr [1979] who described the relaxation in biological cells. The decay of nuclear magnetization due to surface relaxation depends upon both ρ and the self-diffusion coefficient D of the fluid:

$$\frac{\partial M}{\partial t} = D\nabla^2 M - \frac{M}{T_B} \tag{2.32}$$

with the boundary condition

$$[D\hat{n} \cdot \nabla M + \rho M]_{\text{surface}} = 0, \tag{2.33}$$

with T_B the bulk relaxation time of water and $\hat{n}$ the unit normal pointing toward the grain at the pore-grain interface. The solution of the diffusion problem can be expressed as a sum of normal modes

$$M(t) = \sum_{n=0}^{\infty} A_n e^{-t/T_n} \tag{2.34}$$

with the constraint that $M(0) = \sum_n A_n$.

Brownstein and Tarr [1979] showed that this equation can be solved for simple geometries with a characteristic pore size a (with dimension [m]). Depending on the dimensionless parameter $\rho a/D$, the decay of the magnetization will be dominated by a relaxation time

$$T_{\text{surface}} = \begin{cases} \dfrac{a^2}{D}, & \dfrac{\rho a}{D} >> 1 \qquad \text{(slow diffusion region)} \\ \\ \dfrac{a}{\rho}, & \dfrac{\rho a}{D} << 1 \qquad \text{(fast diffusion region)} \end{cases} \tag{2.35}$$

In the *slow diffusion* region, the higher modes of Eq. 2.34 contribute significantly to the relaxation, meaning that although magnetic relaxation occurs at the grain surface, the decay of macroscopic magnetization is controlled by the transport of molecules to the surface. This is likely to be the case when pores are relatively large and/or surface relaxation is strong and results in a time-dependent nonuniform spatial distribution of magnetization in the pore. This gives rise to a magnetization decay which even in a single pore has multi-exponential character and which depends on the shape of the pore.

In the *fast diffusion* region the lowest mode dominates completely, meaning that the rate-limiting step is relaxation at the surface, not the transport of magnetization to the surface. The rate of magnetization decay in an individual pore is thereby mono-exponential and does not depend on pore shape but only on the surface to volume ratio. The time evolution of

the magnetization decay of a sample having a distribution of pore sizes can be expressed as a sum of exponential decays and there is a direct mapping from the spectrum of pore sizes, or more precisely the spectrum of surface to volume ratios, to the spectrum of relaxation times (Kleinberg et al. [1994]).

As shown in section 5.2, the fast diffusion region will be the region of interest for most samples in this work, and a can be replaced by V_p/S, the pore volume-surface ratio. This ratio will be different for each pore size. For spherical pores the ratio V/S is equal to $r/3$, in which r is the pore radius. For long cylindrical pores this ratio is equal to $r/2$. The value for the relaxivity ρ will be different for T_1 and T_2 and in general depends on the microscopic interactions that the protons feel at the pore-grain interface. Because the surface relaxation acts at the same time and independently of the bulk relaxation processes, we can write (for the fast diffusion limit):

$$\frac{1}{T} = \frac{1}{T_{\text{bulk}}} + \frac{1}{T_{\text{surface}}} = \frac{1}{T_{\text{bulk}}} + \rho\frac{S}{V} \tag{2.36}$$

When λ is the thickness of the fluid layer interacting with the surface (see figure 2.2) and by using Eq. 2.31, the previous equation can also be written as

$$\frac{1}{T} = \frac{1}{T_{\text{bulk}}} + \frac{\lambda S}{V}\frac{1}{T_{\text{surface}}}. \tag{2.37}$$

Eq. 2.36 to 2.37 can be written for the spin-spin relaxation time and the spin-lattice relaxation time each with a specific relaxivity ρ. The molecules in the inner part of the pore will behave like bulk until they reach the layer near the pore wall by diffusion. The liquid confined in pores is thus considered to coexist in two homogeneous phases characterized as *bulk-like* and *surface-ordered* (see figure 2.2). This bi-phasic system is in *fast exchange*, indicated by the mono-exponential relaxation and meaning that the time scale of the exchange process (defined by the mean exchange time $\tau_{s,b}$ between bulk-like phase and surface phase) is much faster than the relaxation times.

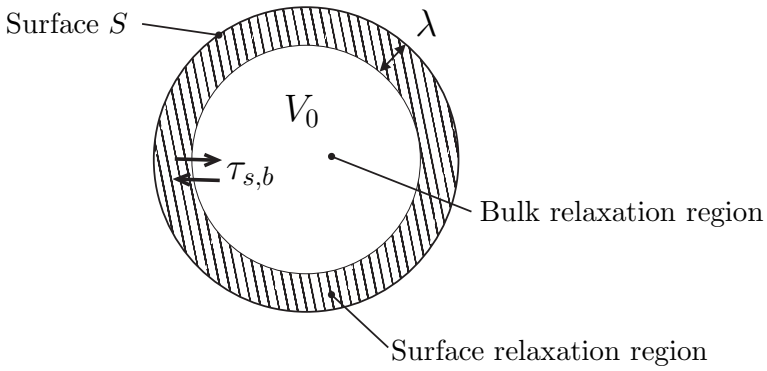

Figure 2.2: Schematic representation of a spherical pore filled with water. A layer of thickness λ of molecules will behave according to the surface relaxation. All other molecules will behave according to bulk relaxation. The exchange of protons between bulk and surface phase is characterised by the time constant $\tau_{s,b}$.

The exact mechanism for surface relaxation is not well understood and depends on material properties. It depends on the magnetic dipolar interaction of the liquid nuclei with magnetic dipoles near or at the liquid-solid interface. This surface interaction is probably related to the van der Waals force between liquid and solid at the interface that hinders the molecular dynamics (Halperin et al. [1989]). This mechanism would then be the intermolecular or intramolecular nuclear dipolar interaction. In many systems paramagnetic impurity sites on the surface are responsible. In this case the mechanism for surface relaxation is the interaction between nuclear dipole moments of the liquid molecules and the electronic dipole moments of paramagnetic entities on the surface.

Field-cycling NMR relaxometry has demonstrated to be a useful method to analyze the spin-lattice relaxation time mechanisms in porous systems (e.g. Kimmich [2002]). Mattea et al. [2004], Zavada and Kimmich [1998] and Stapf et al. [1995] proved that relaxation by electron paramagnetic impurities can be neglected for commercial porous glasses and silica fine particles. The comparison of proton and deuteron spin-lattice relaxation data and isotopic dilution experiments indicated that intramolecular dipolar interactions largely dominate surface proton relaxation. Spin-lattice relaxation is therefore predominantly caused by molecular reorientations, especially by *reorientations mediated by translational displacements* (RMTD) at the pore walls. Rotational diffusion plays a minor role since it tends to be so fast at room temperature that no direct contribution to the spin-lattice relaxation can be expected (Zavada and Kimmich [1998]).

The frequency dependence of the spin-lattice relaxation time can be explained by the RMTD mechanism in which molecules probe the surface topology via translational diffusion and molecular exchange (Mattea et al. [2004]). The orientation of a molecule adsorbed on the pore surface will depend on the surface topology. Those molecules may perform excursions

to the bulk-like medium in the pore space, where no preferential orientation exists. As soon as molecules return to the surface, they adopt the preferential surface orientation at this site. The correlation between the final and the initial orientation on the surface will therefore depend on the surface topology. The correlation function for the RMTD process thus implies dynamic as well as geometrical features of the system (Kimmich [2002]). The latter explains the pore size dependence on the spin-lattice relaxation time, while the former explains the Larmor frequency dependence, i.e. the T_1 dispersions.

Mattea et al. [2004] proved that additionally to the *fast relaxation exchange limit*, $T_1 >> \tau_{s,b}$, also the *slow correlation exchange limit*, $t_c << \tau_{s,b}$ (with t_c the characteristic time constant of the correlation function decay), is valid for the spin-lattice relaxation time of polar liquids in porous glasses. The longest orientation correlation components were observed to decay eight orders of magnitude more slowly than in the free liquid, meaning that many elementary diffusion steps are needed until a molecule totally looses the correlation to its initial orientation (Kimmich [2002]). These *slow dynamics* explain the T_1 dispersion at low frequencies and the assumption of those two exchange limits, leads to the following model for polar liquids in porous glasses:

$$\frac{1}{T_1(\omega)} = \frac{1}{T_{1,b}(\omega)} + \frac{\lambda S}{V_0}\left[\frac{1}{T_{1,s}(\omega)} - \frac{1}{T_{1,b}(\omega)}\right] \tag{2.38}$$

where $T_{1,s}(\omega)$ and $T_{1,b}(\omega)$ are the spin-lattice relaxation times selectively expected for the RMTD mechanism in the adsorbed layer and the rotational diffusion process in the bulk-like phase, respectively. By setting ρ equal to $\lambda\,(1/T_{1,s} - 1/T_{1,b})$ the general expression 2.36 is obtained again where ρ represents a phenomenological constant considered to be characteristic for the surface interaction (D'Orazio et al. [1989]).

Godefroy et al. [2001] showed by low field NMR that changing the amount of surface paramagnetic impurities leads to strikingly different pore-size dependences of the relaxation times T_1 and T_2 of liquids in pores. Based on the fast diffusion regime (surface-limited relaxation) of the biphasic fast exchange model, the overall proton spin-lattice relaxation rate in function of the Larmor frequency can be written as:

$$\frac{1}{T_1(\omega)} = \frac{1}{T_{1,b}} + \rho_1(\omega)\frac{S_p}{V_p} = \frac{1}{T_{1,b}} + \frac{N_s}{N}\frac{1}{T_{1,s}(\omega)} \tag{2.39}$$

The bulk contribution appears now to be frequency independent at low magnetic fields and all the frequency dependence comes from the surface contribution, where N_s/N represents the ratio of the pore surface to the total amount of water molecules.

2.2.3 Relaxation times and pore sizes

Equation 2.37 gives a relationship between the pore size and the relaxation rate. In order to find this relation several approaches are possible. Most methods combine the NMR data with

another independent method that measures some pore characteristics (r or S/V). Kleinberg [1996] determined the surface relaxivity from capillary pressure curves measured by mercury intrusion porosimetry (MIP). The injection pressure P of mercury into a cylindrical tube is related to the tube radius r:

$$P = 2\gamma \cos(\theta)/r \tag{2.40}$$

where γ is the surface tension and θ is the contact angle. Combining Eq. 2.36 and 2.40 and neglecting the bulk relaxation rate gives:

$$\rho_{1,2} = \frac{2}{3}\frac{\gamma \cos(\theta)}{P \cdot T_{1,2}} \tag{2.41}$$

However, this relation is only valid if the *pore throats*, the connection between two pores, have the same order of magnitude as the pores themselves. Fantazzini et al. [2003] showed that the pore size distribution found by NMR relaxometry can be quite different from the distribution found by mercury intrusion porosimetry due to the fact that in relaxation measurements *size* tends to correspond to pore dimensions, while in mercury intrusion porosimetry *size* corresponds to the dimensions of the pore *throats*, the channels connecting the pores. The discrepancy between both distributions will therefore depend on the structure of the pore system and both methods are thus complementary. If the system contains a lot of big pores connected with small throats, mercury intrusion porosimetry will only see the small throats, while NMR relaxometry will mainly see the big pores. For porous systems where the throats and the pores have about the same size, both measurement methods will give similar results.

The relaxivity parameter can also be determined by combining the relaxation data with scanning electron microscopy (SEM) imaging analysis. The latter method gives directly the surface to volume ratio. This value can be inserted in Eq. 2.36 from which ρ can then be determined.

There exist also some other methods that determine the surface relaxivity directly from NMR measurements. Slijkerman and Hofman [1998] describe a method that determines the surface relaxivity by combining restricted diffusion and T_2-relaxation: in an inhomogeneous field, the relaxation will also be influenced by the diffusion which is restricted by the pore size and independent of surface relaxivity. Therefore the relaxivity can be determined by changing the influence of the diffusion in the overall relaxation, for example by changing the inter-echo time in the Carr-Purcell-Meiboom-Gill pulse sequence (CPMG, see section 2.3) as shown by Slijkerman and Hofman [1998].

Due to the fact that natural materials are often mineralogically inhomogeneous, the rate of surface relaxation can vary from pore to pore. In this case, a distribution of relaxation times would reflect heterogeneities that are not necessarily correlated with pore size. Therefore it will be difficult to determine the pore size from the spectrum of relaxation times for very inhomogeneous systems. However, as shown in section 5.2, this technique is feasible for

homogeneous samples.

2.3 Field inhomogeneity

The general relaxation principles explained in section 2.2.1 are only valid in a perfectly homogeneous field. In an inhomogeneous field the precessing signal is not only altered due to relaxation but also due to the inhomogeneity of $\vec{B}_0$ in the sample. In an inhomogeneous field the static magnetic field strength will vary within the sample. To deal with this situation, the magnetization $\vec{M}$ can be decomposed into a sum of elementary magnetic moments associated with different volume elements of the sample. The transverse components of the elementary moments precess at slightly different rates, and therefore individually change their orientation with respect to each other. This dephasing of the elementary magnetic moments leads to a decrease of the total magnetization $\vec{M}$ and is an additional (and in strong inhomogeneous fields decisive) reason for the decay of the transverse magnetization.

The decay of the transverse magnetization due to the inhomogeneity will be significant if the partial magnetization coming from two points of the sample corresponding to the greatest difference ΔB in a field with value B, reach the difference in phase equal to π (i.e. complete dephasing) in a time that is comparable with the decay time of the transverse relaxation. E.g. when the complete dephasing occurs in a time equal to T_2, the signal will already have decayed completely after a time of one time constant in stead of being decreased with a factor of $1/e$ as is the case when the decay is only due to the relaxation. Complete dephasing in time T_2 occurs when

$$\omega = \frac{\pi}{T_2} \tag{2.42}$$

With $\Delta f_L = \dfrac{\omega}{2\pi}$, this can be written as:

$$\Delta f_L = \frac{1}{2T_2} \tag{2.43}$$

By substituting this expression in Eq. 2.5, the field inhomogeneity ΔB can be written as:

$$\Delta B = \frac{2\pi}{\gamma}\Delta f_L \tag{2.44}$$

For protons in water with $T_2 \approx 2$ s, Δf_L is equal to 0.25 Hz and ΔB is approximately 6 nT. This means that for a sample with a maximum length of 5 cm an inhomogeneity of 0.12 μT/m already leads to a significant decay of signal due to the inhomogeneity.

The effects discussed above are due to the inhomogeneity of the measurement field itself and do not depend on the sample. Therefore it is called *external inhomogeneity*. Next to this external inhomogeneity also an *internal inhomogeneity* exist for heterogeneous samples composed of materials with different magnetic susceptibilities for the external field. The

magnetic field in a fluid confined in a porous system will be different from the field in the matrix of the porous system. This will induce internal gradients that can vary strongly over the sample and will depend on the geometry of the porous system. The molecular motion in those susceptibility-induced gradients can cause a random variation of the Larmor frequency of a given nucleus which is very difficult to quantify.

The total inhomogeneity within a heterogeneous sample is thus the result of the external inhomogeneity (a property of the applied magnetic field itself), superimposed with randomly varying gradients due to susceptibility differences within the sample leading to an internal inhomogeneity. Those two inhomogeneity effects will result in a faster overall decay of the transverse magnetization due to more rapid loss of coherence than would be expected from consideration of the usual spin-spin interactions alone.

2.4 The free induction decay (FID) signal and spin echo

The decay of the transverse magnetization after the spins are brought out of the equilibrium state is called *free induction decay* (FID). This signal will not only depend on the transverse relaxation, but also on the field inhomogeneity within the sample. In section 3.4.1.3 it is described how the effect of the external inhomogeneity can be minimized experimentally. Even in a perfectly homogeneous field, the internal gradients can be large due to the susceptibility differences. However, as will be shown in section 3.2, the magnitude of the internal gradients will depend on the strength of the external field. This means that for very low and homogeneous fields both the external and internal inhomogeneity will be low and the free induction signal will mainly decay due to the transverse relaxation process. By analyzing the FID envelope, the transverse relaxation time can thus be obtained when the NMR experiment is performed in a low and homogeneous field.

In standard NMR experiments, the fields that are used are several orders of magnitude larger than the Earth's magnetic field. The homogeneity of those fields is limited. Furthermore, when susceptibility differences are present, the internal gradients will be large due to the dependence on the field strength as explained in section 3.2. The FID in high fields will therefore decay very rapidly because the decay due to the inhomogeneity will be orders of magnitude larger than the decay due to the transverse relaxation. Therefore, it will be practically impossible to derive the transversal relaxation time form the FID envelope.

However, since the decay due to the inhomogeneity of the field is reversible (unlike the decay caused by relaxation), using appropriate pulse sequences can leave relaxation as the only source of the overall signal decay. After a time τ after the initial $\pi/2$ pulse (which brings the magnetization out of equilibrium by flipping it over 90°), a π pulse is brought into the system which flips the magnetization vector over 180°. This π pulses will reverse the dephasing effect

of the inhomogeneity so that after a time 2τ after the π pulse, the dephasing will be zero and the magnetization will grow to a maximum. This phenomenon is called *spin echo*. Because at the same time the magnetization will decay due to relaxation which is a process not influenced by the π pulse, the maximum of the echo will be a factor $e^{\frac{-2\tau}{T_2}}$ smaller than the maximum of the free precession signal (just after the $\pi/2$ pulse). When such a π pulse is repeated after a time τ after the echo maximum and when this is done repeatedly, as suggested by Carr and Purcell [1954], an echo sequence is induced and the maximum of all echoes will describe the relaxation decay. In such a Carr-Purcell echo train all the pulses which follow the initial $\pi/2$ pulse must satisfy the condition $\gamma B_1 \tau_p = \pi$ where τ_p is the duration of the pulse. In a Carr-Purcell-Meiboom-Gill (CPMG) sequence the π pulses are shifted in phase by 90° with respect to the phase of the $\pi/2$ pulse preventing that an incomplete satisfaction of this condition (due to the imperfection of the π pulse which is not always exactly 180°) will be accumulated (Meiboom and Gill [1958]).

Chapter 3

Earth's field NMR

3.1 The Earth's magnetic field

In this work the Earth's magnetic field is used as measuring field during the NMR experiment. The Earth's magnetic field is approximately a magnetic dipole B_0, with one pole near the geographic north pole and the other near the geographic south pole. The direction of the dipole is inclined by approximately 11.3° from the planet's axis of rotation and varies slowly with time. The origin of the field is explained by the self-sustaining dynamo theory where circulating molten metal in the inner core of the Earth is creating a magnetic field (Jackson [2000]). The Earth's magnetic field is not constant but changes slowly with time and space (see below).

Compared to the fields that can be attained with superconducting magnets used in standard NMR applications, the Earth's magnetic field is very weak: it varies from about 25 μT at the Equator to 75 μT at the poles (see figure 3.1). In Europe and North America the inclination angle of the geomagnetic field lines is about 60° to the (horizontal) surface (see figure 3.2). In the measurement laboratory at the University of Bremen the field strength is about 48 μT corresponding to a Larmor frequency for protons of about 2050 Hz and the natural inclination of the Earth's magnetic field in Bremen is about about 68.5°. Inside the laboratory this value might be different due to disturbances by ferromagnetic materials.

The Earth's magnetic field is not constant: currents in the ionosphere and disturbances from Earth's interior produce slow daily variations in the field with amplitudes of some 25 nT, corresponding to Lamor frequency variations of a few mHz. Superimposed on these variations are further oscillations with periods of a few seconds and amplitudes of about 1 nT. The diurnal variation of incoming solar radiation leading to lower magnetic flux density during the day time are the main source of temporal variations of the geomagnetic field (Berckhemer [2005]).

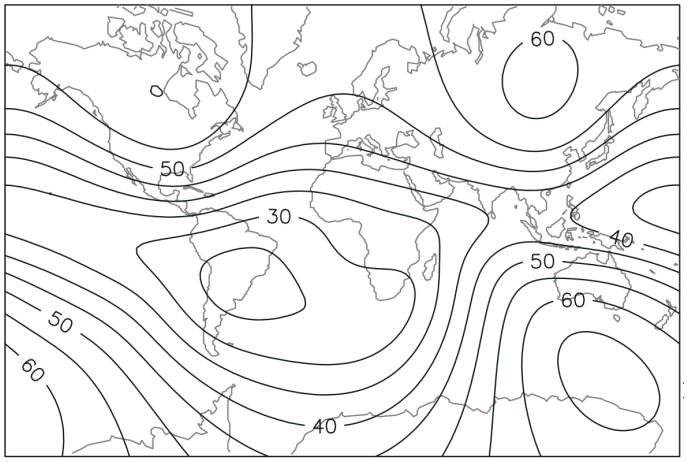

Figure 3.1: Intensity of the Earth's magnetic field in μT in the year 2000 (from: U.S. Geological Survey - National Geomagnetism Program, `http://geomag.usgs.gov/`, Oct. 2006)

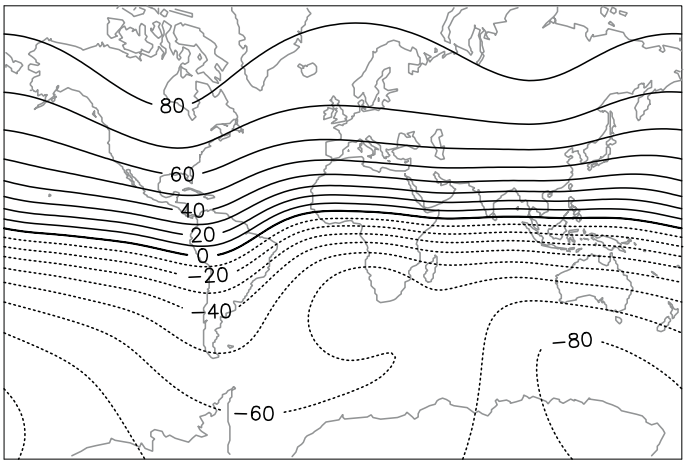

Figure 3.2: Inclination of the Earth's magnetic field in degrees in the year 2000 (from: U.S. Geological Survey - National Geomagnetism Program, `http://geomag.usgs.gov/`, Oct. 2006)

Those variations can be clearly detected in figure 3.3 where the temporal variability of the Larmor frequency in Bremen (measured with the Earth's field NMR measuring device) is compared with the continuously recorded data from the Geomagnetic Observatory Wingst (Edinburgh INTERMAGNET Geomagnetic Information Node, `http://www.geomag.bgs.ac.uk`, Oct. 2006). The diurnal variations in the measured Larmor frequency are about 2 Hz, corresponding with variations of about 0.3 μT. The variations of the magnetic field in the nT range, corresponding to changes in the Larmor frequency of a few mHz, are too small to be detected with the EFNMR device. The absolute difference of about 50 Hz between both locations is due to the fact that at the Geomagnetic Observatory Wingst, the magnetic field strength is measured without any anthropogenic disturbances. In the laboratory in Bremen, the magnetic field will be disturbed leading to a different Larmor frequency. The strong effect of the

local inhomogeneities on the Larmor frequency's magnitude is also illustrated by the fact that in another room of the same laboratory building, the Larmor frequency was about 1830 Hz (Goedecke [1993]).

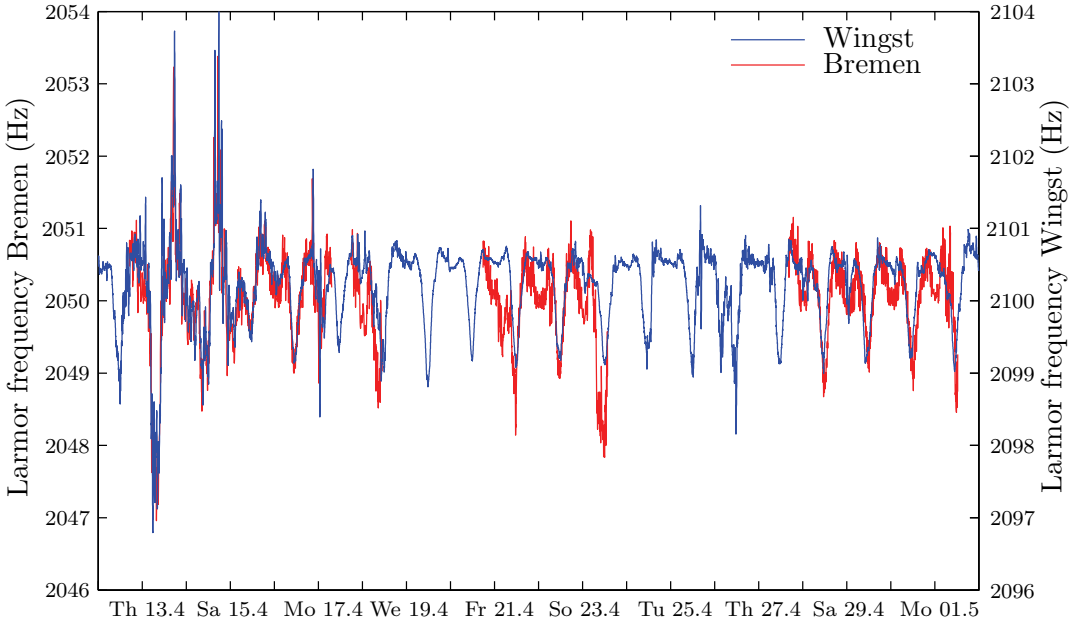

Figure 3.3: Variation of the Larmor frequency with time in the period from 13.04.2006 to 01.05.2006 in the laboratory in Bremen and the Geomagnetic Observatory in Wingst (Edinburgh INTERMAGNET Geomagnetic Information Node, `http://www.geomag.bgs.ac.uk`, Oct. 2006)

Next to the natural variations also some anthropogenic factors have influence on the temporal variations of the geomagnetic field. The main sources are probably the magnetic fields from rails and overhead electric power lines of tram and railway line (in a distance of respectively 600 m and 300 m from the laboratory) and the fields from the 50 Hz electric power supply in the laboratory and in the laboratory building. To minimize those disturbing influences, the measuring coil is built as a first order gradiometer and is surrounded by an aluminum shielding box (see section 3.4.1.1).

The Earth's magnetic field also varies in space as the global variation in figure 3.1 and 3.2 shows. The global inhomogeneity is superimposed by strong deviations of the magnetic flux density caused by a variety of susceptibilities of the materials in the bedrock. However, the gradient of the field caused by those natural sources is much smaller than the gradient due to anthropogenic factors. Ferromagnetic materials (usually iron and nickel) in and around the laboratory (reinforced concrete in the construction material, radiators and furniture in the

laboratory, etc.) will lead to strong inhomogeneities.

3.2 Earth's field NMR

Despite its advantages (see below), low field NMR and in particularly Earth's field NMR (EFNMR) is still an exotic branch in the broad pallet of NMR applications. In the past, only a few groups dealt with Earth's field NMR. Besides some smaller groups (e.g. Florokowski et al. [1969]; Powles and Cutler [1957]; Favre et al. [1990]), the most active group in this field was the group of Bene that built several Earth's field NMR devices from the late 50's until the early 80's (e.g. Rocard [1957]; Bene [1980]). Two groups still active in Earth's field NMR are the group around Callaghan (Callaghan and Le Gros [1982], Callaghan et al. [1997], Callaghan et al. [1999]), who developed the commercially available Earth's field NMR device Terranova and the group around Stepisnik (Stepisnik et al. [1994], Stepisnik [2006], Mohoric et al. [1999]), who were the first to use Earth's field NMR as an imaging tool (Planinsic et al. [1994]).

Recently there has been an increased interest in ultra low field NMR (e.g. Stepisnik [2006]), mainly due to new polarization methods such as optical pumping for ^{129}Xe (Appelt et al. [2005]) and cross-polarization of nuclei with hyperpolarized gases (e.g. ^{1}H cross-polarized with ^{129}Xe, Heckman et al. [2003]).

A short overview of the advantages and disadvantaged of EFNMR is given below:

External field homogeneity
Probably the main advantage of Earth's field NMR is the superb Earth's field homogeneity. The first NMR experiments in the Earth's magnetic field were performed at locations with minimum spatial and temporal variations of the field. Rocard [1957] describes a well chosen location in a wooden cabin in the middle of a forest far away from any urban disturbances. More recently, Callaghan et al. [1998] performed Earth's field NMR experiments in the Antarctic, where the NMR electronics were placed 10 meters away from the probe head. In such extreme locations homogeneities of $\Delta B/B_0 \approx 2.4 \cdot 10^{-9}$ m^{-1} could be obtained. This is much higher than the homogeneities reached by typical super conducting magnets for spectroscopy applications ($\Delta B/B_0 > 10^{-6}$ m^{-1}) or NMR imaging applications ($\Delta B/B_0 > 10^{-5}$ m^{-1}).

To make use of the large homogeneity of the Earth's magnetic field but to avoid such severe limitations, the device used in this work is equipped with some unique features such as an aluminum shielding box, first order gradiometer coil and shimming coils (see section 3.4.1), making Earth's field NMR possible in a normal laboratory environment.

In the laboratory building, the Earth's magnetic field is not as homogeneous as outside far away from any urban disturbances. The inhomogeneity in the laboratory is displayed in

figure 3.4 and ranges from about 0.3 to 1.4 μT/m. The inhomogeneity was measured by determining the Larmor frequency of 25 ml water with the EFNM device (see section 3.4.4) for 100 linearly spread points in a 1 m by 1 m grid in the laboratory. From the spatial variation of the Larmor frequency, the inhomogeneity of the field was derived using Eq. 2.5. In section 2.3 it has already been demonstrated that a gradient of 0.12 μT/m leads to a significant signal decay due to the inhomogeneity for samples with relatively long time constants. At the location with the lowest inhomogeneity (the blue zone in figure 3.4), the inhomogeneity is about 0.3 μT/m. For a sample with a maximum length of 5 cm, this corresponds to a value of ΔB of 0.015 μT. In such a field, complete dephasing is reached after already 0.8 s. This means that for samples with long relaxation times ($T_2 > 0.8$ s), the complete signal has decayed within a period of one time constant. Without this inhomogeneity, 37 % ($1/e$) of the initial signal amplitude would remain after this time. The inhomogeneity plays thus a major

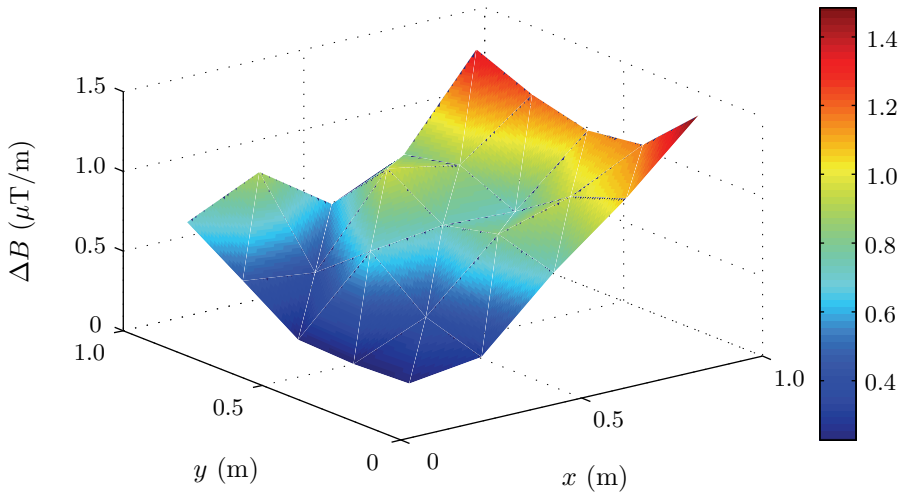

Figure 3.4: Inhomogeneity of the Earth's magnetic field in the laboratory

role in the decay of the FID envelope for substances with long relaxation times. In section 3.4.1.3 it will be shown that the homogeneity of the field can be improved by the process of *shimming*.

Costs

Additional to the good homogeneity, other advantages of using the Earth's magnetic field for NMR applications are the low production and working costs because there is no need for large and expensive superconducting magnets to induce the magnetic field as in conventional NMR techniques.

Internal inhomogeneity

Besides the better homogeneity and the lower costs, low field NMR can have other advantages. Low field NMR has been found to be more accurate than high-field NMR in measuring

water and oil volumes in media that possess large internal magnetic gradients (Manalo et al. [2003]). For fluids in porous media, a higher field improves the signal amplitude but also causes higher internal gradients that degrade the measurements through the susceptibility effect (Brown and Fantazzini [1993]). This effect is proportional to the external magnetic field strength (Doskocilova et al. [1975]). When a fluid confined in a porous medium is in an applied magnetic field, gradients arise from the field inhomogeneity ΔH, caused by the susceptibility contrast between the porous media and the pore fluid,

$$\Delta H \propto \Delta \chi H \tag{3.1}$$

where $\Delta\chi$ is the difference in susceptibilities, and H is the external static magnetic field. These susceptibility-induced gradients are called *internal gradients*. The molecular motion in those gradients causes a random variation of the Larmor frequency of a given nucleus, resulting in a more rapid loss of coherence than would be expected from consideration of the usual spin-spin interactions alone. Although the resulting echo attenuation can be reduced by employing the multiple pulse CPMG technique (see section 2.3), the high internal gradients present in heterogeneous systems can make it difficult to eliminate the attenuation effectively (Kleinberg and Horsfield [1990]).

Hurlimann [1998] analyzed the influence of internal gradients with the concept of *effective gradients*. Effective gradients are related to the field inhomogeneities over the dephasing length, the typical length over which the spins diffuse before they dephase. All the gradients in the pore space scale with $\Delta\chi H$, but the largest possible effective gradients scale with the 3/2 power of $\Delta\chi H$:

$$\sqrt{\frac{\gamma}{D_0}} \cdot (\Delta \chi B_0)^{3/2} \tag{3.2}$$

with D_0 the molecular self-diffusion coefficient of the pore fluid. $\Delta\chi$ was determined for several kinds of sand stones and varied from $1.22 \cdot 10^{-6}$ till $278 \cdot 10^{-6}$, corresponding to effective gradients of 50 μT/cm till 0.18 T/cm in a field of 2 MHz. In the Earth's magnetic field, the values of those effective gradients are more than 3000 times smaller.

Chen et al. [2005] expressed the effective spin-spin relaxation time characterizing the FID explicitly as the sum of contributions due to the spin-spin relaxation rate ($1/T_2$), the underlying external inhomogeneity of B_0 ($1/T_{2m}$), and to an internal field (B_i) induced by the susceptibility difference ($\Delta\chi$) between the pore fluid and solid matrix ($1/T_{2i}$). The $1/T_{2m}$ term is usually insignificant for samples with large susceptibility differences.

$$1/T_2^* = 1/T_2 + 1/T_{2m} + 1/T_{2i} \tag{3.3}$$

In most rocks or soils, there is a large susceptibility difference between the pore-filling fluid and the solid matrix due to the paramagnetic impurities in the solid matrix. At high magnetic fields the overall decay rate of the FID is dominated by the $1/T_{2i}$ term and the other decay

terms ($1/T_2$ and $1/T_{2m}$) can be neglected (Chen et al. [2003]). Due to the excellent external field homogeneity, the term $1/T_{2m}$ in Eq. 3.3 will be always negligible in the Earth's magnetic field. Since the largest possible effective internal magnetic field gradients, caused by the different susceptibility values of the solid grains and the pore fluid, scales with the 3/2 power of the applied magnetic field strength, also the effect of the internal inhomogeneity can be minimized by a reduction of the applied magnetic field.

Kleinberg and Horsfield [1990] demonstrated that the transversal relaxation rate changes roughly with the square of the product of Larmor frequency and echo spacing for sandstone and limestone samples. According to this theory, reducing the field (e.g. from 2 MHz to 2 kHz, i.e. performing the measurements in the Earth's magnetic field) will decrease the overall relaxation rate ($1/T_2^*$ in Eq. 3.3) due to the decrease of $1/T_{2i}$. At low fields, the free induction decay of the magnetization is therefore expected to be dominated by contact between the relaxing spins and the surface of the matrix of porous system, i.e. $1/T_2$ dominates the overall relaxation (see Eq. 3.3). As will be shown in chapter 5, this is only true for samples with moderate susceptibility differences between the pore fluid and the surface of the matrix. When those susceptibility differences are increasing, the effect of the internal inhomogeneity can not be neglected anymore.

Increased relaxation

The relaxation times will depend in a small or large extent on the Larmor frequency (see Eqn. 2.29 and 2.30). While the frequency dependence for bulk water is usually small, it can increase dramatically for water confined in porous media or gelous systems (see section 2.2). At low fields this property can be advantageous when analyzing changes in the environment of the protons that have an effect on the relaxation time. At low fields, those changes will have a much larger effect on relaxation than in higher fields.

Low signal to noise ratio

The reason for the relatively limited research on low field NMR is probably due to the fact that since the first description of the NMR phenomenon by Bloch et al. [1946] and Purcell et al. [1946], there was a continuous trend to higher magnetic fields because the signal to noise ratio is proportional to the field strength. The lack of sensitivity is therefore one of the main drawbacks of NMR at low magnetic fields.

The S/N ratio can be expressed as (Abragam [1973]):

$$\frac{S}{N} \propto \chi B_0 \sqrt{\frac{\eta f_L Q V_S}{\Delta f k T}} \tag{3.4}$$

with χ the nuclear magnetic susceptibility, f_L the Larmor frequency, Q the quality factor of the coil, V_S the sample volume and Δf the band width of the system. From this formula it can be seen that the S/N ratio is proportional to $B_0^{3/2}$. Due to the small field strength, the signal to noise ratio will be also very small in the Earth's magnetic field. To improve

sensitivity, there are two processes that can be adjusted: the polarization and the detection.

Because the measurement field and the polarization field do not necessarily have to be of the same strength, the Earth's magnetic field is usually only used as the measurement field and the protons in the sample are polarized by a field that can be more than 1000 times stronger. This method, increasing the S/N ratio by this factor, was already reported in 1954 (Packard and Varian [1954]) and is also used in this work. In this method the pre-polarization of the sample and the detection of the signal is done with the same coil. Appelt et al. [2006] showed that it is also possible to pre-polarize the sample in a Halbach magnet, then transfer the sample mechanically into the probe head and detect signals with S/N ratios of 3 to 100 for a single acquisition on 2 cm^3 samples.

Additional to improvements in the polarization, the sensitivity can also be increased by adjustments at the detection level. The lower sensitivity at the detection level is usually compensated by large sample volumes that can be used because of the high external field homogeneity. In this work, sample volumes of 25 ml are used, a volume which is comparable with commercially available NMR relaxometers having field strengths of a few MHz, but considerably smaller than in other low-field instruments that are using sample volumes up to 0.5 l (e.g. Callaghan et al. [1998]). Furthermore, because of the low Larmor frequency, the band width of the system can be reduced in comparison with high field applications.

Due to the pre-polarization, the relatively large sample volume and the well chosen design of the probe head and the electronics, a S/N ratio of about 100:1 for 25 ml of water can be achieved with a single scan. This is, unlike one would expect from Eq. 3.4, comparable to high-field applications and compensates the main drawbacks of low-field NMR.

3.3 Measurement principle applied in this work

A graphical representation of the measurement principles is displayed in figure 3.5. A coil is placed with its axis (x-axis in an imaginary Cartesian coordinate system) orthogonal to the direction of the Earth's magnetic field (z-axis). The excitation of the protons within the sample is performed by directing a current I_p through the coil for a time t_p (switch at position 1 in figure 3.5). This current will induce a magnetic induction B_p in the axial direction of the coil. Due to this induction, the macroscopic magnetic moment M_p from the ensemble of protons will be aligned in the direction of B_p (see Eq. 2.16). Since in this situation the components of M orthogonal to the direction of B_p (x-direction) are not of importance anymore ($B_p >> B_0$), the Bloch equations can be simplified to

$$\frac{\mathrm{d}M_p}{\mathrm{d}t} = -\frac{1}{T_1} \cdot (M_p - M_{pe}) \tag{3.5}$$

with solution

$$M_p = M_{pe} + (M_{pp} - M_{pe}) \cdot \exp(-\frac{t_p}{T_1}) \tag{3.6}$$

M_{pp} represents the magnetization before the polarization and M_{pe} the magnitization at equilibrium, i.e. for $t_p \to \infty$ or $t_p >> T_1$.

In the second step the polarizing field B_p is rapidly switched off non-adiabatically. Non-adiabatically means $\mathrm{d}B_p/\mathrm{d}t \geq \gamma B_0^2$, i.e. the magnetization remains aligned along B_p. Because B_0 is orthogonal to B_p, the precession of the bulk magnetization is then directly observable (Abragam [1973]). In contrast, some EFNMR devices (e.g. Callaghan et al. [1997]) are switching off the polarizing field adiabatically ($\mathrm{d}B_p/\mathrm{d}t << \gamma B_0^2$). In this case the bulk magnetization becomes aligned along the measurement field B_0 and it is then necessary to apply a $\pi/2$ pulse to observe the precession of the magnetization.

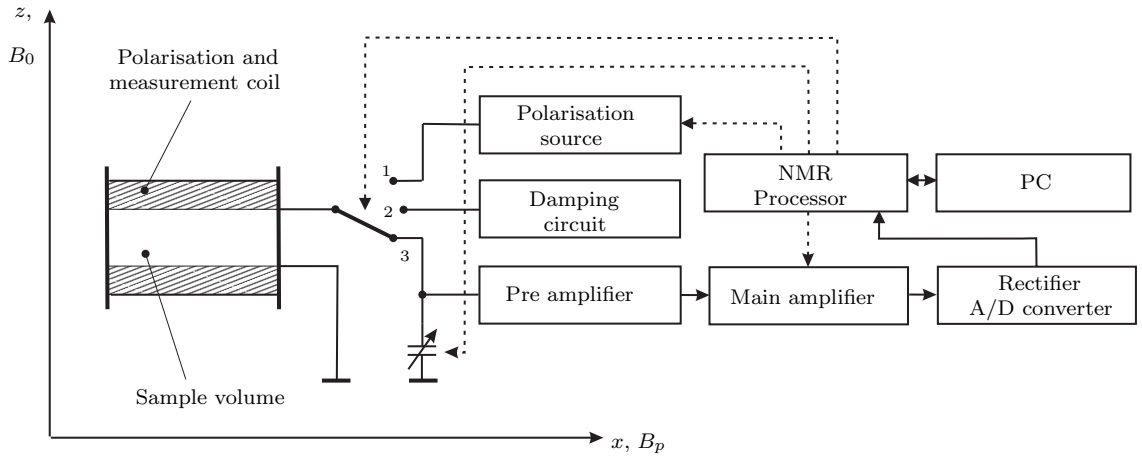

Figure 3.5: Schematic overview of the measuring principle

Rapidly switching off B_p inevitably results in a transient field which arises from the currents proportional to $\mathrm{d}B/\mathrm{d}t$ induced in any conductive materials (e.g. components of the experimental apparatus). The energy related with those transients must be withdrawn and dispersed rapidly (switch at position 2 in figure 3.5) to be able to detect the FID signal within a few milliseconds after switching off the polarizing field.

At this stage M_p will only be influenced by B_0 and the Bloch equations can be reduced to

$$\frac{\mathrm{d}M_x}{\mathrm{d}t} = \gamma \cdot (M_y B_z) - \frac{1}{T_2} \cdot M_x \tag{3.7}$$

$$\frac{\mathrm{d}M_y}{\mathrm{d}t} = -\gamma \cdot (M_x B_z) - \frac{1}{T_2} \cdot M_y \tag{3.8}$$

If the initial condition is $M_{x,0} = M_p$, the x-component of the solution for (3.7) and (3.8) can be written as

$$M_x = M_p \cdot \exp(-\frac{t}{T_2}) \cdot \cos(\omega_L t) \tag{3.9}$$

Substituting (3.6) in (3.9) gives

$$M_x = \left[M_{pe} + (M_{pp} - M_{pe}) \cdot \exp(-\frac{t_p}{T_1}) \right] \cdot \exp(-\frac{t}{T_2}) \cdot \cos(\omega_L t) \tag{3.10}$$

This equation describes the precessing magnetic moment of the nuclei around the direction of the Earth's magnetic induction $\vec{B}_0$ after switching off $\vec{B}_p$. A qualitative representation of the overall magnetization vector precessing in the xy-plane is displayed in figure 3.6. The precessing magnetic moment will induce an alternating current in the coil with frequency $f_L = \omega_L/2\pi$ which can be amplified and analysed (switch in position 3 in figure 3.5). The initial amplitude of the alternating current depends on the amount of nuclei in the sample, on the magnitude of the magnetic induction B_p and on the ratio t_p/T_1. This free induction decay (FID) signal will decay with a time constant T_2 when B_0 is perfectly homogeneous within the sample. From the envelope of this decay the transversal relaxation time can be derived directly.

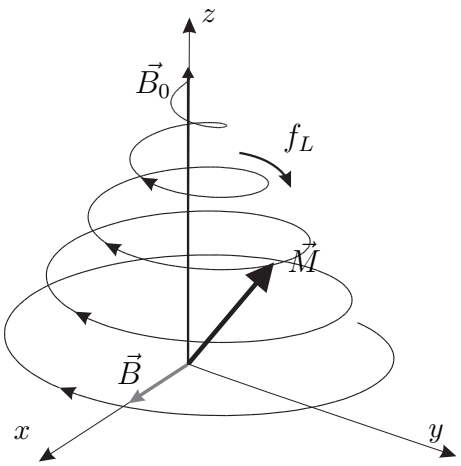

Figure 3.6: Evolution of the overall magnetization in the sample around $\vec{B}_0$ after switching off the polarizing field $\vec{B}_p$

Since the longitudinal variation of the magnetization M_p described by the longitudinal time constant T_1 does not induce a signal in the coil, T_1 cannot be measured directly. But by varying t_p, the amplitudes of the induced FIDs can be described by Eq. 3.6 from which T_1 can be derived (see Fig. 3.7). By varying B_p, T_1 can be measured at different field strengths or different Larmor frequencies. This method of measuring T_1 is usually called *electronic Field-Cycling-Technique* and was first described by Bloom and Mansir [1954].

The different stages of T_2 and T_1 measurements are explained below (figure 3.7).

1. One can distinguish between two different cases:

   - figure 3.7 *bottom*: For measurements at low magnetic induction ($B_p \leq 1/2 \cdot B_{p,max}$),

the magnetization of the nuclei is enlarged by a pre-polarisation pulse with a maximum magnetic induction $B_{p,max}$ (see Eq. 2.16). Since T_2 is measured in the Earth's magnetic field it does not depend on the magnitude of B_p. But because the signal to noise ratio increases with increasing B_p, the transversal relaxation time will always be measured using the maximum polarizing induction.

- figure 3.7 *top*: For measurements at high magnetic induction ($B_p > 1/2 \cdot B_{p,max}$), no pre-polarisation is necessary so that $t_{pp} = M_{pp} = 0$.

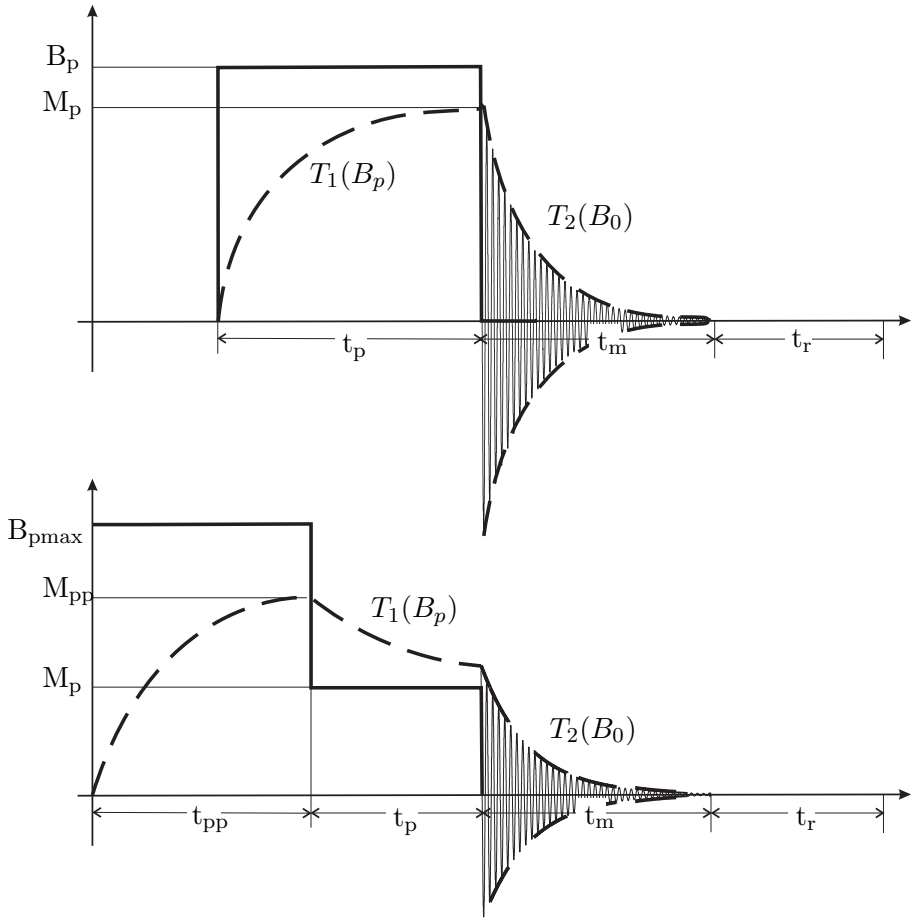

Figure 3.7: Magnetic induction (B_p) and x-component of the macroscopic nuclear magnetic moment (M_p) during a Field-Cycling-experiment in the magnetic induction of the Earth (B_0) with pre-polarisation by the method of Packard and Varian [1954] with t_{pp}: pre-polarisation time, t_p: polarisation time, t_m: measurement time, t_r: repetition time. Top: $B_p \geq \frac{1}{2}B_{p,max}$, bottom:$B_p < B_{p,max}$.

2. During the polarisation time t_p the magnetic induction B_p is generated and the magnetic moment M_p will be described by Eq. 3.6.

3. After switching off B_p rapidly and non-adiabatically (see above), the x-component of M_p starts to precess around B_0 and induces an alternating current in the coil. The amplitude of the FID decreases exponentially as described by Eq. 3.10 and is measured during t_m.

4. After the waiting time t_r the magnetization has reached the equilibrium state and the coil has cooled down preventing thermal overload.

5. When stage 1 till 4 are repeated, the signal to noise ratio of the FID can be improved by signal accumulation.

6. When stage 5 is done for different values of t_p, T_1 can be derived from the variation of the starting amplitudes of the respective FIDs (see Eq. 3.6 or 3.10).

7. By repeating all steps at different values for B_p, a so called relaxation dispersion curve can be derived by measuring T_1 at different field strengths.

In the derivation of Eqs. 3.6 and 3.10 it was assumed that the exponential decay of the magnetization could be described by only one time constant. In real samples however, especially in porous systems, the decay is often multi-exponential (see chapter 2.2). In those cases the exponential terms in Eq. 3.10 have to be replaced by weighted sums of exponentials. This does not change anything about the measuring method but will lead to higher demands in setting the measurement variables because the different relaxation times have to be measured in the same measurement.

3.4 The Earth's field NMR device

The Earth's field NMR device is based on the work of Goedecke [1993]. This author also carried out some improvements on the electronics of the device in this work. Additional to the replacements of some small electronic components, the shortening of the dead time from about 28 ms to 8 ms (see section 3.4.3.1) and the development of the serial port communication were the main improvements done by the author of the original work.

Additional to those improvements, some hardware components were replaced completely in the framework of this work. The probe head (see section 3.4.1.1) together with the coil (see section 3.4.1.4) and sample temperating (see section 3.4.1.5) were newly designed and rebuilt to better fulfill the needs encountered in this work. Some other components such as the shimming coils (see section 3.4.1.3) were slightly modified. Additional to the improvements in the hardware and electronic components, the data acquisition and analysis was completely modified and is now performed by a self-written software running on a standard PC.

In the following sections the main characteristics of the particular components of the device will be described. The EFNMR device can be equipped with two different probe heads: an *in-vitro* and an *in-situ* probe head. When using the in-vitro probe head, the sample must fit within the cylindrical sample space of about 25 ml (see section 3.4.1). Since the sensitive volume of the in-situ probe head is situated outside the coil, the geometry of samples measured by this probe head is less restricted (see section 3.4.2). The in-situ probe head was originally built for in-vivo applications (Goedecke [1993] and Goedecke and von Boetticher [1999]).

3.4.1 In-vitro measurements

3.4.1.1 Probe head

As explained in section 3.3 the measurement principle used in this work uses the same coil to polarize the sample (in order to bring the magnetization vector out of equilibrium and increase the magnetization) and to detect the signal after this polarization. Although other NMR devices operating in the Earth's magnetic field are usually using separate coils to polarize and to detect (e.g. Callaghan et al. [1997]), this setup is chosen because the distance between the sample and the coil is optimal (minimal) for polarization as well as detection which will lead to a higher sensitivity. The disadvantage of using only one coil is the fact that in order to optimize the dimensions of the coil, different requirements that are often conflicting with each other have to be fulfilled. The most important requirements are listed below:

1. The probe head must be dimensioned for realistic probe volumes. Since the first experiments will make use of commercially available well defined artificial systems with volumes of a few cubic centimeters, the probe head should have sample dimensions in this order of magnitude. Larger dimensions would lead to a large need of sometimes very expensive sample material, too small dimensions will lead to border effects, unrepresentative samples and a lower sensitivity.

2. The NMR device must be able to measure relaxation times in the order of magnitude as they occur in porous systems (from a few milliseconds up to few seconds). Measuring relaxation times of a few milliseconds is only possible with measurement systems having even shorter time constants. Very large coils do not bring any advantage since the potential high quality factor Q has to be artificially decreased in order to realize a short time constant ($\tau = Q/\omega_L$) of the input circuit. A low quality factor is also desirable to decrease the effect of radiation damping (see Goedecke [1993]).

3. Measurements must be possible in inhomogeneous magnetic fields such as a normal laboratory environment (see figure 3.4). This requirement favors smaller sample volumes

since the absolute deviations of the mean magnetic induction will be smaller for smaller samples for the same external inhomogeneity.

4. Since the amplitude of the FID signal depends on the strength of the pre-polarizing field B_p, it is desirable to be able to induce maximal field strengths. The magnetic induction in the middle of a coil is proportional to the square root of the applied electrical power and inversely proportional to the coil dimensions. This also favors smaller sample volumes.

5. In order to handle the necessary voltages with power semiconductors, the high magnetic induction should be induced with moderate voltages (a few hundred volts), requesting a coil with a low resistance.

6. The sample must be large enough to ensure a large signal to noise ratio. The signal to noise ratio is proportional with the square of the coil inner radius. This requirement limits the minimization of the sample volume.

7. To minimize the induction by external disturbing alternating fields, the winding surface of the coil should be minimal, favoring small coil dimensions.

8. A commercially available standard sample holder should be used.

An optimization of the coil dimensions is difficult due to the contradictory character of the requirements listed above. Without experimental measurements it is difficult to weight those requirements. The dimensions of the coil displayed in figure 3.8 are a result of experiments done in this work and by Goedecke [1993]. The main characteristics of the coil are given in Table 3.1.

The probe head exists of two identical coils, wound in directions opposite to each other, connected in series and placed behind each other (*first order gradiometer*). The sample is located in one of the coils, while the other half is left empty. In this way external magnetic field noise common to both coils is canceled out and the signal from the sample in one of the coils can be detected with minimal interference. To construct such a first order gradiometer, the coils were wound with the same number of turns (3000) and placed in the center of a strong alternating magnetic field. Because the coils are wound in opposite direction, the net voltage induced in the coils should be zero for perfectly symmetrical coils. In order to achieve a zero net induction, 9 windings had to be removed from the coil with the highest induction. After this removal the induction in the coils connected in series was a factor of thousand smaller than the induction in one coil half. The coil holding the sample is provided with some auxiliary equipment for sample temperating (see section 3.4.1.5) and sample fixation.

As already mentioned, the same coil is used to prepolarize the sample and to measure the FID signal. Since the measured signal amplitude is proportional to the polarization strength, the

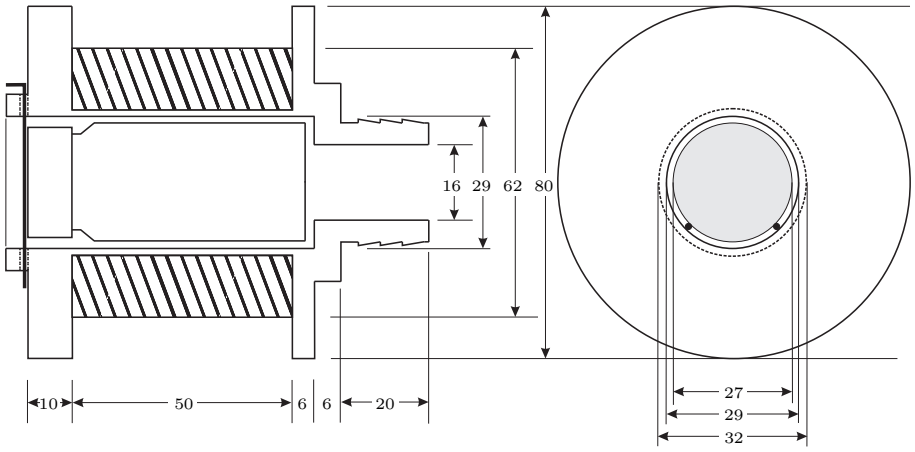

Figure 3.8: Side and front view of the in-vitro measuring coil (dimensions in mm)

Table 3.1: Some characteristics of the in-vitro coil.

Coil material:	Polycarbonate		
Winding inner radius	R_i	= 16.0 mm	
Winding outer radius	R_o	= 30.8 mm	
Length	2b	= 50 mm	
Winding radius	d	= 0.5 mm	
Winding number	n	= 3000 / 2991	per coil half
Winding cross section	F	= 743.5 mm^2	per coil half
Average winding area	A	= 178 mm^2	per coil half
Total winding area	$n \cdot A$	= 5.34 m^2	per coil half
Copper filling factor	f	= 0.79	
Copper mass	m	= 1.550 kg	
Resistance	R	= 75.6 Ω	at 20°C
Inductance	L	= 0.406 Hy	
Time constant	τ_C	= 5.4 ms	
Self capacitance	C_L	= 200 pF	
Ratio Induction/Current	B/I	= 0.057 T/A	

ratio of the magnetic induction to the input current of the coil is an important characteristic of the coil. Because the coil is dimensioned to optimize the signal amplitude and not the homogeneity within the coil, the field in the sample volume will not be constant.

In figure 3.9 the spatial variation of the ratio B/I on the coil axis is displayed. To measure this ratio an alternating field was induced by a current I through the coil and a copper loop (with the same dimensions as the sample) was inserted in the measuring coil. The voltage induced in the copper loop is equal to:

$$|U_i| = n \cdot A \cdot \omega \cdot B \tag{3.11}$$

with n the number of windings, A the average winding area and $\omega/2\pi$ the frequency of the alternating field. This induced alternating voltage was calculated back to the average magnetic field density (B) and divided by the current I through the coil.

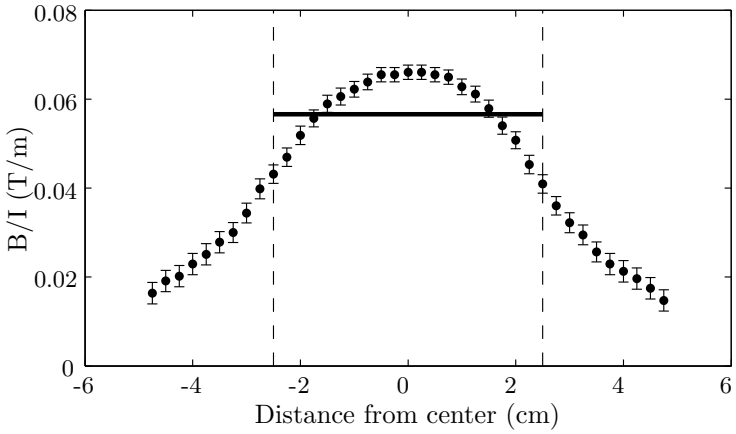

Figure 3.9: The ratio of average magnetic induction and the inducing current I in the sample volume in function of the distance from the center on the coil axis. The vertical lines represent the sample dimensions and the horizontal line represents the average value of B/I in this region.

The average value of this ratio within the sample volume is about 0.057 T/A with a maximum value of 0.066 T/A and a minimum value of 0.036 T/A. This minimum value is only valid for a small part of the sample volume as can be seen from the position of the sample in figure 3.9. For most experiments a current of 1 A is taken for the polarization, resulting in a polarization field of about 60 mT. With an electrical resistance of the coils of 75,6 Ω such a polarization strength is achieved by moderate voltages ($U_p < 120$ V). Higher currents will lead to higher polarization strengths but would also increase the power drastically ($P = R \cdot I^2$), resulting in an intense warming up of the coil.

The distance between the compensation and polarization coil is 4 cm. This means that the smallest distance between the sample and the center of the compensation coil is 6.5 cm ($5/2 + 4$). From figure 3.9 it can be seen that at this distance the magnetic induction is insignificant. The compensation coil will therefore have no significant influence on the polarization of the sample.

Due to the reciprocity theorem, the relative sensitivity of the coil for alternating magnetic fields from the copper loop inside the coil will have the same shape as the ratio B/I displayed in figure 3.9. The spatial dependence of the local contribution of the precessing protons to the detected signal can therefore be described by the product of relative sensitivity with the ratio

B/I. From figure 3.10 it can be seen that the contribution to the FID signal form protons at the border regions of the sample ($z = 2.5$ cm) is only about one third from the contribution from protons at the center of the sample.

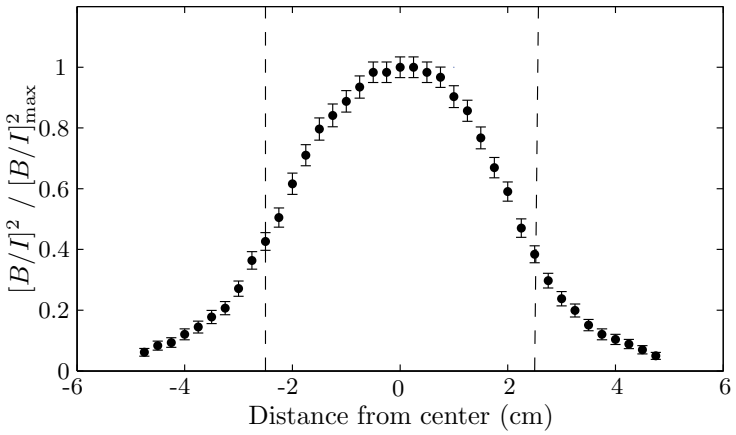

Figure 3.10: The product of relative sensitivity with the ratio of the average magnetic induction and the inducing current I in the sample volume ($[B/I]^2 \ / \ [B/I]^2_{\max}$) in function of the distance from the center on the coil axis. The vertical lines represent the sample dimensions.

It has to be repeated that the strength of the polarization has no influence on the transversal relaxation time T_2, since this time constant is always measured in the Earth's magnetic field. However, the longitudinal time constant is measured in the polarizing field and will depend on its magnitude. But in a typical longitudinal relaxation dispersion, $1/T_1$ (the transversal relaxation rate) only varies significantly when the field strength B_p is changed over several orders of magnitude, so that the variation of B/I within the sample volume is negligible.

3.4.1.2 Shielding

The coil is placed in a 4 mm thick aluminum shielding box to minimize the influences from external alternating electrical and magnetic fields (Goedecke [1993]). The construction of this shielding box is based on the work of Meyer [1984] but the dimensions were slightly reduced for transport purposes (dimensions: $0.78 \times 0.78 \times 0.81$ m). This shielding box has one open side in the direction of the coil axis for better sample handling. The magnetic shielding factor of this aluminum box is about 285 at a frequency of 2050 Hz. In figure 3.11 the measurement coil inside the shielding box is displayed.

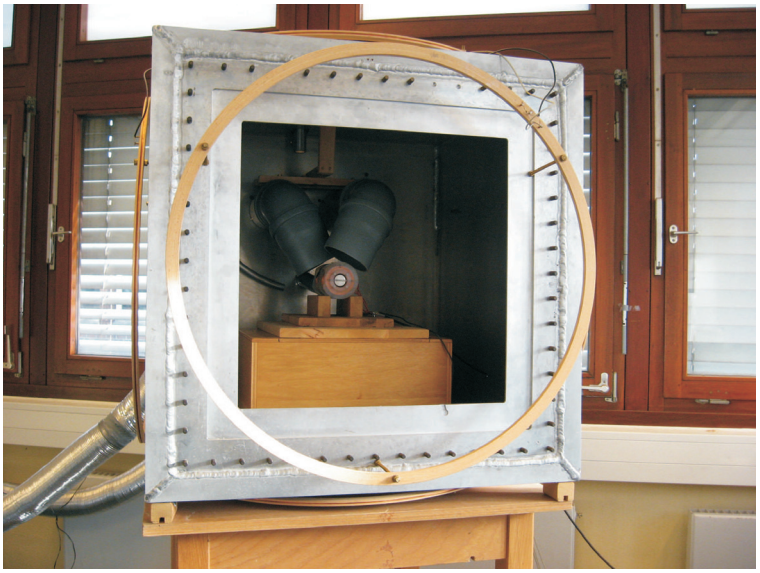

Figure 3.11: Probe head inside the aluminum shielding box

3.4.1.3 Optimizing the field homogeneity

As already mentioned in section 2.3 a very homogeneous field is needed to perform the NMR experiment in the Earth's magnetic field without pulse sequences. The Earth's magnetic field is not homogeneous in the laboratory mainly due to iron from reinforced concrete, radiators and furniture (see section 3.1). In standard NMR applications, the inhomogeneity can be canceled out by applying pulse sequences as explained in section 2.3. In this work the external homogeneity is optimized by choosing the best location in the laboratory (see figure 3.4) and by shimming using three pairs of Maxwell coils. The small remaining inhomogeneity that is then still present in the sample is modeled so that the decay due to relaxation can be derived from the digitized FID.

Choosing the optimal location

The variation of the inhomogeneity in the laboratory is displayed in figure 3.4 and ranges from about 0.3 to 1.4 μT/m. The Earth's field NMR device is placed at the location with the lowest inhomogeneity. But even at this location (the dark blue zone in figure 3.4), there is a significant decay of signal due to the inhomogeneity (see section 2.3). Therefore the inhomogeneity is further improved by shimming the field.

Shimming

Shimming is the process in which the field is adjusted in a way that the inhomogeneities in the sample are minimized. Two types of shimming can be distinguished. *Passive shimming* involves pieces of ferrous material that are placed in the neighborhood of the magnetic field in such a way that the original field is getting more homogeneous. In this work *active shimming*

is used by installing three pairs of coils exactly around the center of the measuring coil (and sample volume). The dimensions are chosen large to prevent disturbing influences from the shimming coil on the measuring coil. The coils in every pair have the same amount of windings, they are wound in opposite directions with respect to each other and connected in series. For a certain distance between the two coils (depending on the coil radius, see below), a current I flowing through the coil pair will induce a linear magnetic field gradient $\mathrm{d}H/\mathrm{d}z$ between the pairs without a nominal change of the magnetic induction in the center of the coils (see figure 3.12). Such kind of coils are then called *Maxwell coils*.

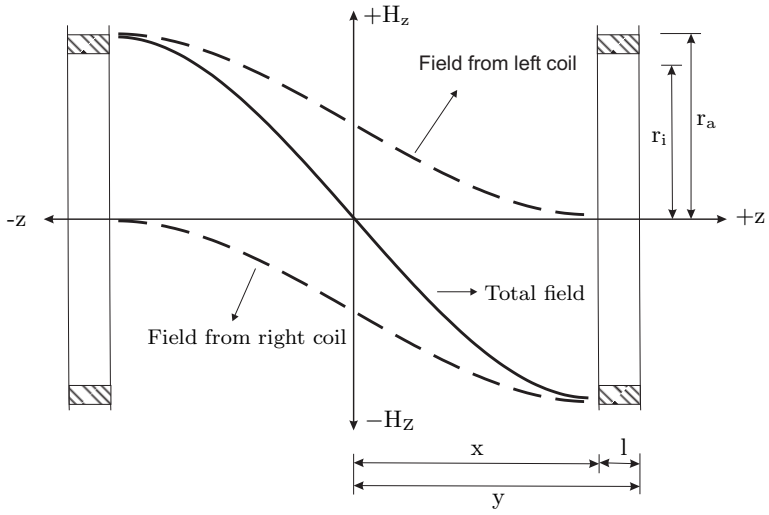

Figure 3.12: Field variation on the axis of a pair of Maxwell coils. The dimensions are given in the text.

The series expansion of the anti-symmetric function $H(z)$ describing the field variation on the coil axis is

$$H_z(z) = \frac{H_z'(0)}{1!}z + \frac{H_z'''(0)}{3!}z^3 + \frac{H_z^V(0)}{5!}z^5 + ... \tag{3.12}$$

The first term of this expression defines the constant gradient. The main deviation of this constant gradient is determined by the next term so that in order to obtain an approximately constant linear gradient the following condition must be fulfilled:

$$\mathrm{d}^3H/\mathrm{d}z^3 = 0 \tag{3.13}$$

The influence of the 5th and higher order components will be very small and can be neglected. The magnetic induction induced by a cylindrical coil on the coil axis can be calculated by applying the Biot-Savart law (Berger and Butterweck [1956]):

$$H(z) = \frac{N \cdot I}{2(r_a - r_i)}\left[y\left(Arcsin\frac{r_a}{x+l} - Arcsin\frac{r_i}{x+l}\right) - x\left(Arcsin\frac{r_a}{x} - Arcsin\frac{r_i}{x}\right)\right] \tag{3.14}$$

The physical meaning of the parameters in this equation are given in figure 3.12. Applying

condition 3.13 on Eq. 3.14 and given $r_a - r_i = 0.001$ m and $l = 0.002$ m, leads to:

$$x \approx 0.8618 \times r_i \tag{3.15}$$

For $r_i = 0.3425$ m, the distance between the two coils would be 0.59 m. Since the aluminum shielding box (see section 3.4.1.2) has a size length of about 0.8 m, choosing this value for x would mean that the shimming coils are installed within the shielding box. This would make the shielding effectless and therefore an x value of 0.43 is taken. The deviation from the linear gradient with this non optimal value for x is negligible ($\pm$ 0.1%) within the sample volume (see figure 3.13). Also the 5th and higher order components will not influence the linear gradient significantly (see Eq, 3.12).

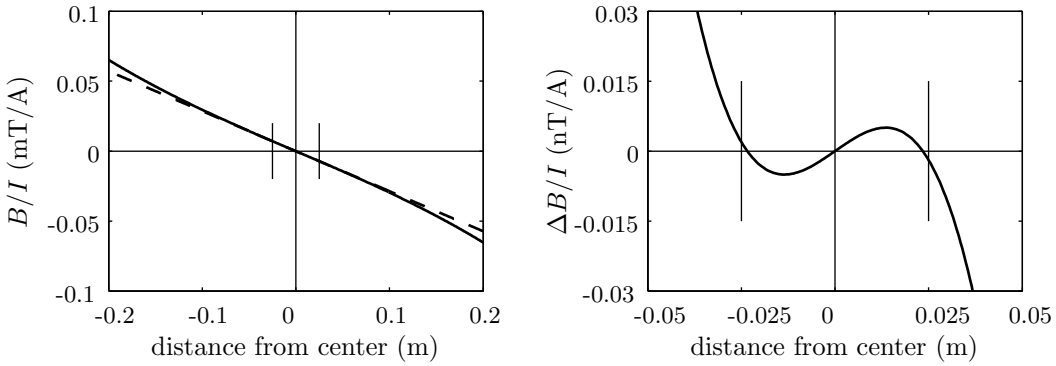

Figure 3.13: *Left*: linear gradient (**- - -**) and gradient with non optimal distance between the two Maxwell coils (——). *Right*: deviation from the linear gradient within the sample. The vertical marks represent the longest dimension of the sample volume ($\approx$ 50 mm). Mind the different units of both figures.

During the shimming process, the direct current I through every *Maxwell pair* is adjusted manually until the free precession signal of a 25 ml water sample can be fitted well with one (long) time constant corresponding to literature values ($T_2 \approx 1.8$ s). After a rough adjustment of the currents through every pair of coils independently, the shimming procedure is repeated with a fine adjustment of the currents. The whole procedure takes about 25 minutes and, when no changes occur in the location of ferromagnetic materials in the laboratory, only has to be checked about once a month. The current that has to be set to compensate the gradient along the axial direction of the sample (the largest dimension of the sample) is about 3.8 mA, leading to a gradient of about 0.33 μT/m. This value corresponds very well to the gradient values in the dark blue zone one of figure 3.4, where the measuring coil is placed (0.2 - 0.4 μT/m).

The result of the shimming procedure is displayed in figure 3.14. The difference between the FID with and without compensation is considerable and shows the importance of the shimming process. The inhomogeneity in the sample leads to dephasing of the net magnetization

because spins at different locations within the sample precess at different frequencies. When all spins are completely out of phase the signal amplitude is zero. Because the dephasing will go on, the spins can come in phase again leading to an increase of the signal amplitude and an *echoes* can be detected.

The FID recorded in an inhomogeneous field can obviously not correctly be described by an exponential decay with one or more time constants. However, the time response of FID signals shortened by artifacts during the measurement or by inhomogeneity is generally described by T_2^*, analog to the time constant T_2. Although T_2^* cannot be interpreted as a real time constant in sense of describing an exponential decay, it gives a quantitative value for the quality (homogeneity) of the measuring field. In the ideal case with zero inhomogeneity, T_2^* is equal to T_2. The FID without compensation in figure 3.14 has a T_2^* value of about 0.4 s. For the FID with shimming this value is equal to about 1.6 s and close to the theoretical T_2 of 1.8 s (black curve in the figure). Even after the shimming process, there still exists a remaining inhomogeneity that shortens the signal slightly. Deriving the real time constant T_2 from the FID measured in a slightly inhomogeneous field is done by including a non-exponential term in the FID-model.

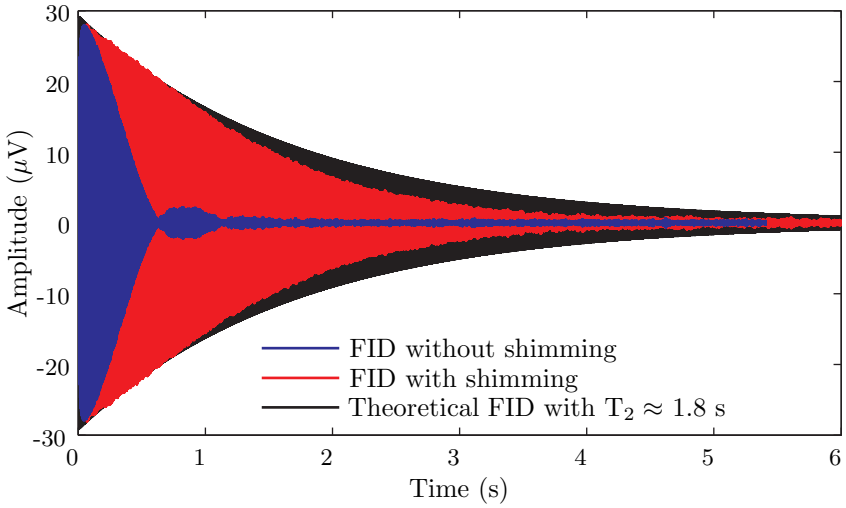

Figure 3.14: Effect of shimming on the FID signal of 25 ml H_2O at 20°C (not deoxygenated)

Modeling the remaining inhomogeneity

As can already be seen from figure 3.14 the effect of the residual inhomogeneity is rather small within the first second of the free induction decay. Therefore it can be neglected for samples with short relaxation times ($T_2 < 0.5$ s). Only for samples with longer relaxation times, the residual external inhomogeneity after shimming has to be taken into account to be able to derive the correct relaxation times. In figure 3.15 the envelopes of the FIDs of a sample with long relaxation time (water with $T_2 = 1.80$ s) and a sample with shorter relaxation time ($MnCl_2$ with $T_2 = 0.282$ s) are displayed. The effect of the inhomogeneity and hence

the effect of the compensating shimming process is larger for the water sample than for the $MnCl_2$ sample. The remaining inhomogeneity plays almost no role anymore for the $MnCl_2$ sample: the difference between T_2^* and T_2 is minimal (278 vs. 283 ms). For water however, the effect of the remaining homogeneity after shimming is clearly visible and the difference between T_2^* and T_2 is not negligible (1.60 vs 1.80 s) and therefore the corresponding FID cannot be modeled by a single exponential decay and a correct modeling of the effect of the remaining inhomogeneity is necessary.

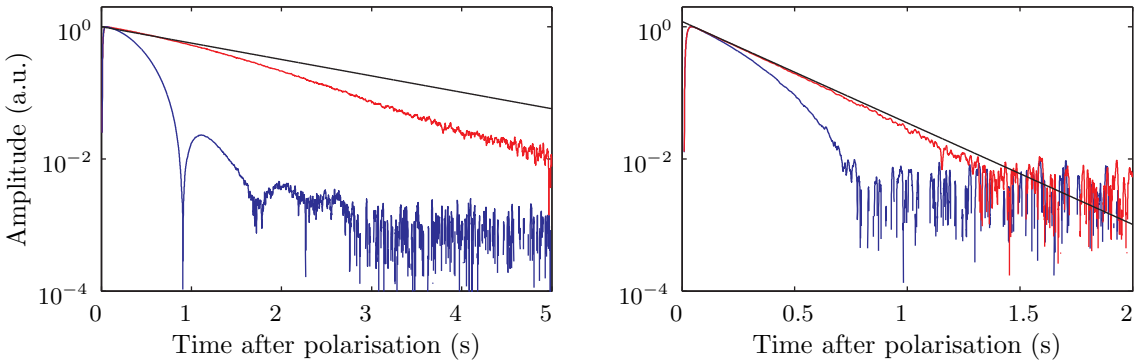

Figure 3.15: Theoretical FID envelope (black), FID envelope with shimming (red) and without shimming (blue) of 25 ml of water with $T_2 = 1.80$ s (*left*) and for 25 ml $MnCl_2$ with $T_2 = 0.28$ s (*right*) at 20°C

To take field inhomogeneity into account, we assume that the magnetic induction $\vec{B_0}$ can be written as a sum of a homogeneous term $\vec{B_E}$ coming from the very homogeneous Earth's magnetic field $\vec{H_E}$ and a term $\vec{B}(\vec{r})$ variable in space:

$$\vec{B_0} = \vec{B_E} + \vec{B}(\vec{r}). \tag{3.16}$$

$P(\vec{B})$ being the probability density distribution function of $\vec{B}(\vec{r})$, Eq. 3.9 can be written as

$$M_x(t) = M_p \cdot \exp(-\frac{t}{T_2}) \cdot \int_{-\infty}^{+\infty} P(\vec{B}) \cdot \cos\left[\gamma \cdot (B_E + B) \cdot t\right] \mathrm{d}B \tag{3.17}$$

Applying the cosine addition theorem, this expression can be simplified to

$$M_x(t) = M_p \cdot \exp(-\frac{t}{T_2}) \cdot \cos(\gamma B_E t) \cdot \int_{-\infty}^{+\infty} P(\vec{B}) \cdot \cos(\gamma B t) \, \mathrm{d}B \tag{3.18}$$

because the integral of $P(\vec{B}) \cdot \sin(\gamma B t)$ is zero when $P(\vec{B})$ is a symmetric function. Eq. 3.18 was simplified by two different approaches:

- In a first approach it is assumed that the superposed field $\vec{B}(\vec{r})$ vanishes at the origin and has a gradient G in the z-direction with an axial symmetry about the z-axis. According

to Torrey [1956], the most general field of this character can be written as:

$$\vec{B} = (\frac{1}{2}Gx, \frac{1}{2}Gy, B_0 + Gz) \tag{3.19}$$

This leads to an expression for B equal to:

$$B = \sqrt{B_x^2 + B_y^2 + B_z^2} = \sqrt{(B_0 + Gz)^2 + \frac{1}{4} \cdot G^2(x^2 + y^2)} \tag{3.20}$$

The second term under the square root will be orders of magnitude smaller than the first one, so that the gradient in the x- and y-direction will be negligible and $B = B_0 + Gz$. The integral (I) in Eq. 3.18 can then be transferred into an integral over z because due to the cylindrical symmetry of the sample volume, all volume elements parallel with the coil axis ($z = 0$) are giving a constant contribution:

$$I = C \cdot \int_{-R}^{+R} G(z) \cdot \cos(\tau \cdot z) \cdot \mathrm{d}z \tag{3.21}$$

with $\mathrm{d}B_i/\mathrm{d}z = G$, $\tau = \gamma G t$ and C a constant. R is the inner sample radius. $G(z)$ is now the relative amount of volume elements at a distance z from the coil axis and can be expressed by:

$$G(z) = \sqrt{R^2 - z^2} = R\sqrt{1 - z^2/R^2} \tag{3.22}$$

After substitution by $z = Rw$, R can be written as $\mathrm{d}z/\mathrm{d}w$ and with $a = \gamma G t R = \tau R$, Eq. 3.21 is equal to:

$$I = 2C \cdot R^2 \cdot \int_0^1 \sqrt{1 - w^2} \cdot \cos(a \cdot w) \cdot \mathrm{d}w \tag{3.23}$$

With the use of the Bessel function (Bronstein and Semendjajew [1981]), this expression can be written as:

$$C' \cdot \frac{J_1(a)}{a} = \frac{C'}{\alpha} \cdot \frac{J_1(\alpha \cdot t)}{t} \tag{3.24}$$

with $\alpha = \gamma G_z r$ and C' a constant. The envelope of the signal $M'(t)$ (Eq. 3.18) can then be simplified to:

$$M_x(t) = \mathrm{const} \cdot \exp(-\frac{t}{T_2}) \cdot \frac{J_1(\alpha \cdot t)}{t} \tag{3.25}$$

- Another way to simplify Eq. 3.18 is done by the assumption that the function $P(\vec{B})$ can be approximated by a Gaussian distribution with standard deviation ΔB:

$$P(\vec{B}) = \frac{1}{\sqrt{2\pi} \cdot \Delta B} \cdot \exp\left(-\frac{B^2}{2\Delta B^2}\right), \tag{3.26}$$

The solution of the integral in Eq. 3.18 with Eq. 3.26 gives:

$$M_x(t) = M_p \cdot \exp(-\frac{t}{T_2} - \frac{\gamma^2 t^2 \Delta B^2}{2}) \cdot \cos(\gamma B_E t) \tag{3.27}$$

Both approaches were experimentally tested and both Eq. 3.25 and 3.27 could model the inhomogeneity of the FID satisfactorily. Because the Gaussian model describes the experimental decay signal slightly better and is mathematically easier to perform, this approach was implemented in the data analysis.

From Eq. 3.27 it can be seen that the inhomogeneity leads to an additional attenuation of the exponential decay of the magnetization by a time dependent factor that can not be represented by an exponential function with time constants since the time t appears quadratic in the additional term. In the further analysis (see chapter 4) this term will be fitted using a parameter DB $= -\gamma^2 \Delta B^2/2$. The values for this parameter and the corresponding value of ΔB for the water sample from figure 3.15 are given in Table 3.2 for the theoretical FID, the FID with shimming and without shimming.

Table 3.2: Values for the parameter DB and ΔB (DB $= -\gamma^2 \Delta B^2/2$) for the theoretical FID, the FID with shimming and without shimming

	DB (-)	ΔB (T)
theoretical FID	0	0
FID with shimming	$1.21 \cdot 10^{-7}$	$1.8 \cdot 10^{-9}$
FID without shimming	$3.61 \cdot 10^{-6}$	$1.0 \cdot 10^{-8}$

To conclude this section it should be noted that the field inhomogeneity is not the only source of signal shortening. Another effect is radiation damping, which occurs when the rotating transverse magnetization of the sample is strong enough to induce a rotating electromotive force in the measuring coil which in turn is strong enough to act significantly back on the sample, leading to a rotation of the magnetization vector. However, Goedecke [1993] showed that within the chosen experimental setup this effect plays only a minor role.

Furthermore, the shimming process will only have an influence on the *external inhomogeneity*, i.e. the inhomogeneity of the measuring field. The *internal inhomogeneity* induced by susceptibility differences within the sample can not be compensated since it can vary strongly from one part of the sample to the other and will depend in a complex way on the sample structure. Although this *internal inhomogeneity* is field dependent and therefore smaller at low fields, the effect is considerable as some experiments with samples with quite a high amount of paramagnetic particles (see section 5.3) showed. The applications of Earth's field NMR by the method of Packard and Varian [1954] are therefore limited to samples without large paramagnetic disturbances.

3.4.1.4 Coil cooling

Because the relaxation times depend on the temperature (Gultekin and Gore [2005]), it is important to keep the temperature of the sample fixed during the measurement. To enlarge the signal to noise ratio, the polarization current is maximized (see Eq. 3.4). Therefore a large amount of electrical power is converted into heat during the polarization time in the coil windings. Without cooling the temperature of the sample would raise dramatically since the sample is not thermally isolated from the coil.

To prevent a strong heating of the coils, each coil is cooled with a centrifugal in-line air fan (Helios, type RR100C, 220 V, 72 W) which blows air on the coils' outer windings. In this way the heating up of the coil during the polarization can be reduced significantly. To measure the effect of the cooling, the temperature of the coil is measured when the coils are supplied with a current of 0.5 A, producing a continuous electrical power of about 18.9 W ($P = RI^2 = 75.6\ \Omega \cdot (0.5\ I)^2$). This corresponds with a standard T_2 measurement where one fourth of the time is used to polarize with 1 A. During the rest of the time the FID is measured and the data are transmitted to a PC. The temporal variation of the coil temperature during such an experiment (derived from the applied voltage to maintain a constant current I during the experiment) is given in figure 3.16 for the case with and without cooling.

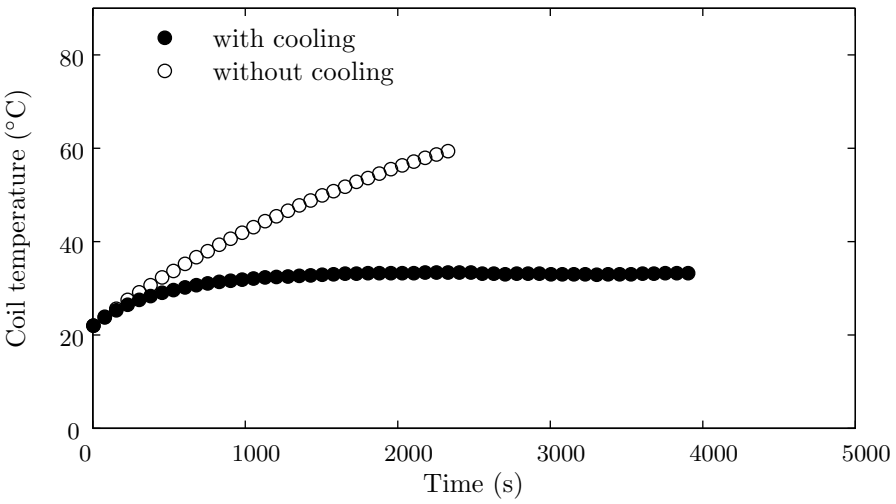

Figure 3.16: Coil temperature in function of time for a continuous electrical power of about 18.9 W with and without cooling.

Without coil cooling, the coil would reach a temperature of about 80 °C after one hour of measurement. The cooling reduces this temperature significantly to about 30 °C. Because the coils are cooled with ambient air at room temperature, this last value will depend on the room temperature.

3.4.1.5 Sample temperating

To maximize the polarization of the sample and the detection of the signal (see section 3.4.1.1), the distance between the sample and the copper windings of the coil is kept small (air slit of 2 mm and 3 mm probe head material, see figure 3.8). Due to this relatively small distance, the air in the slit between sample and coil will warm up and the sample will, after a long measurement time, eventually reach the equilibrium coil temperature ($T_\infty \approx 30$ °C and $T_\infty > 80$ °C with and without cooling respectively). To prevent this unwanted effect (the temperature influences the relaxation times), temperated pressured air is flowing through the air slit with a flow rate of about ± 1 L/s . The air is temperated by two heat exchangers with a total exchange surface of 4660 cm^2. The heat exchangers themselves are temperated by a cooling thermostat (type LAUDA TUK 30) which contains ethylene glycol as cooling liquid. The liquid circulates by a pump via a system of isolated PVC tubes through the heat exchangers and back to the thermostat. The temperature of the circulating fluid is constant and can be regulated by the thermostat from -10 to 90 °C with a resolution of 0.1 °C.

By means of the coil cooling and sample temperating, the temperature of the coil can be set from -5 to +75 °C with a precision of ± 1°C.

3.4.2 In-situ measurements

Additional to the in-vitro probe head, the device can also be connected to an *in-situ* probe head, originally built for *in-vivo* applications (Goedecke [1993]). This in-situ coil has a not clearly definable sample volume. The coil is constructed in a way that a large part of the sensitive volume is located at the outside of the coil. Because the induction outside a coil is smaller than inside, the in-situ coil has larger dimensions than the in-vitro coil in order to achieve a sufficiently large signal to noise ratio. This probe head also consists of a double coil (measurement and compensation coil) to compensate for external disturbances. The dimensions and the experimentally derived (not clearly defined) sensitive volume of the in-situ probe head is displayed in figure 3.17. The characteristics of both coils are given in Table 3.3.

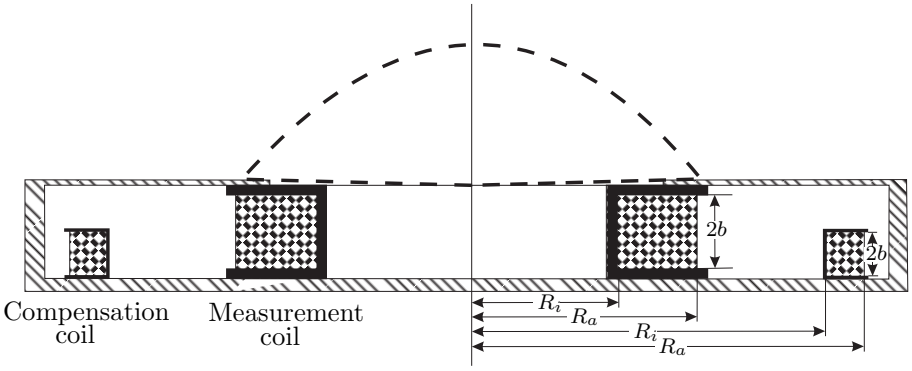

Figure 3.17: Drawing of the in-situ probe head. The sensitive volume of the measurement coil is located within the dashed lines.

Table 3.3: Characteristics of the in-situ probe head.

Measurement coil				
Coil material			PVC	
Winding inner radius	R_i	=	35.0 mm	
Winding outer radius	R_o	=	77.0 mm	
Length	2b	=	30 mm	
Wire diameter	d	=	0.71 mm	
Winding number	n	=	2031	
Winding cross section	F	=	12.6 cm^2	
Total winding area	$n \cdot A$	=	20.95 m^2	
Copper filling factor	f	=	0.64	
Copper mass	m	=	2.53 kg	
Resistance	R	=	31.4 Ω	at 20 ℃
Inductance	L	=	0.396 Hy	
Compensation coil				
Winding inner radius	R_i	=	175 mm	
Winding outer radius	R_o	=	185 mm	
Length	2b	=	15 mm	
Wire diameter	d	=	0.8 mm	
Winding number	n	=	206	
Winding cross section	F	=	1.5 cm^2	
Total winding area	$n \cdot A$	=	20.97 m^2	
Resistance	R	=	7.75 Ω	at 20 ℃
Inductance	L	=	0.308 Hy	
Total probe head				
Housing	$W \cdot H \cdot L$	=	50.2 cm · 5.2 cm · 45 cm	
Resistance	R	=	39.2 Ω	at 20 ℃
Inductance	L	=	0.398 Hy	
Resonance frequency	ν_R	=	13400 Hz	

Since the accessible sensitive volume of this probe head lies outside the coil, this probe head can be used as a *surface NMR scanner*. Recently, different kinds of such unilateral NMR-relaxometers to probe surfaces were introduced, e.g. the *NMR-mouse* (Eidmann et al. [1996]) or *NMR-mole* (Manz et al. [2006]).

Although the length $2b$ of the measuring coil is kept small in order to increase the magnetization in the parts of the sample further away from the coil, the sensitivity will decrease fast with the distance. The field to current ratio can be derived from the Biot-Savart law. The magnetic induction on the axis on a distance d from the center of a circular loop with radius R where a current I is flowing through, can be written as

$$\frac{B}{I} = \frac{\mu_0}{2} \cdot \frac{R^2}{\sqrt{(R^2 + d^2)^3}} \tag{3.28}$$

As explained in section 3.4.1.1, the spatial dependence of the local contribution of the precessing protons to the detected signal can be described by the product of relative sensitivity (normalized by the sensitivity in the center) with the ratio B/I. This product is displayed in figure 3.18 together with the experimental obtained sensitivity. The experimental values are derived by determining the amplitude of the FID (100 accumulations) of a 30 cm × 30 cm × 1 cm volume of water that is moved parallel with the coil front side along the coil axis. Those experimental data are arbitrarily normalized by the value closest to the front side of the probe head.

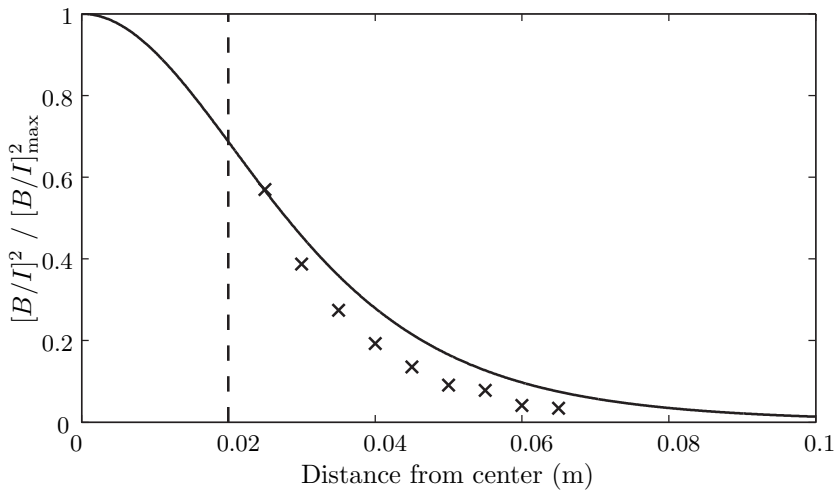

Figure 3.18: The calculated product of relative sensitivity with the ratio B/I in the sample volume ($[B/I]^2$ / $[B/I]^2_{\max}$) in function of the distance from the center on the coil axis ——) together with the experimentally derived values (×, arbitrarily normalized). The area at the left of the dashed line lies within the housing of the probe head and does not belong to the sensitive volume.

From figure 3.18 it becomes clear that the sensitivity of the probe head decreases rapidly with depth. The experimentally derived decrease is even sharper than the calculated spatial

dependence which can be explained by the fact that most of the sample is not located at the coil axis and by a possible influence of the compensation coil on the measurement signal. Due to the rapid decrease, the sensitive area will be limited to the first few centimeters and signal coming from deeper layers will hardly have an effect on the total signal. Because the signal continuously decreases with distance, it is not possible to derive information about the vertical distribution of the signal generating material (water). However, by moving the probe head in the horizontal direction (parallel with the coil front side), information about the horizontal distribution of the material inside the sample can be derived and the NMR device can be used as a surface scanner for proton rich fluids. The experimentally derived lateral resolution of the probe head is given in figure 3.19. The lateral resolution was measured by horizontally moving the coil under a spatial fixed and relatively small sample (a petri-dish with $d = 7$ cm, $h = 2$ cm, filled with water) and measuring the signal amplitude of 20 accumulations.

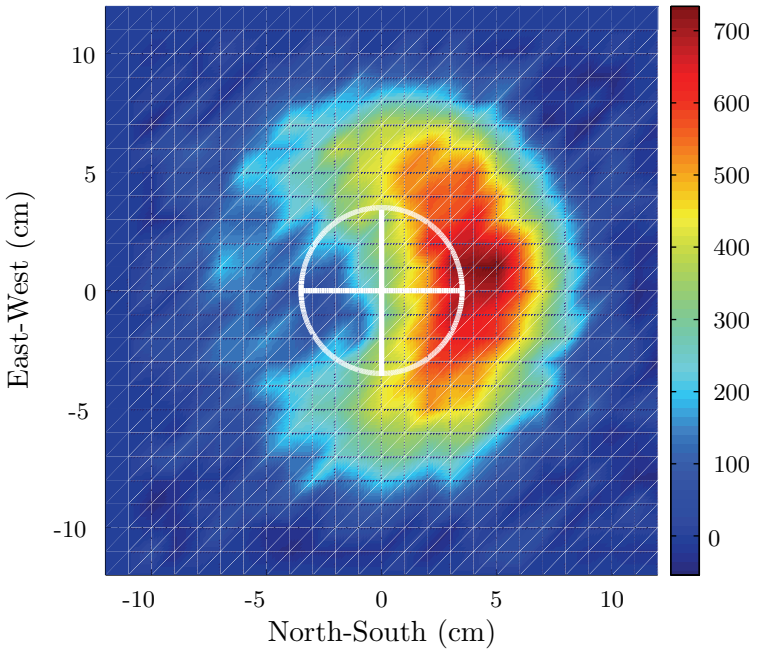

Figure 3.19: The spatial distribution of the intensity of the signal (a.u.) measured with the in-situ probe head. The white circle represents the location of the phantom. The north is pointing to the left.

In figure 3.19 it can be seen that the highest intensity does not correspond to the center of the phantom but is shifted to the right. This is due to the inclination of the Earth's magnetic field. Since the probe head is placed horizontally on the sample, the angle between the polarizing field (this is the vertical direction on the coil axis) and the Earth's magnetic field will not be optimal (i.e. not equal to 90°). The natural inclination of the Earth's magnetic field in Bremen is about 68.5° (see section 3.1). Therefore, the maximum signal amplitude

at the coils axis will be significantly smaller than the local maximum magnetization. This is schematically explained in figure 3.20.

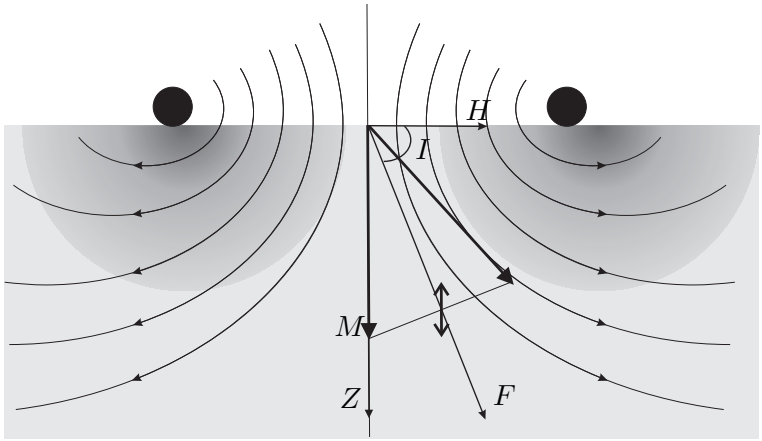

Figure 3.20: The influence of the inclination of the Earth's magnetic field on the signal amplitude for a horizontally orientated polarization and detection coil when the sample is located below the coil surface. The double arrow represents the maximum amplitude of the precessing magnetization and the darkest zones represent the most sensitive regions (see text). With M the precessing magnetization vector, F the Earth's magnetic field vector, H = horizontal component, Z = vertical component, I= inclination.

From the figure it can be seen that the coil is only sensitive for the vertical component of the precessing magnetization. The magnitude of this component depends on the inclination: $M_0 = M_p \cdot \cos^2(I) \approx 0.134 \cdot M_p$. Due to this dependence, the measurement will be impossible to perform in the neighborhood of the magnetic poles of the Earth since at those location the inclination is 90°, leading to a zero vertical component of the precessing magnetization vector. The largest signals will be obtained at the equator where the inclination is 0°, i.e. a maximum precession in the vertical direction. From figure 3.20 it can also be seen that the regions where the field lines from the coil are orthogonal to the direction of the Earth's magnetic field will lead to the largest signals. This means that the most sensitive regions (the dark gray regions in the figure) are lying in the neighborhood of the coil at the north side for the case where the sample is located below the coil. When the sample is located above the coil (as for the experiment illustrated in figure 3.19), the most sensitive regions will be at the south side. This is however only true for an undisturbed Earth's magnetic field. Since the field is disturbed inside the laboratory building, it will be difficult to predict the exact location of the most sensitive regions inside a building.

3.4.3 Signal processing

3.4.3.1 Band width

The measured FID envelope will contain the magnetization signal and some thermal noise. According to the Johnson-Nyquist equation, the level of this noise can be decreased by limiting the band width of the system:

$$u_n = \sqrt{4k_B T R \Delta f} \tag{3.29}$$

with u_n the noise voltage, k_B the Boltzmann constant, T the absolute temperature, R the resistance and Δf the noise band width.

Decreasing the band width in order to improve the signal to noise ratio is however limited by the fact that a small -3dB band width Δf will give a further signal time constant:

$$\tau = \frac{1}{2\pi\Delta f} \tag{3.30}$$

To cope with these two contradictory conditions, the band width is made selectable: $\Delta f =$ 35 Hz or $\Delta f = 100$ Hz. The small band width will suppress more noise but will lead to slower amplitude changes, while the larger band width will pass more noise but will lead to a faster build-up of the signal (see figure 3.21). Additional to those two band widths, the signal can also be measured without a selective band width. However, this alternative will lead to very low signal to noise ratios, and will therefore not be used in this work.

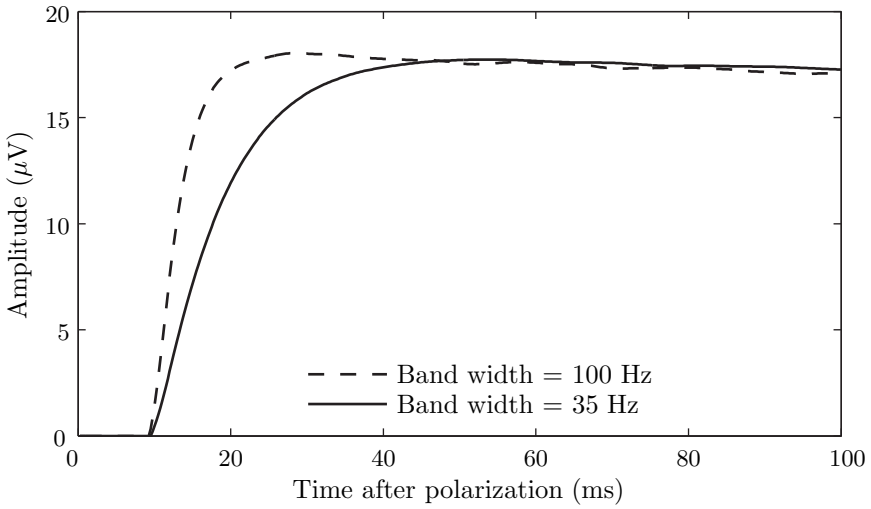

Figure 3.21: Build up of the signal for the band widths of 35 and 100 Hz for 25 ml of water

Since directly after switching off the polarizing field the signal to noise ratio is highest, it is desirable to analyze the signal as soon as possible, especially for systems with short relaxation times. Therefore the build up of the signal has to be modeled in order to distinguish the signal

decay due to relaxation and the superposed influences of the signal delaying systems of the device. Although the time delay of the signal is a result of three in series connected delaying systems (resonance circuit, main amplifier, rms-rectifier-smoothing), each with their own time constant, it can roughly be approximated by one single time constant:

$$1 - e^{-\frac{t-t_0}{\tau}} \tag{3.31}$$

This factor is one component of the function that models the FID envelope (see Eq. 4.59). Since the time constant of the main amplifier will be the largest of the three delaying systems, the overall time constant in Eq. 3.31 will depend almost linearly on the band width of the main amplifier: for the band width of 35 Hz τ is about 9 ms and for the band width of 100 Hz this value is about three times smaller (3 ms).

Additional to the time constant τ, Eq. 3.31 also contains t_0 which describes the time after switching off the polarization current until the signal appears. The physical dead time of the NMR device will be slightly smaller since the polarization will still go on for up to 2 milliseconds after switching off the current, due to the energy released by the coils' self-inductance (coils' back emf). Since the mono-exponential model is only a first approximation for the signal, the extrapolated signal start will change slightly with changing time constant and t_0 also has to be fitted. The value of t_0 is about 10 ms, corresponding with a physical dead time of about 8 ms. This dead time is relatively large compared to any high field NMR machines, but extremely short compared to other Earth's field NMR devices described in the literature (e.g. Bene [1980], Callaghan et al. [1997], Teachspin$^{\mathrm{TM}}$ (`www.teachspin.com`, Feb. 2007).

The length of the dead time has important consequences for measurements of samples with short relaxation times. Due to the delayed build up, the maximum of the FID envelope is reached at around 28 or 20 ms for the bandwidth of 35 Hz or 100 Hz, respectively. The initial amplitude can be derived by extrapolating the amplitude of the FID envelope to the time where the free precession started, i.e. at about 2 ms after switching of the polarization current. For short relaxation times ($T_2 < 10$ ms), the determination of the exact initial amplitude will be difficult because most of the signal has already decayed before the FID envelope is detected. Therefore, the errors in the amplitude determination will increase with decreasing relaxation times. For relaxation times shorter than 10 ms also the determination of the relaxation itself will be accompanied by larger errors. Relaxation times below 5 ms can even not be detected at all with the Earth's field NMR device.

By measuring the initial amplitude of several samples with different relaxation times, it was experimentally found that the initial amplitude depends on the relaxation time: shorter relaxation times lead to higher amplitudes. The relationship between the amplitude and the relaxation rate is studied by analyzing the initial amplitude of a fixed volume of water with different concentrations of $CuSO_4$ ranging from about 0.5 to 60 mmol/l. As already described

by Bloembergen [1957] the addition of paramagnetic ions to water markedly decrease the proton relaxation time. He showed that the relaxation rate of solutions containing paramagnetic ions is proportional to the ion concentration. This can also be seen in figure 3.22. The solid line represents the linear relationship between the relaxation rate measured by the EFNMR device and the concentration of $CuSO_4$ ($R^2 = 0.9998$). This almost perfect linear relationship, as predicted by the theory (Bloembergen [1957]), shows that the EFNMR device is able to measure the correct relaxation times in a broad range (from 10 ms up to 2 s).

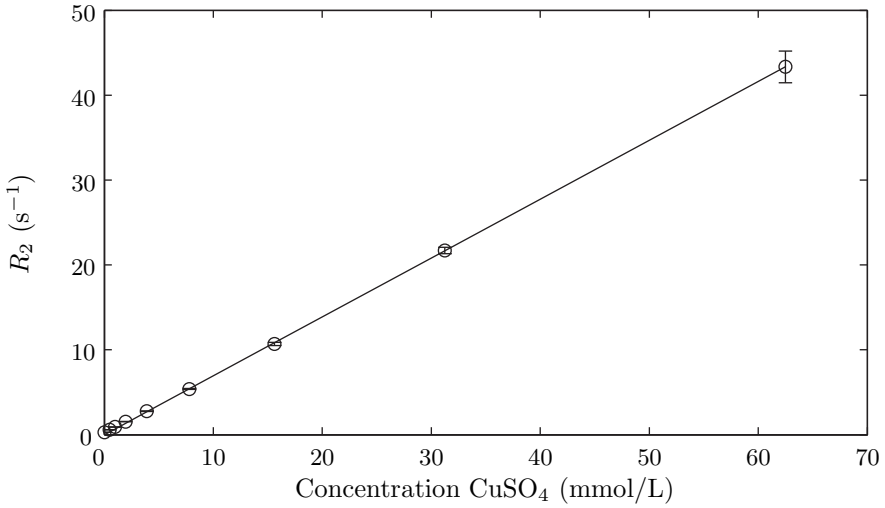

Figure 3.22: The relaxation rate for different concentrations of $CuSO_4$ in 22 ml of water. The solid line represents a linear relationship ($y = 1.39\ x$) with $R^2 = 0.9998$.

In figure 3.23 the ratio of the initial amplitudes (S) and the water content of the sample (V_w) are plotted in function of the relaxation rates. There is a linear relationship for all band widths.

Band width of 35 Hz:

$$\frac{S}{V_w} = 0.0108\ R_2 + 0.918 \quad (R^2 = 0.9954) \tag{3.32}$$

Band width of 100 Hz:

$$\frac{S}{V_w} = 0.0070\ R_2 + 0.916 \quad (R^2 = 0.9971) \tag{3.33}$$

Non selective band width:

$$\frac{S}{V_w} = 0.0031\ R_2 + 0.928 \quad (R^2 = 0.9843) \tag{3.34}$$

The signal dependence on the relaxation time increases strongly with the band width, suggesting that this dependence is caused by the delaying influence of the main amplifier and

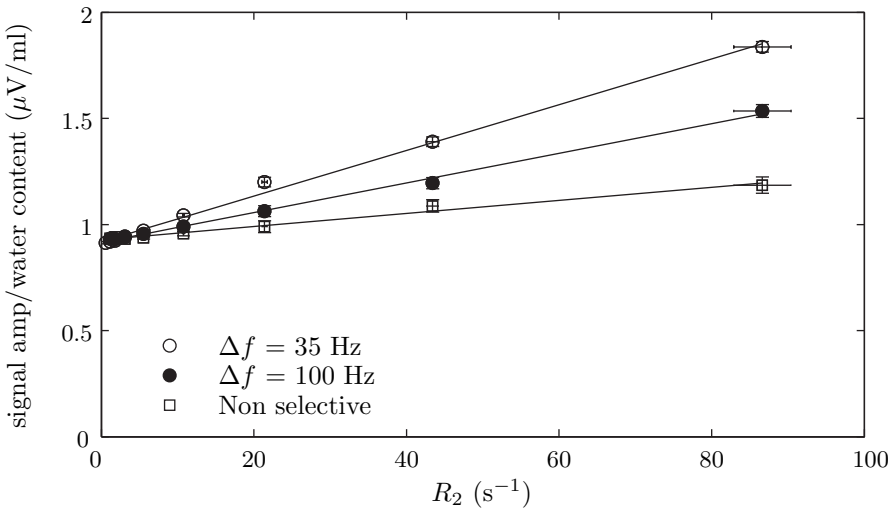

Figure 3.23: The ratio of the initial amplitudes and the water content in function of the relaxation rate of 22 ml of deionised water doped with $CuSO_4$ for all band widths Δf of the main amplifier

some other components of the Earth's field NMR device. To be able to compare amplitudes from samples with different relaxation times, all amplitudes in this work are normalized to amplitudes corresponding with the relaxation rate of bulk water ($R_2 \approx 0.5$ s^{-1}) by using equations 3.32, 3.33 and 3.34.

3.4.3.2 Signal accumulation

As already discussed in section 3.1 the Earth's magnetic field is not constant but varies over time. Additional to the diurnal variation there are also random variations with short periods. This will lead to a stochastic frequency modulation during an FID measurement which will have consequences for the way of signal accumulating. For small variations of the frequency, the output after the amplification is an alternating voltage that contains the signal (S) and some noise components (N):

$$V = S\sin(\omega t) + N\sin(\omega t + \phi) \tag{3.35}$$

To improve the signal to noise ratio, signals can be accumulated. Due to the frequency modulation, the accumulation can not be done by stacking the single FID signals but can only be done after rectification of the oscillating signal. As there exists no synchronous signal the rectification is performed by a root mean square rectifier which first squares the actual value of the voltage before accumulating. Averaging over one Larmor period gives:

$$V_e^2 = \frac{1}{2}\cdot(S^2 + 2SN\cos(\phi) + N^2) \tag{3.36}$$

After accumulation of V_e^2 the square root is taken to get the signal V_e. Due to the accumulation, the term $2SN\cos(\phi)$ in Eq. 3.36 will become negligible. The term N^2 does not disappear but will trend to a value $\overline{N^2}$, the *average noise power*. This value is estimated by averaging over a lot of V_e^2 when there is no signal S (no FID) and is subtracted from V_e^2:

$$U^2 = V_e^2 - \overline{N^2} = \frac{1}{2} \cdot (S^2 + 2SN\cos(\phi) + (N^2 - \overline{N^2})) \tag{3.37}$$

Because $\overline{N^2}$ is only an estimator for the real average noise power N^2 and both will fluctuate themselves, the accumulation of U^2 will be not as efficient as in the case of a synchronous demodulation, especially when N^2 nearly reaches V_e^2.

3.4.3.3 Signal to noise ratio

The average noise power $\overline{N^2}$ can not be used to calculate the signal to noise ratio since Eq. 3.37 contains also the term $2SN\cos(\phi)$. Therefore an empirical value for the noise is derived by calculating the effective average difference between the FID signal and the fit (ΔU) for k data points in the neighborhood of the signal maximum (Goedecke [1993]):

$$\text{Noise} = \sqrt{\frac{1}{k}\sum_{j=1}^{k} \Delta U_j^2} \tag{3.38}$$

To calculate the signal to noise ratio, the maximum value for the fit of the FID signal is divided by this empirical derived noise value. In figure 3.24 the signal to noise ratio is given for 20 successive chronological measurements of 25 ml of a solution of 1000 ppm $CuSO_4$. In figure 3.25 the signal to noise ratio is given in function of the square root of the number of accumulations. Although there is no synchronous demodulation, the signal to noise ratio increases almost linearly with the square root of the number of accumulations. In both figures 3.24 and 3.25 the signal to noise ratio is derived for a sample volume of 25 ml. For smaller volumes, the signal to noise ratio will decrease. However, by increasing the number of accumulations, even for small sample volumes, good data quality can be obtained. In section 5.1.1 it is showed that the EFNMR device is able to measure accurately water contents as small as 0.5 ml.

3.4.4 Data acquisition

The primary control and data acquiring is done by the microprocessor which directly communicates with the electronics of the Earth's field NMR device. When the EFNMR device was built (Goedecke [1993]), controlling and data acquiring was performed by the firmware without the need of an external PC. The input of all parameters was done by an hexadecimal keyboard and all different measurements programs were saved in the firmware. In this work,

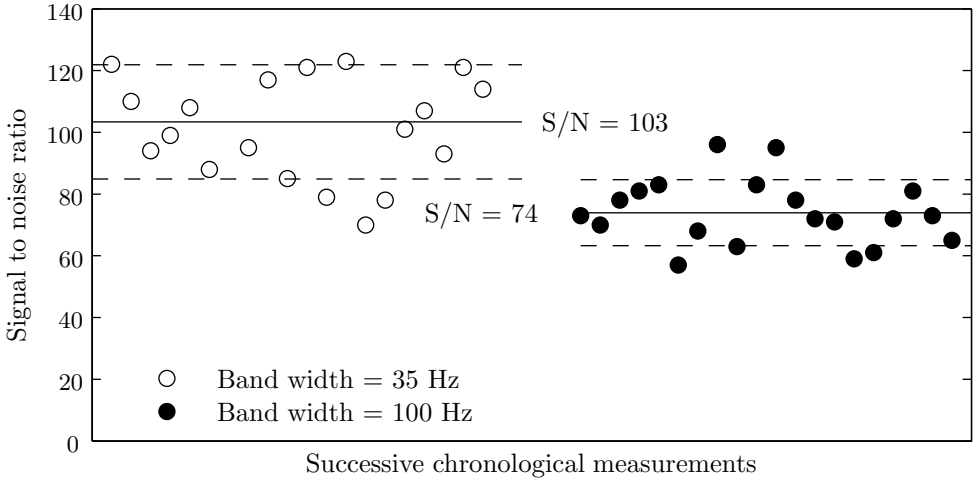

Figure 3.24: The signal to noise ratio for 20 successive chronological measurements for both band widths for 25 ml of a solution of 1000 ppm $CuSO_4$ together with the mean value (——) and the standard deviation (**- - -**)

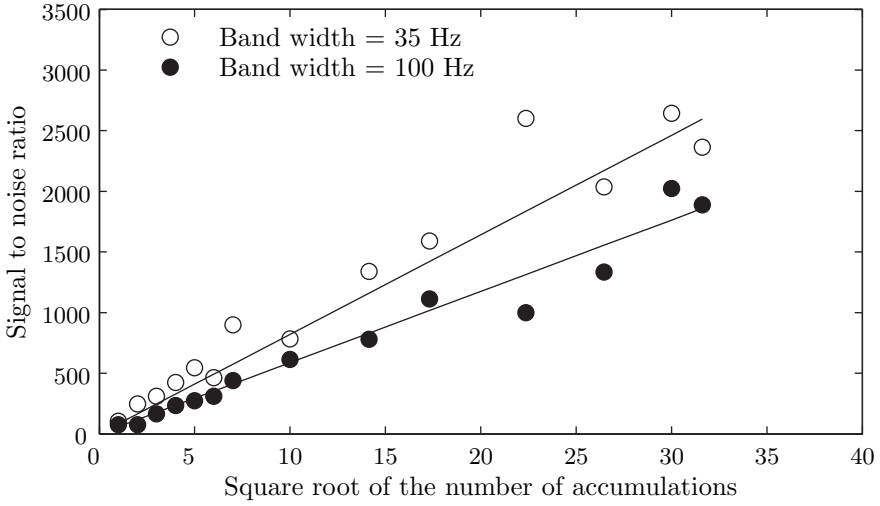

Figure 3.25: The signal to noise ratio in function of the square of the number of accumulations for both band widths for 25 ml of a solution of 1000 ppm $CuSO_4$. The lines represent the expected linear relation.

the NMR device is controlled by a self developed and written PC-software that communicates by means of the serial port (RS232, baud rate 38400). The software is written in Matlab (The Mathworks, Inc. Massachusetts, US) and consists of a Graphical User Interface (GUI) and a collection of underlying scripts with different routines to communicate with the NMR device (setting and reading parameters, starting measurements), control the measurement sequence and analyze the measurement data in different ways. A screen dump of the main

input window of the Earth's field NMR control software is given in figure 3.26.

The custom software allows a very easy and flexible data handling and data analysis. Different kinds of measurement sequences can be applied (see section 4). The use of the PC-software

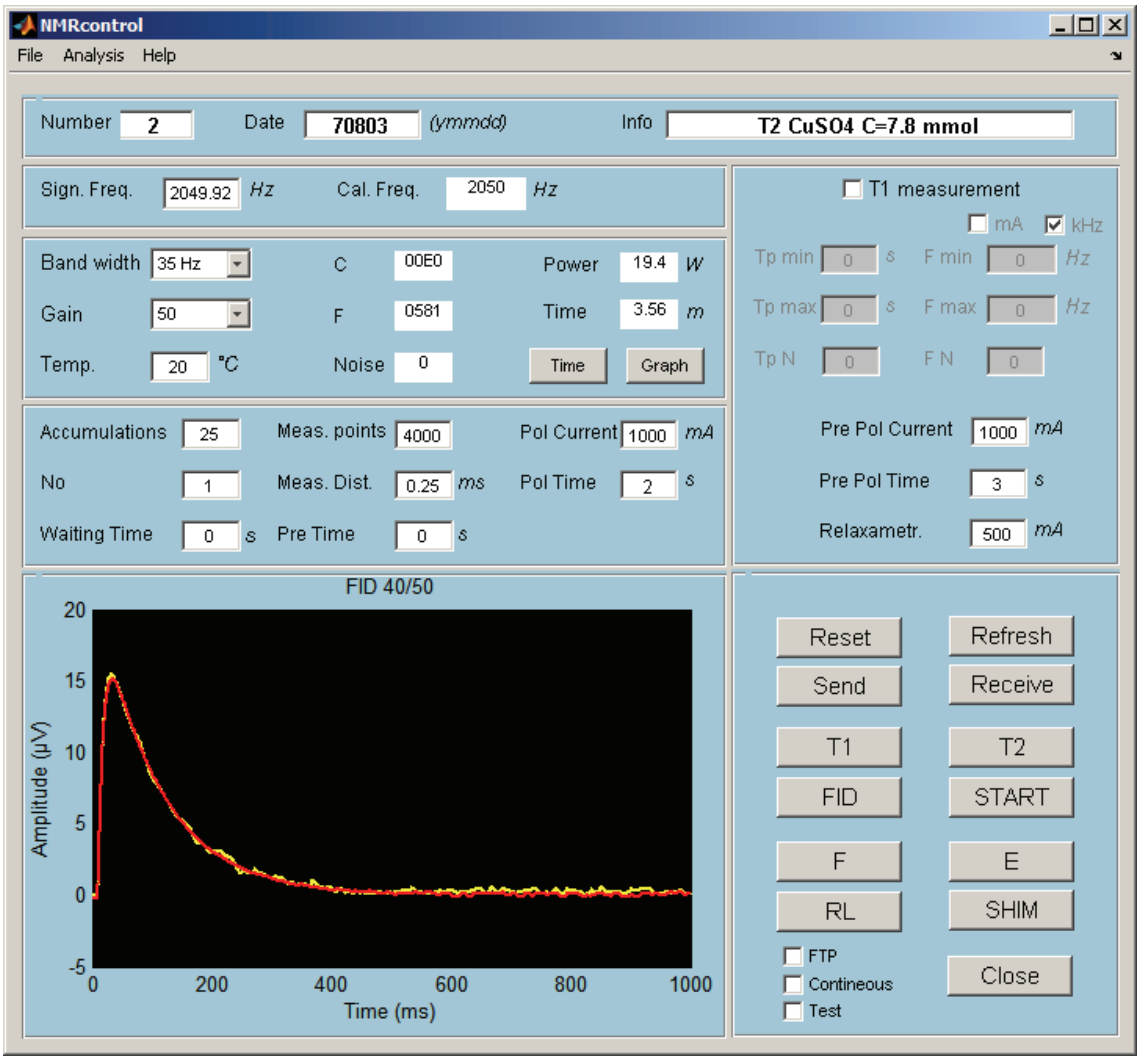

Figure 3.26: Screen dump of the main input window

allows a very high flexibility of the measurement sequences and memory capacity is also not an issue. Furthermore, the GUI allows a fast and easy data analysis with different self-written analysis methods (see section 4). Because the software takes over parts of the firmware programs, not all firmware programs are used anymore. Because the measurement sequences are determined by the PC, a lot of parameters describing those sequences are not transmitted to the NMR device, but only used internally by the software. Every measurement is characterized by a set of parameters that can be separated into four different categories. An overview of all the parameters in those categories is given below:

- Parameters that describe the device settings
  - **Calibration frequency**
    The frequency that is used to tune the input stage and main amplifier.
  - **Signal frequency**
    The measured Larmor frequency.
  - **Band width**
    Determines the 3dB filter band width of the main amplifier. Three settings are possible:
    * 0: none selective mode of the main amplifier
    * 1: nominal 3dB filter band width of 100 Hz
    * 2: nominal 3dB filter band width of 35 Hz

    The selection of the filter band width will influence the time delay of the signal and the signal to noise ratio (see sections 3.4.3.1 and 3.4.3.2).
  - **Gain**
    The amplification factor of the main amplifier. The setting of this value is done by a switch directly on the NMR device. Three settings are possible: 10, 50 and 250.
  - **Capacitor settings**
    A hexadecimal number which binary notation describes the settings of the capacitors of the input stage after tuning. E.g. 0133 represents 0000 0001 0011 0011 which means that capacitor 1, 2, 5, 6 and 9 are switched on.
  - **Resistance settings**
    A hexadecimal number which binary notation describes the settings of the resistors of the main amplifier after tuning in a similar way as the capacitor settings.
- Parameters that describe the measurement sample
  - **Measurement identification**
    A nine digit unique identification of the measurement that contains the measurement date and measurement number (Format: YYMMDD 000).
  - **Sample information**
    A string containing information about the sample.
  - **Temperature**
    The temperature at which the experiment is performed.
  - **Noise power**
    The noise power measured during the last noise measurement
- Parameters that determine the measurement sequence

- **Relaxometry cut off value**
  The polarization current that determines whether the T_1 measurement is done in the normal or in the relaxometry mode (see Figure 3.7). This value is usually equal to $\frac{1}{2}I_{p,max}$.
- **Pre-polarization current (I_{PP})**
  The current that induces the magnetic induction $B_{p,max}$ when T_1 is measured in a low field ($B_p \leq \frac{1}{2}B_{p,max}$): *relaxometry mode* (see figure 3.7). This pre-polarization current will induce a high (maximal) magnetization before the longitudinal relaxation at the low field B_p is measured. This is done to maximize the signal to noise ratio.
- **Pre-polarization time (t_{PP})**
  The time during which the pre-polarization current is applied (see figure 3.7).
- **Polarization current (I_P)**
  The current that induces the field B_p. For T_2 measurements this current should be as high as possible to achieve a high signal to noise ratio. To measure T_1 at different frequencies this current has to be varied. When $B_p \leq \frac{1}{2}B_{p,max}$ the T_1 measurement is performed in the *relaxometry mode*, i.e before the measurement the protons undergo a pre-polarization with maximum B_p. When $B_p > \frac{1}{2}B_{p,max}$ T_1 is measured directly without pre-polarization.
- **Polarization time (t_P)**
  The time during which the polarization current is applied.
- **Accumulations (N)**
  The number of accumulations of an FID at a specific polarization current and time.
- **Measurements cycles (Nz)**
  The number of cycles of accumulations. Before every cycle the average noise power is determined.
- **Number of data points (n)**
  The number of data points of the measured FID. The maximum number is 10000.
- **Sampling rate (r)**
  The distance between two data points (must be multiple of 0.25 ms).
- **Waiting time (t_R)**
  The time the device waits after detection and processing of the signal to start the next measurement cycle. This time ensures a total recovery of the nuclear magnetization and prevents a too strong warming up of the coil. Since the total time between two polarizations is characterized by the detection time and the signal processing time (which depends on the amount of data points), the value for the waiting time depends on the measurement sequence.

- Parameters that describe the measurement sequence
  - **Power**
    The average power of the measurement sequence (calculated from the sequence data). This value is used to estimate heat stress on coil and sample.
  - **Measurement time**
    The duration of the measurement sequence (calculated from the sequence data).

For a T_1 measurement the variation of the polarization time is controlled by three extra parameters: the minimum and maximum value and the number of values. Those parameters are only used to determine the polarization time t_p which is then transmitted to the primary control unit of the NMR device. When T_1 is measured at different frequencies, the variation of the setting of the polarization current is also controlled by a minimum, maximum and number of polarization values.

The custom PC-software communicates with the NMR-control unit by a combination of three basic commands to set the parameters (`MRS`), read the output (`MRR`) and execute program sequences (`MRD`). A complete list of the commands together with the command structure is given in appendix A. Five different program sequences of the firmware written by Goedecke [1993] are used in this work. Every measurement will be a combination of one or more of those program sequences. An overview is given below:

- **Frequency determination**
  This program determines the Larmor frequency after measuring a FID. The polarization current and polarization time have to be set before running this program and a sample has to be put into the measuring coil. The NMR device will perform a polarization and will measure the FID's frequency. For a Larmor frequency of about 2050 Hz the frequency resolution will be about 0.16 Hz.
- **Frequency calibration**
  With this program the input stage and the main amplifier are tuned to a given frequency. This is done by varying the sequence of switched on capacitors or variable resistors respectively. Both sequences are described by the parameters *Capacitor settings* and *Resistance settings*. The Larmor frequency determined with the frequency determination program module should be used as reference value.
- **Noise power determination**
  This program determines the average noise power by recording 16384 data points of the signal envelope during a measurement time of about 10 s. Before the noise power is determined, the NMR device keeps inactive for about 5 s to ensure that all the rest

magnetization still present in the sample has decayed. All the values are squared and the mean value is calculated. The result is used as the best estimator of the actual noise power and is subtracted from every FID signal during the data analysis (see section 3.4.3.2).

- **FID measurement**
  This is the most frequently used program module. During this measurement the sample is polarized with a polarization current I_p during time t_p. When the resulting magnetic induction B_p is smaller than $1/2B_{p,max}$, the sample will be pre-polarized with $B_{P,max}$ during time t_{PP} (see figure 3.7). After the polarization, n data points of the FID envelope are recorded with a sampling rate r and transfered to the PC.

- **Continuous determination of the Larmor frequency**
  With this program module it is possible to measure the Larmor frequency in function of time. Every 3.6 s the Larmor frequency is measured and every 6 minutes the average value over 100 measurements is given out. For a continuous determination of the Larmor frequency a sample with a long transversal relaxation time should be used. The frequency resolution is about 0.08 Hz at a Larmor frequency of 2050 Hz. From the temporal variation of the Larmor frequency information can be derived about the origin of the fluctuations of the magnetic induction in the laboratory. By analyzing the time intervals between the perturbations homogeneous (e.g. cosmic) variations can be separated from inhomogeneous or local variations (see figure 3.3).

From those five program modules, a variety of measurements can be performed. For a typical T_2 measurement the following program sequences are executed: (1) measurement of the Larmor frequency, (2) tuning of the system to this frequency, (3) noise power determination, (4) repetitive measurements of the FID. The number of accumulations depends on the signal to noise ratio of the single FID and of the desired data quality. When a measurement has a large number of accumulations, the noise power can also be measured in between to ensure that a possible change of the background noise is taken into account. After every measurement the FID envelope is digitized and transfered to the PC. When the time the FID is digitized and the transfer time to the PC is not long enough (automatically detected by the software), an extra waiting time has to be inserted to ensure that there is no residual magnetization left from the previous measurement and to prevent excessive heating of the coil. Before the start of every measurement the average power during the measurement is calculated and if necessary decreased by increasing an additional waiting time between two measurements. After the measurement all FID envelopes are squared and summed up by the PC-software. The noise power is subtracted n times where n is the number of accumulations. The square root is taken and from the resulting FID envelope, T_2 is derived (see chapter 4).

A T_1 measurement consists of a collection of FID recordings with varied polarization times t_p

at a given polarization current I_p. When the system is known to have only one single relaxation component that can be estimated well, it is possible to derive the value of T_1 from a small number of FIDs. If the system is expected to have a (broad) relaxation time distribution, up to 100 different values for the polarization time are used to ensure that the time dependence of the components with short relaxation times as well as with long components can be properly described. Usually t_p will range from 10 ms to 10 s. To measure a T_1 dispersion the T_1 measurement described above is repeated with different polarization currents.

Chapter 4

Data analysis

The signal that is recorded by the NMR device is a result of underlying physical processes that determine the relaxation times. In section 2.2 it was shown that the water confined in a pore will have relaxation times that depend on the pore size. Every porous material will have a (narrow or broad) distribution of pore sizes. Since every pore will be associated with a specific relaxation time, the sample will also have a relaxation time distribution. The NMR decay associated with such a continuous distribution of relaxation time constants is often described in the literature in terms of a Laplace transform:

$$y(t) = \int_0^\infty P(T)\, e^{-t/T} dT. \tag{4.1}$$

This Laplace transform is the extension of Eq. 2.25 to a continuous distribution of relaxation times. However, the measured NMR signal will not be purely exponential due to the experimental conditions such as the influence of the inhomogeneity and the non ideal response function of the device (see section 4.1.1). Therefore a more general form of the Laplace transform, the Fredholm integral of the first kind

$$y(t) = \int_{T_{min}}^{T_{max}} P(T)\, f(t,T)\, dT, \tag{4.2}$$

will be more suitable to describe the behavior of the NMR signal since the function $f(t,T)$ (the kernel function) may adopt different forms (Press et al. [2002]). Given the NMR data $y(t)$, the aim in solving Eqs. 4.1 and 4.2 is the determination of the function $P(T)$. Since it is not possible to derive a continuous function $P(T)$ from a finite number of discrete values of $y(t)$, $P(T)$ will be discretized, so that we can write Eq. 4.2 as

$$y(t) = \sum_{T_{min}}^{T_{max}} P(T_i)\, f(t,T_i), \tag{4.3}$$

which can also be written in matrix notation:

$$y = \boldsymbol{A}x + \epsilon \tag{4.4}$$

where y is the vector of experimental values, x the discrete approximation of $P(T_i)$, $\boldsymbol{A}$ represents the kernel function $f(t, T_i)$, and ϵ are the unknown noise components. Deriving x from Eq. 4.4 belongs to the general class of inverse problems and will be discussed in the following sections for T_2- and T_1-measurements.

4.1 T_2 measurements

4.1.1 The Kernel function $\boldsymbol{A}$

In Eq. 4.4 $\boldsymbol{A}$ only depends on the measurement time t and the time constants T_i (transversal relaxation times). However, the FID signal measured by the Earth's field NMR device will also depend on experimental conditions such as the response function of the device and the residual inhomogeneity:

- To decrease the noise of the signal the band width of the main amplifier is kept rather small (-3dB-band width of 35 Hz or 100 Hz) and therefore the signal will not appear immediately after switching off the polarizing field (see section 3.4.3). The transient effect can be modeled by a factor (Eq. 3.31)

$$1 - e^{-\frac{t-t_0}{\tau}}$$

- As already explained in section 3.4.1.3 for systems with long relaxation times, the influence of the external inhomogeneity on the FID can not be neglected and has to be taken into account by a factor

$$e^{-DB \cdot t^2} \qquad \text{with } DB = \gamma^2 \Delta B^2 / 2$$

These experimental factors will influence the signal shape and have to be taken into account before further analyzing the signal. The part of the signal that will only depend on the underlying physical properties of the measured system can be written as:

$$y'(t) = \frac{y(t)}{(1 - e^{-\frac{t-t_0}{\tau}}) \cdot e^{-DB \cdot t^2}} \tag{4.5}$$

Only this part of the signal will be analyzed in terms of expression 4.4 and can then be written as:

$$y'(t) = \boldsymbol{A} \cdot x + \epsilon \tag{4.6}$$

with

$$\boldsymbol{A} = \begin{bmatrix} e^{-\frac{t_1}{T_{2,1}}} & e^{-\frac{t_1}{T_{2,2}}} & \cdots & e^{-\frac{t_1}{T_{2,n}}} \\ e^{-\frac{t_2}{T_{2,1}}} & e^{-\frac{t_2}{T_{2,2}}} & \cdots & e^{-\frac{t_1}{T_{2,n}}} \\ \vdots & \vdots & \ddots & \vdots \\ e^{-\frac{t_m}{T_{2,1}}} & e^{-\frac{t_m}{T_{2,2}}} & \cdots & e^{-\frac{t_m}{T_{2,n}}} \end{bmatrix} \tag{4.7}$$

and

$$x = [a_1 \quad a_2 \quad \cdots \quad a_n] \tag{4.8}$$

and where m represents the number of data points and n the number of discrete relaxation times. a_i are the weighting factors of the m time constants and determine the relaxation time distribution. The transformed data vector from Eq. 4.5 will be for simplicity denoted y in the following sections where it will be explained how x can be determined when y and $\boldsymbol{A}$ are known. How the values for t_0, τ and DB are determined will be explained in section 4.1.9.

4.1.2 The least squares solution

Because in general there will be more measurements y_i than unknown variables x_i, Eq. 4.4 will be over-determined. This means that there is no exact solution. A *good* solution in this case will be a solution with the minimal deviation between the model and the data points. When we call the difference between the data and the theoretical model $e = \boldsymbol{A}x - y$, obtaining the best solution can be done by minimizing the Euclidean norm of the vector e:

$$\|e\|_2 = \sqrt{e^T e} \tag{4.9}$$

or rather the square of it:

$$\begin{aligned} \chi^2 &= e^T e \\ &= (\boldsymbol{A}x - y)^T (\boldsymbol{A}x - y) \\ &= x^T \boldsymbol{A}^T \boldsymbol{A}x - x^T \boldsymbol{A}^T y - y^T \boldsymbol{A}x + y^T y \end{aligned} \tag{4.10}$$

In the derivation of Eq. 4.10 we assumed that the relative errors are the same for all data points and that they are uncorrelated. Minimization of this expression will lead to the well known *least square solution*. To minimize Eq. 4.10 the first derivative of it has to be equal to zero:

$$\begin{aligned} \frac{\partial \chi^2 [x]}{\partial x_k} &= I_k^T \boldsymbol{A}^T \boldsymbol{A}x + x^T \boldsymbol{A}^T \boldsymbol{A} I_k - I_k^T \boldsymbol{A}^T y - y^T \boldsymbol{A} I_k \\ &= I_k^T \left(\boldsymbol{A}^T \boldsymbol{A}x - \boldsymbol{A}^T y\right) + \left(x^T \boldsymbol{A}^T \boldsymbol{A} - y^T \boldsymbol{A}\right) I_k \\ &= I_k^T \left(\boldsymbol{A}^T \boldsymbol{A}x - \boldsymbol{A}^T y\right) + \left(\boldsymbol{A}^T \boldsymbol{A}x - \boldsymbol{A}^T y\right)^T I_k \\ &= 2 I_k^T \left(\boldsymbol{A}^T \boldsymbol{A}x - \boldsymbol{A}^T y\right) \end{aligned} \tag{4.11}$$

with I_k equal to the k^{th} unit vector.

Setting this expression equal to zero leads to the least squares solution $\widehat{x}$:

$$\boldsymbol{A}^T \boldsymbol{A}\widehat{x} - \boldsymbol{A}^T y = 0 \tag{4.12}$$

or, solved for $\widehat{x}$:

$$\widehat{x} = \left(\boldsymbol{A}^T \boldsymbol{A}\right)^{-1} \boldsymbol{A}^T y \tag{4.13}$$

This is the so called *normal equation* which gives the condition that must be fulfilled to obtain the least square solution of $\boldsymbol{A}x = y$. The solution is denoted $\widehat{x}$ and not x because there is no x that solves this set of linear equations exactly. $\widehat{x}$ is only the best estimation in terms of the least squares. To solve the normal equation the inverse of $\boldsymbol{A}^T \boldsymbol{A}$ has to be derived. When $\boldsymbol{A}^T \boldsymbol{A}$ is a singular matrix, this will not be possible. A more general way to solve Eq. 4.13 is to derive $\widehat{x}$ based on the singular value decomposition (SVD) of the matrix $\boldsymbol{A}$ and will be explained in the next section.

4.1.3 Singular value decomposition

Any $m \times n$ matrix $\boldsymbol{A}$ whose number of rows m is greater than or equal to the number of columns n, can be written as the product of an $m \times n$ column-orthogonal matrix $\boldsymbol{U}$, an $n \times n$ diagonal matrix $\boldsymbol{S}$ with positive or zero elements (the *singular values*), and the transpose of an $n \times n$ orthogonal matrix $\boldsymbol{V}$:

$$\boldsymbol{A} = \boldsymbol{U} \cdot \boldsymbol{S} \cdot \boldsymbol{V}^T \tag{4.14}$$

The column vectors u_i (*left singular vectors*) and v_i (*right singular vectors*) of $\boldsymbol{U}$ and $\boldsymbol{V}$ form an orthonormal base of the m-dimensional data space and the n-dimensional parameter space respectively. The vectors v_i corresponding to zero singular values form a basis for the nullspace of $\boldsymbol{A}$: $\text{Null}\,(\boldsymbol{A}) = \{v | A \cdot v = 0\}$.

When p is the number of non zero singular values (p = rank of matrix $\boldsymbol{A}$), $\boldsymbol{A}$ can be also written as:

$$\boldsymbol{A} = \boldsymbol{U}_p \cdot \boldsymbol{S}_p \cdot \boldsymbol{V}_p^T, \tag{4.15}$$

where the $m \times p$ matrix $\boldsymbol{U}_p$, the $p \times p$ matrix $\boldsymbol{S}_p$ and the $n \times p$ matrix $\boldsymbol{V}_p$ are formed by removing the $n - p$ last columns (corresponding to zero singular values) of $\boldsymbol{U}$, $\boldsymbol{S}$ and $\boldsymbol{V}$ respectively.

Substituting Eq. 4.15 in the normal equation and taking into account the orthogonality of $\boldsymbol{U}_p$ and $\boldsymbol{V}_p$ ($\boldsymbol{U}_p^T \boldsymbol{U}_p = \boldsymbol{V}_p \boldsymbol{V}_p^T = I_p$) gives:

$$\widehat{x} = \boldsymbol{V}_p \boldsymbol{S}_p^{-1} \boldsymbol{U}_p^T y = \sum_{i=1}^{p} \frac{u_i^T y}{s_i} v_i \tag{4.16}$$

The matrix $\boldsymbol{V}_p \boldsymbol{S}_p^{-1} \boldsymbol{U}_p^T$ is also called *pseudo inverse* matrix of $\boldsymbol{A}$. Applied to the equation $\boldsymbol{A}x = y - \epsilon$, it gives the smallest least square solution, often called the *principal solution*. When matrix $\boldsymbol{A}$ has full rank (no zero singular values) the pseudo inverse is equal to $\left(\boldsymbol{A}^T \boldsymbol{A}\right)^{-1} \boldsymbol{A}^T$ since it is constructed to fulfill the normal equation. In this case the least square solution is unique. The pseudo inverse matrix is thus a generalization of the inverse matrix for non-regular matrices (matrices with zero singular values). For such matrices $\widehat{x}$ will not be the only solution of the normal equation. Every $x = \widehat{x} + x'$ with $\boldsymbol{A}x' = 0$ (x' is a member of the nullspace) will also fulfill the normal equations and can be very different from the true solution x.

4.1.4 Ill-posed problems

Performing a singular value decomposition on the kernel $\boldsymbol{A}$ of the Fredholm equation of the first kind will reveal following characteristics (Hansen [1994]):

- The singular values s_i ordered by magnitude decay gradually to zero (without reaching zero) with no particular gap in the spectrum. An increase of the dimensions of $\boldsymbol{A}$ will increase the number of small singular values.
- The vectors u_i and v_i tend to have more sign changes in their elements as the index i increases, i.e., as s_i (the singular value) decreases.

To illustrate those characteristics, data of a simulated T_2 experiment are examined. We assume that the FID envelope consists of 40 discrete values uniformly spread between 10 ms and 1 s. The distribution of relaxation times has 100 different time constants uniformly spread between 10 ms and 10 s in a logarithmic domain. From the FID envelope the underlying distribution (displayed in figure 4.1(b)) has to be determined, i.e. solving equation 4.4 for x. Figure 4.1 (a) shows the singular values s_i which decrease rapidly as i increases. A few of the right singular vectors v_i and left singular vectors u_i are shown in figure 4.1(c) and (d) respectively. All singular vectors except the first one are oscillatory and the number of nodes (zero crossings) equals i. Thus, the higher-order singular vectors are more oscillatory (Provencher [1982b]). Figure 4.1(b) shows the model spectrum of relaxation times (thick line). The spectrum reconstructed with 3 (thin solid line), 5 (dotted line), 8 (dashed line) and 10 (dot-dashed line) singular vectors are also plotted. The spectrum is artificially broad and biased when only 3 or 5 singular vectors are considered in the reconstruction. On the other hand, when 10 singular values are used, the reconstructed spectrum is narrower and fit the model spectrum quite well. However, due to the inclusion of singular vectors v_i with small s_i, it can be unstable (Song et al. [2005]). Since negative components in the relaxation time distribution are not possible, it is clear that this last spectrum can not be physically

correct. In order to allow only positive or zero amplitudes, a non-negative constraint will be implemented in the analysis (see section 4.1.7).

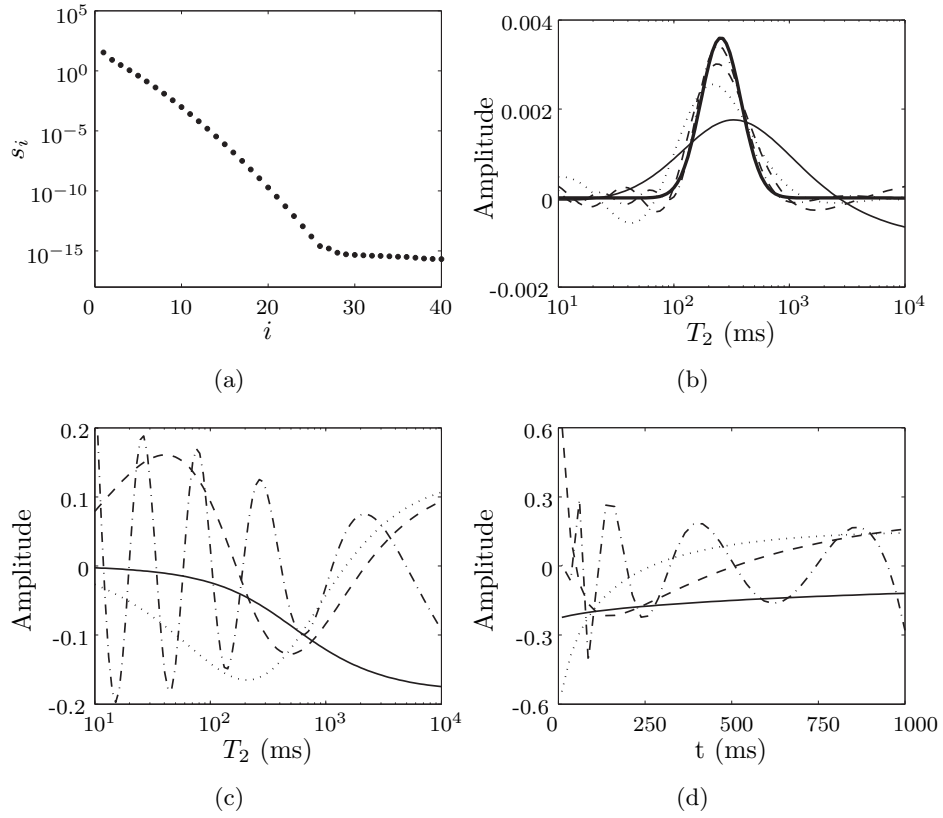

Figure 4.1: Singular value decomposition of the exponential kernel $\boldsymbol{A}$ with 100 time constants uniformly spaced logarithmically between 10 and 10^4 ms. (a) The singular values of A. (b) The model spectrum (thick solid line) together with the spectra reconstructed with 3 (thin solid line), 5 (dotted line), 8 (dashed line) and 10 (dot-dashed line) singular vectors. (c,d) Plot of the right singular vectors v_i and left singular vectors u_i for $i = 1, 2, 3$ and 10 plotted in solid, dotted, dashed and dot-dashed lines (modified after Song et al. [2005]).

The two characteristics listed above will make $\boldsymbol{A}$ extremely *ill-conditioned*. The *condition* associated with the linear equation $\boldsymbol{A}x = y$ indicates how strong inaccurate data (e.g. by noise) can disturb the solution. The condition number can be expressed as the ratio of the largest to smallest singular value of the matrix:

$$cond(\boldsymbol{A}) = s_1/s_p. \tag{4.17}$$

Since the singular values of Fredholm equations of the first kind will decrease gradually, $\boldsymbol{A}$ will be extremely ill-conditioned ($\text{cond}(\boldsymbol{A}) = 2.3 \cdot 10^{17}$ for the example shown in figure 4.1). A small disturbance in the data vector y can therefore lead to huge changes in $\widehat{x}$. This

means that a large number of solution exists, all satisfying Eq. 4.4 and compatible with the data within the experimental error (Provencher [1982a]). Solving $\widehat{x}$ by equation 4.16 will be problematic since the small singular values will be numerically equal to zero. Furthermore those small singular values will correspond to strong oscillating singular vectors (due to the many sign changes) and characterize subtle structures, not influencing the general trend.

Another aspect of ill-posed problems related with the oscillatory character of the singular vectors corresponding with small singular values is the smoothing effect. Using the SVD we can decompose an arbitrary vector x in

$$x = \sum_{i=1}^{n} \left(v_i^T x\right) v_i. \tag{4.18}$$

Considering the mapping $\boldsymbol{A}x$ knowing $\boldsymbol{A}v_i = s_i u_i$, we get

$$\boldsymbol{A}x = \sum_{i=1}^{n} s_i \left(v_i^T x\right) u_i \tag{4.19}$$

Due to the multiplication with the singular values the high-frequency components of x will be more damped in $\boldsymbol{A}$ than low-frequency components. For the inverse problem (computing x from $\boldsymbol{A}x = y$) the opposite effect will occur: the high-frequency oscillations will be amplified in the right-hand side y, making the least square solution highly unstable.

Although exponential ill-posed problems have full rank (no singular values are equal to zero), in praxis they are under determined (the singular values decay gradually to zero). A possible solution to solve such kind of problems would therefore be to set the very small singular values equal to zero and only leave over the p largest values (Meyer [2000]). The solution would look then like Eq. 4.16 which can also be written as

$$\widehat{x} = \sum_{i=1}^{n} F_p(s_i) \frac{u_i^T y}{s_i} v_i \tag{4.20}$$

with $F_p\left(s_i\right)$ a *filter factor*:

$$F_p\left(s_i\right) = \begin{cases} 0: & i \leq p \\ 1: & i > p \end{cases} \tag{4.21}$$

This solution can thus be interpreted as a low pass filter since the high frequency fractions corresponding to the small singular values are filtered out and only the general structure is left over. This can be seen in figure 4.1(b). For low values of p (3 or 5) only the general shape of the spectrum can be reconstructed. When using a larger value for p (e.g. 10) the spectrum is modeled quite well but gets unstable.

Due to the gradual decay of the singular values (see figure 4.1(a), it is difficult to choose an appropriate cut-off value for p. When p is chosen too small, the solution will hardly have any

structure. Too large values for p however, will lead to wildly oscillating solutions. To overcome this problem, the solution can be *regularized* until the desired level of detail is reached. This imposes, of course, that the general structure of the solution is known *a priori*.

4.1.5 Regularization

Our problem can thus be solved by *regularization* to get an unambiguous solution. This is done by considering a second quadratic functional of x additional to $\chi^2[x]$, containing some *a priori* information about x. If we have the two random quadratic functionals $\mathcal{A}[x]$ and $\mathcal{B}[x]$, we can try to determine x by either minimizing $\mathcal{A}[x]$ subject to the constraint that $\mathcal{B}[x]$ has some particular value b or minimizing $\mathcal{B}[x]$ subject to the constraint that $\mathcal{A}[x]$ has some particular value a. Applying the method of Lagrange multipliers (Press et al. [2002]) for the first case gives

$$\frac{\delta}{\delta x}\left(\mathcal{A}[x] + \lambda_1\left(\mathcal{B}[x] - b\right)\right) = \frac{\delta}{\delta x}\left(\mathcal{A}[x] + \lambda_1\mathcal{B}[x]\right) = 0, \tag{4.22}$$

and for the second case

$$\frac{\delta}{\delta x}\left(\mathcal{B}[x] + \lambda_2\left(\mathcal{A}[x] - a\right)\right) = \frac{\delta}{\delta x}\left(\mathcal{B}[x] + \lambda_2\mathcal{A}[x]\right) = 0. \tag{4.23}$$

Both equations are identical when we set $\alpha = \lambda_1 = 1/\lambda_2$ The solutions of both forms depend now on one parameter α. Depending on the value of α, all solutions will vary along a so-called *trade-off* curve between the problem of minimizing $\mathcal{A}$ and the problem of minimizing $\mathcal{B}$ (see figure 4.2). Both problems will of course generate different answers. When for $\mathcal{A}$ the deviation of χ^2 is taken, minimizing $\mathcal{A}$ will result in the least square solution. As discussed above this solution can become unstable, wildly oscillating, or in other ways unrealistic. When $\mathcal{B}$ represents some a priori knowledge, e.g. about the smoothness of the solution, minimizing $\mathcal{B}$ by itself will give a solution that is smooth and has nothing at all to do with the measured data. $\mathcal{B}$ is called *stabilizing functional* or *regularizing operator*. By varying the parameter α we can find a compromise between a good agreement with the measured data and with our a priori knowledge. This solution will be a unique solution if we choose a nondegenerate quadratic form for $\mathcal{B}$ since the sum of a degenerate quadratic form ($\mathcal{A}$) with a nondegenerate quadratic form results in a nondegenerate quadratic form.

When $\mathcal{A}[x] = \|\boldsymbol{A}x - y\|$ and $\mathcal{B}[x] = \|\boldsymbol{B}x - b\|$, the minimization problem can be expressed as

$$\min\Big(\quad \|\boldsymbol{A}x - y\|^2 + \alpha\,\|\boldsymbol{B}x - b\|^2\Big) \tag{4.24}$$

This can be solved in the same way as for Eq. 4.11:

$$\left(\boldsymbol{A}^T\boldsymbol{A} + \alpha\boldsymbol{B}^T\boldsymbol{B}\right)\widehat{x} = \boldsymbol{A}^T y + \alpha\boldsymbol{B}^T b \tag{4.25}$$

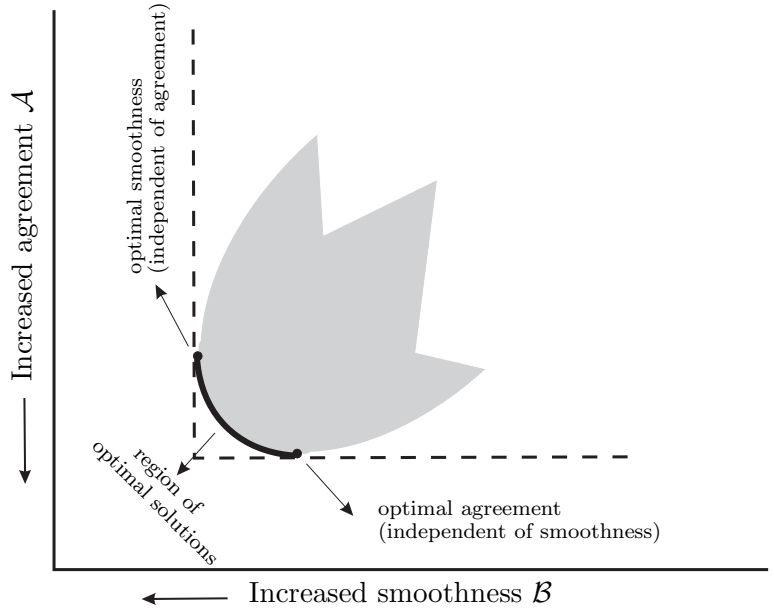

Figure 4.2: The inverse problem as a trade-off between two different optimizations: agreement between data and solution by a least square fit ($\mathcal{A}$) and smoothness or stability of the solution ($\mathcal{B}$). The shaded region represents all possible solutions. The curve connecting the unconstrained minimum of $\mathcal{A}$ and the unconstrained minimum of $\mathcal{B}$ represent the best solutions since all other solution have, for a specific optimization $\mathcal{A}$ a better optimization $\mathcal{B}$ on the curve and vice versa. (Adapted after Press et al. [2002])

or solved for $\widehat{x}$:

$$\widehat{x} = \left(\boldsymbol{A}^T\boldsymbol{A} + \alpha\boldsymbol{B}^T\boldsymbol{B}\right)^{-1}\left(\boldsymbol{A}^T y + \alpha\boldsymbol{B}^T b\right) \tag{4.26}$$

This very general form can be further simplified when the *a priori* knowledge is specified. If the matrix $\boldsymbol{B}$ is equal to the identity the solution reduces to the so-called Levenberg-Marquardt expression, or zeroth order regularization ($b = 0$):

$$\widehat{x} = \left(\boldsymbol{A}^T\boldsymbol{A} + \alpha I\right)^{-1}\boldsymbol{A}^T y, \tag{4.27}$$

which will lead to a solution where the norm of $\widehat{x}$ ($\|\widehat{x}\|^2$) is also minimized.

If $\boldsymbol{B}$ is the first derivative matrix, the regularization is called to be of first order. In the first order regularization, the first derivative of the solution $\widehat{x}$ is minimized. This means that minimizing $\mathcal{B}$ will lead to a *smooth* solution. $\mathcal{B}$ can then be written as:

$$\mathcal{B} \propto \int \left[\widehat{x}'\right]^2 dx \tag{4.28}$$

When the individual elements of the solution vector $\widehat{x}$ are uniformly spaced, we can write this as

$$\mathcal{B} \propto \sum_{k=1}^{m-1} \left[\widehat{x}_k - \widehat{x}_{k+1}\right]^2 = \|\boldsymbol{B}\cdot\widehat{x}\|^2 \tag{4.29}$$

where $\boldsymbol{B}$ is the $(m-1) \times m$ first difference matrix (with m the length of vector $\widehat{x}$)

$$\boldsymbol{B} = \begin{bmatrix} -1 & 1 & 0 & 0 & 0 & 0 & 0 & \dots & 0 \\ 0 & -1 & 1 & 0 & 0 & 0 & 0 & \dots & 0 \\ \vdots & & & & \ddots & & & & \vdots \\ 0 & \dots & 0 & 0 & 0 & 0 & -1 & 1 & 0 \\ 0 & \dots & 0 & 0 & 0 & 0 & 0 & -1 & 1 \end{bmatrix} \tag{4.30}$$

and the product $\boldsymbol{B}^T\boldsymbol{B}$ is then equal to an $m \times m$ matrix

$$\boldsymbol{B}^T\boldsymbol{B} = \begin{bmatrix} -1 & -1 & 0 & 0 & 0 & 0 & 0 & \dots & 0 \\ -1 & 2 & -1 & 0 & 0 & 0 & 0 & \dots & 0 \\ 0 & -1 & 2 & -1 & 0 & 0 & 0 & \dots & 0 \\ \vdots & & & & \ddots & & & & \vdots \\ 0 & \dots & 0 & 0 & 0 & -1 & 2 & -1 & 0 \\ 0 & \dots & 0 & 0 & 0 & 0 & -1 & 2 & -1 \\ 0 & \dots & 0 & 0 & 0 & 0 & 0 & -1 & 1 \end{bmatrix} \tag{4.31}$$

so that Eq. 4.26 can be written as:

$$\widehat{x} = \left(\boldsymbol{A}^T\boldsymbol{A} + \alpha\boldsymbol{B}^T\boldsymbol{B}\right)^{-1}\boldsymbol{A}^T y \tag{4.32}$$

In analogy to Eq. 4.21, the different regularization expressions can also be written in function of a filter factor (Song et al. [2005]):

$$\widehat{x} = \sum_{i=1}^{n} F_p(s_i)\frac{u_i^T y}{s_i} v_i \quad \text{with} \quad F_p\left(s_i\right) = \frac{s_i^2}{s_i^2 + \alpha^2} \tag{4.33}$$

This filter factor will suppress singular values that are small in comparison with α^2 and the corresponding strong oscillating singular vectors are filtered out. Singular values that are large in comparison to α^2 are almost not changed so that the slowly changing components of the solution are well reproduced. By varying the regularization parameter α the suppression of the wildly oscillating fractions can be continuously adjusted.

4.1.6 Regularization parameter

Solving Eq. 4.32 for a particular value of α will give us a unique solution. A critical step in the solution of the minimization problem is a most adequate choice for the value of α, since it will determine how our solution will look like. Three different methods to determine an *appropriate* value for the regularization parameter will be discussed below.

- A value for α said to give a balance between closeness to the experimental data and the a priori knowledge is given by (Press et al. [2002]):

$$\alpha = \mathrm{Tr}\left(\boldsymbol{A}^T\boldsymbol{A}\right)/\mathrm{Tr}\left(\boldsymbol{B}^T\boldsymbol{B}\right). \tag{4.34}$$

  Since this value does not depend on the quality of the experimental data, this value is clearly not the optimum value for α. It can however be used as a starting value from which the minimization can be further regulated.

- Hansen [1994] describes a graphical tool for the analysis of ill-posed problems, the so called *L-curve* which is a plot (for all valid regularization parameters) of the (semi)norm $\|\boldsymbol{B}x\|^2$ of the regularized solution versus the corresponding residual norm $\|\boldsymbol{A}x - y\|^2$. When those two norms are plotted in *log-log* scale, an L-shaped curve appears with a distinct corner separating the vertical and the horizontal parts of the curve (see figure 4.3). Those two different regions are the result of two different kinds of underlying errors of the minimization. When x_0 is the true solution, the error $x - x_0$ consists of two compounds, namely, a perturbation error from the error ϵ in the data vector y, and a regularization error due to the regularization of the error-free component of y. The vertical part of the curve corresponds to solution where $\|\boldsymbol{B}x\|^2$ is very sensitive to changes in the regularization parameter because the perturbation error ϵ dominates. The horizontal part of the curve corresponds to solutions where it is the residual norm $\|\boldsymbol{A}x - y\|^2$ that is most sensitive to the regularization parameter because $\widehat{x}$ is dominated by the regularization error.

  Hansen [1994] showed that the optimum value for the regularization parameter is not far from the regularization parameter that corresponds to the L-curve's corner. Because this method assumes that the regularized solution is a linear low-pass-filtered version of the actual distribution, the L-curve's corner can be sometimes quite different from the optimum value of the regularization parameter since the solution of our inverse problem has some non-linear constraints (e.g. the non-negativity constraint).

- An optimum value for the regularization parameter is the smallest one that renders an acceptable reproducible estimate of the distribution function. Clearly this preferred value depends on the magnitude of the measurement errors and the data. An *ad hoc* algorithm is described by Fordham et al. [1995] that finds a suitable value of α based on the *log-log* graph of the fit error

$$\chi(\alpha) = \|\boldsymbol{A}x - y\| \tag{4.35}$$

  plotted as a function of the regularization parameter α and which exhibits now a sigmoidal shape (see figure 4.4). This *ad hoc* method takes into account the actual shape of the distribution function and is therefore independent of non linear constraints. The

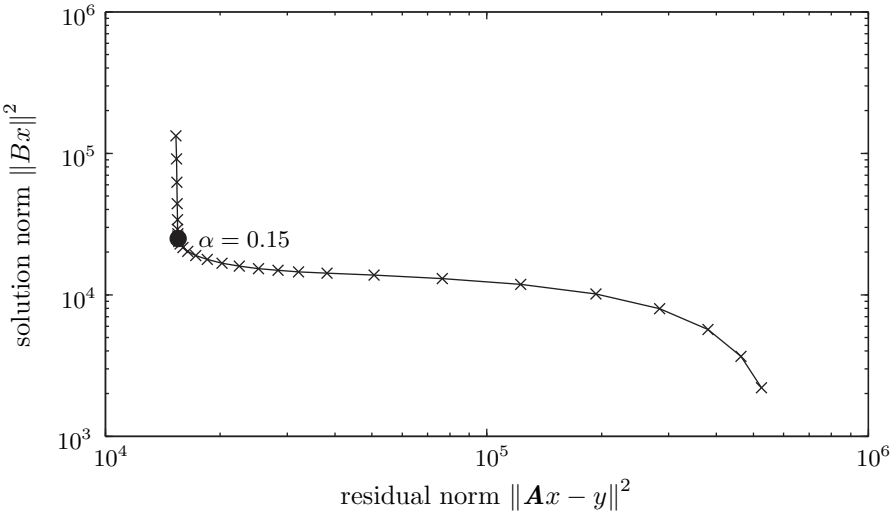

Figure 4.3: L-shaped log-log graph of the norm of the regularized solution $\|B\widehat{x}\|$ versus the corresponding residual norm $\|\boldsymbol{A}\widehat{x} - y\|$ for different values of the regularization parameter α for the T_2 distribution of the FCP1 sample given in figure 5.14. The *optimum* value for α (black dot) lies in the corner of the curve.

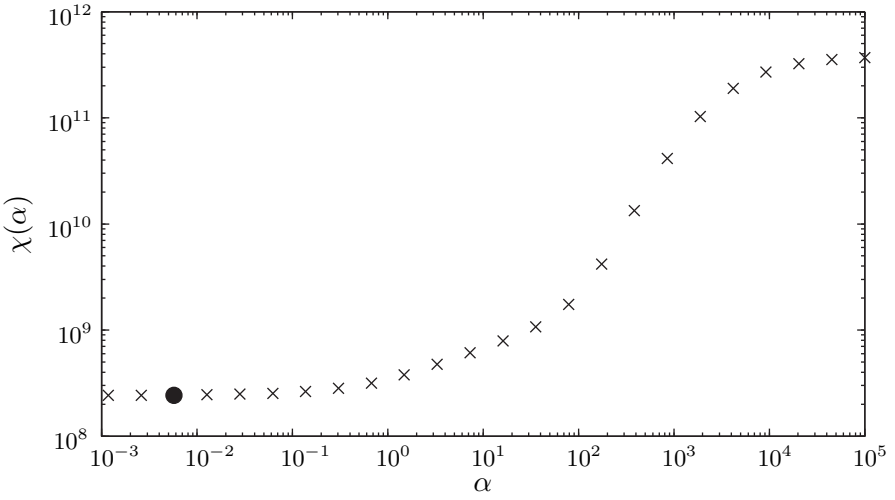

Figure 4.4: S-shaped log-log graph of the fit error in function of the regularization parameter α for the T_2 distribution of the FCP1 sample given in figure 5.14. The *optimal* value for α (black dot) lies at the left base of the S-shaped cure where Eq. 4.36 is satisfied. (TOL=0.01)

disadvantage of this method is that the distribution has to be calculated for a large set of possible values for the regularization parameter.

In the large α limit the curve approaches $\chi^2 \approx \|y\|$. As α is decreased, the fit error χ eventually starts to decrease. The value of α chosen is the smallest value that satisfies

$$\frac{d\,(log\chi)}{d\,(log\alpha)} = \text{TOL} \tag{4.36}$$

where $0 < \mathrm{TOL} < 1$ is a prefixed constant close to zero, so that the resulting value of α will depend on the constant TOL (*tolerance*). At first sight this method just replaces one parameter (α) with another (TOL). Note, however, that this last parameter is data-independent: possible values are clearly bounded, and it can be set to a constant irrespective of the measurement noise level and the actual distribution. A fixed choice of TOL corresponds, for all data sets, to the same degree of compromise between resolving the structure in $\widehat{x}$ (by minimizing $\|\boldsymbol{A}x - y\|^2$) and avoiding instability (by minimizing $\|\boldsymbol{B}x\|^2$).

4.1.7 Solving the minimization problem

Once a value for the regularization parameter is found, Eq. 4.32 can be solved. However, the solution will have some constraints. Negative amplitudes, arising from the oscillating eigenvectors (see figure 4.1(b), are not possible and Eq. 4.24 can therefore be written as:

$$\widehat{x} = \arg\min_{\widehat{x}\geq 0} \left(\|\boldsymbol{A}x - y\|^2 + \alpha \|\boldsymbol{B}x - b\|^2 \right) \tag{4.37}$$

Due to these non-linear constraints it is not possible to solve this equation analytically. Three different approaches are described below:

- The minimization problem can be solved by a nonlinear optimization based on the Nelder-Mead Simplex method (Nelder and Mead [1965]). If n is the dimension of x, a simplex in n-dimensional space is characterized by the $n+1$ distinct vectors that are its vertices. At each step of the search, a new point in or near the current simplex is generated. The function value at the new point is compared with the function's values at the vertices of the simplex and, usually, one of the vertices is replaced by the new point, giving a new simplex. This step is repeated until the diameter of the simplex is less than the specified tolerance.

  The algorithm used in this work is the Matlab function `fminsearch` that uses the simplex search method of Lagarias et al. [1998]. Because the simplex method only requires function evaluations and no derivatives, the method is sometimes not very efficient in terms of the number of function evaluations it requires. Furthermore the dimension of n can become quite large, making this method very time consuming.

- The steepest decent method combined with projections onto convex sets (SDPCS) can also be used to solve the minimization problem (Press et al. [2002]). In the steepest descent method one starts at point $\widehat{x}_0$ and moves as many times as needed in the direction of the "downhill" gradient $-\nabla f(x_i)$. With the gradient of Eq. 4.26 equal to

$$\nabla(\mathcal{A} + \alpha\mathcal{B}) = 2\left(\boldsymbol{A}^T\boldsymbol{A} + \alpha\boldsymbol{B}^T\boldsymbol{B}\right) \cdot \widehat{x}, \tag{4.38}$$

the solution after $k+1$ iterations can then be written as

$$\begin{aligned}\widehat{x}^{(k+1)} &= \widehat{x}^{(k)} - \epsilon\nabla\left(\mathcal{A}+\alpha\mathcal{B}\right)\\ &= \left[1-\epsilon\left(\boldsymbol{A}^T\boldsymbol{A}+\alpha\boldsymbol{B}^T\boldsymbol{B}\right)\right]\cdot\widehat{x}^{(k)}.\end{aligned} \tag{4.39}$$

The non-linear constraints can be implemented in this solution by applying *nonexpansive projection operators* $\mathcal{P}_i$ onto a *convex set*:

- a *convex set* is a set of possible underlying functions for which the point

$$(1-\eta)\widehat{x}_a+\eta\widehat{x}_b \quad \text{with}: 0\leq\eta\leq 1 \tag{4.40}$$

  must be also in the set, when $\widehat{x}_a$ and $\widehat{x}_b$ are elements of that set. The nonnegativity constraint and the zero values outside a certain region are therefore defining a convex set.
- the *nonexpansive projection operators* $\mathcal{P}_i$ onto these two convex sets are then:
  - "setting all negative compounds equal to zero" ($\mathcal{P}_1$)
  - "setting all compounds outside of the region of support equal to zero" ($\mathcal{P}_2$)

When C is the intersection of m convex sets $C_1, C_2, ..., C_m$ then

$$\widehat{x}^{(k+1)} = \left(\mathcal{P}_1\mathcal{P}_2\cdots\mathcal{P}_m\right)\widehat{x}^{(k)} \tag{4.41}$$

will converge to C from all starting points, for $k\rightarrow\infty$. Combining Eqn. 4.39 and 4.41 gives

$$\widehat{x}^{(k+1)} = \left(\mathcal{P}_1\mathcal{P}_2\cdots\mathcal{P}_m\right)\left[1-\epsilon\left(\boldsymbol{A}^T\boldsymbol{A}+\alpha\boldsymbol{B}^T\boldsymbol{B}\right)\right]\cdot\widehat{x}^{(k)} \tag{4.42}$$

This iteration will converge to minimize the quadratic functional 4.32 subject to the desired nonlinear constraints. Because this method makes use of the gradient, it will be significantly faster than the first method.

- Butler et al. [1981] provide an elegant method (BRD method) to solve the constrained minimization problem for the zeroth order regularization given in Eq. 4.27:

$$\widehat{x} = \arg\min_{\widehat{x}\geq 0}\left(\|\boldsymbol{A}x-y\|^2+\alpha\|x\|^2\right) = \arg\min_{\widehat{x}\geq 0} Q \tag{4.43}$$

  Let x_i be the elements of the solution $\widehat{x}$ with i=1,...,n. The necessary conditions for the inequality constrained minimum (the Kuhn-Tucker conditions) are:

$$\nabla Q(x_i) = 0, \quad \text{if } x_i>0, \quad i=1,\ldots,n \tag{4.44}$$

$$\nabla Q(x_i) \geq 0, \quad \text{if } x_i=0, \quad i=1,\ldots,n \tag{4.45}$$

  where ∇ represents the derivative operator. The derivative of Eq. 4.27 is given by

$$\frac{\partial Q}{\partial x_i} = A_i^T(\boldsymbol{A}x-y)+\alpha x_i \tag{4.46}$$

where A_i is the ith column of $\boldsymbol{A}$. From Eq. 4.44 and 4.46, we get

$$\alpha x_i = -A_i^T(\boldsymbol{A}x - y) \quad \text{if } x_i > 0 \tag{4.47}$$

This can be written as

$$x_i = A_i' c \quad \text{if } x_i > 0 \tag{4.48}$$

where

$$c = \frac{\boldsymbol{A}x - y}{-\alpha} \tag{4.49}$$

From Eq. 4.45, 4.46 and 4.48, we get

$$x = \max\left(0, \boldsymbol{A}^T c\right) \tag{4.50}$$

Substituting Eq. 4.50 in 4.49, we have

$$\boldsymbol{A}\left[\max(0, \boldsymbol{A}^T c)\right] - y + \alpha c = 0 \tag{4.51}$$

$$(\boldsymbol{G}(c) + \alpha I)c = y \tag{4.52}$$

where

$$\boldsymbol{G}(c) = \begin{bmatrix} H(A_1^T c) & 0 & \dots & 0 \\ 0 & H(A_1^T c) & \dots & 0 \\ \vdots & \vdots & \ddots & \vdots \\ 0 & 0 & \dots & H(A_n^T c) \end{bmatrix} \tag{4.53}$$

and where $H(\,\cdot\,)$ denotes the Heaviside function. The matrix $\boldsymbol{G}(c)$ is symmetric and semi-positive definite. Butler et al. [1981] showed that the vector c that satisfies Eq. 4.52 can be estimated by minimizing the function

$$\chi(c) = \frac{1}{2} c^T \left[\boldsymbol{G}(c) + \alpha I\right] c - c^T y \tag{4.54}$$

Since the first and second derivative of this expression can be derived,

$$\nabla\chi(c) = (\boldsymbol{G}(c) + \alpha I)c - y \tag{4.55}$$

$$\nabla\nabla\chi(c) = \boldsymbol{G}(c) + \alpha I, \tag{4.56}$$

the optimization for c can be performed using the inverse Newton method:

$$c_{n+1} = c_n - \frac{\boldsymbol{G}(c) + \alpha I}{(\boldsymbol{G}(c) + \alpha I)c - y} \tag{4.57}$$

Substituting Eq. 4.57 in 4.48 gives the estimation for x.
Because this method also makes use of the gradients, the minimum will be found again relatively fast. It will however be slower as the previous method because during the iteration, the inverse of a eventually large matrix $((\boldsymbol{G}(c)+\alpha I)c-y)$ must be calculated.

All three methods are implemented in the data analysis software.

4.1.8 Validation of the regularized solutions

All three regularization methods were tested extensively with simulated data. This was done by generating an FID envelope from a simulated relaxation distribution calculated from one or two lognormal probability density functions with 100 elements each. Using this distribution, the resulting FID envelope was then generated by Eq. 4.4:

$$y = \boldsymbol{A}x + \epsilon, \tag{4.58}$$

where x is the distribution of the relaxation times, $\boldsymbol{A}$ is the kernel (see 4.1.1) and ϵ is a noise vector. Experimental noise was recorded by the Earth's field NMR device and was added to the FID envelope. By adjusting the noise amplitude, a signal to noise ratio comparable to real (accumulated) measurements from a porous system containing about 6 ml of water, was obtained (SNR ≈ 1000).

From this noisy signal the underlying distribution is recalculated by the three different regularization methods and compared with the true distribution. A first guess for the regularization parameter was obtained by Eq. 4.34. A set of 30 possible values for the regularization parameter, logarithmically spread around this value, was generated. The most *appropriate* value among this set was evaluated by S-curve method (Fordham et al. [1995], see section 4.1.6).

Four different cases were considered:

- one broad peak
- one narrow peak
- two distinct peaks
- two overlapping peaks

In the following four figures, the original relaxation time distribution as well as the distributions derived from the noisy FID envelopes are given for the four cases and the three different methods. The FID envelopes themselves are also displayed, together with the difference between the calculated and original FID envelope. Although the difference between the distributions determined by the three regularizing methods are considerable, the FID envelopes are not easily distinctable. This proves the *ill-posed* character of the inversion: a small disturbance in the data (the FID envelope) can lead to huge changes in the underlying distribution, meaning that a large number of solution exists, all compatible with the data within the experimental error.

As can be seen from figure 4.5, all three regularization methods give good results for the distributions with one broad peak. The distribution that is found by the Simplex method is

hardly discernible from the original distribution. The distribution of both the SDPCS and BRD method are showing some small features at the right side of the distribution that are not present in the original distribution. For the narrow peak (figure 4.6) the SDPCS method gives a too broad distribution. The Simplex and the BRD method are giving much better results. In the case of two distinct peaks (figure 4.7), the SDPCS gives again a too broad distributions for the first peak. The other two methods give better results. For two overlapping peaks (figure 4.8) the difference between the original distribution and the solutions found by the three regularization methods are biggest. The general shape of the distribution and the location of both peaks are found by all three methods, but the intersection between both peaks is not well fitted.

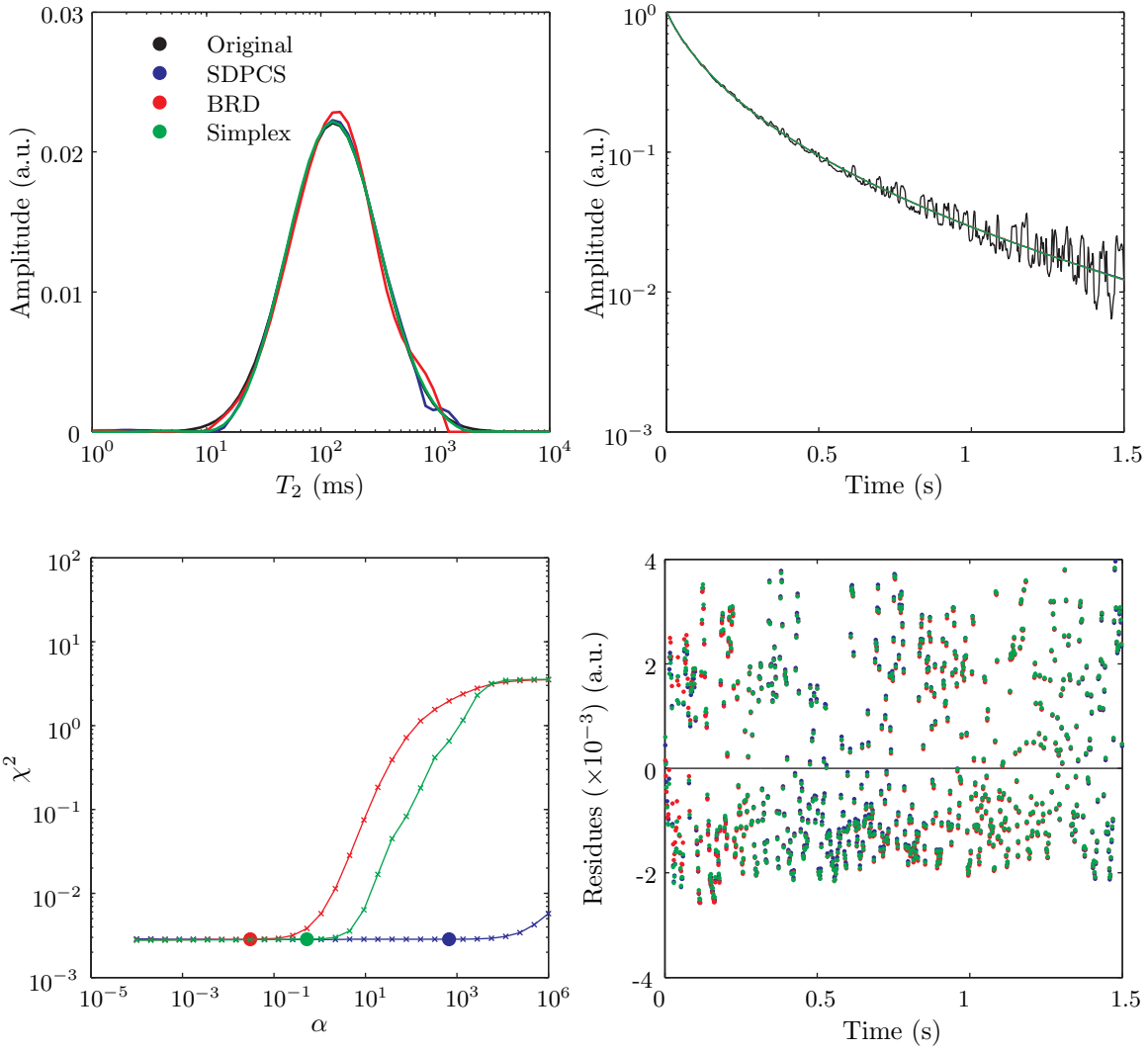

Figure 4.5: *top left:* The original distribution together with the distributions found for the three different regularized inversion methods (SDPCS, BRD and Simplex) for the case of a broad monodisperse distribution. *top right:* The FID envelopes corresponding to the original distribution together with the corresponding envelopes of the three fits. *bottom left:* The S-curves for every method with the chosen α (dot). *bottom right:* The residual values for all data fits.

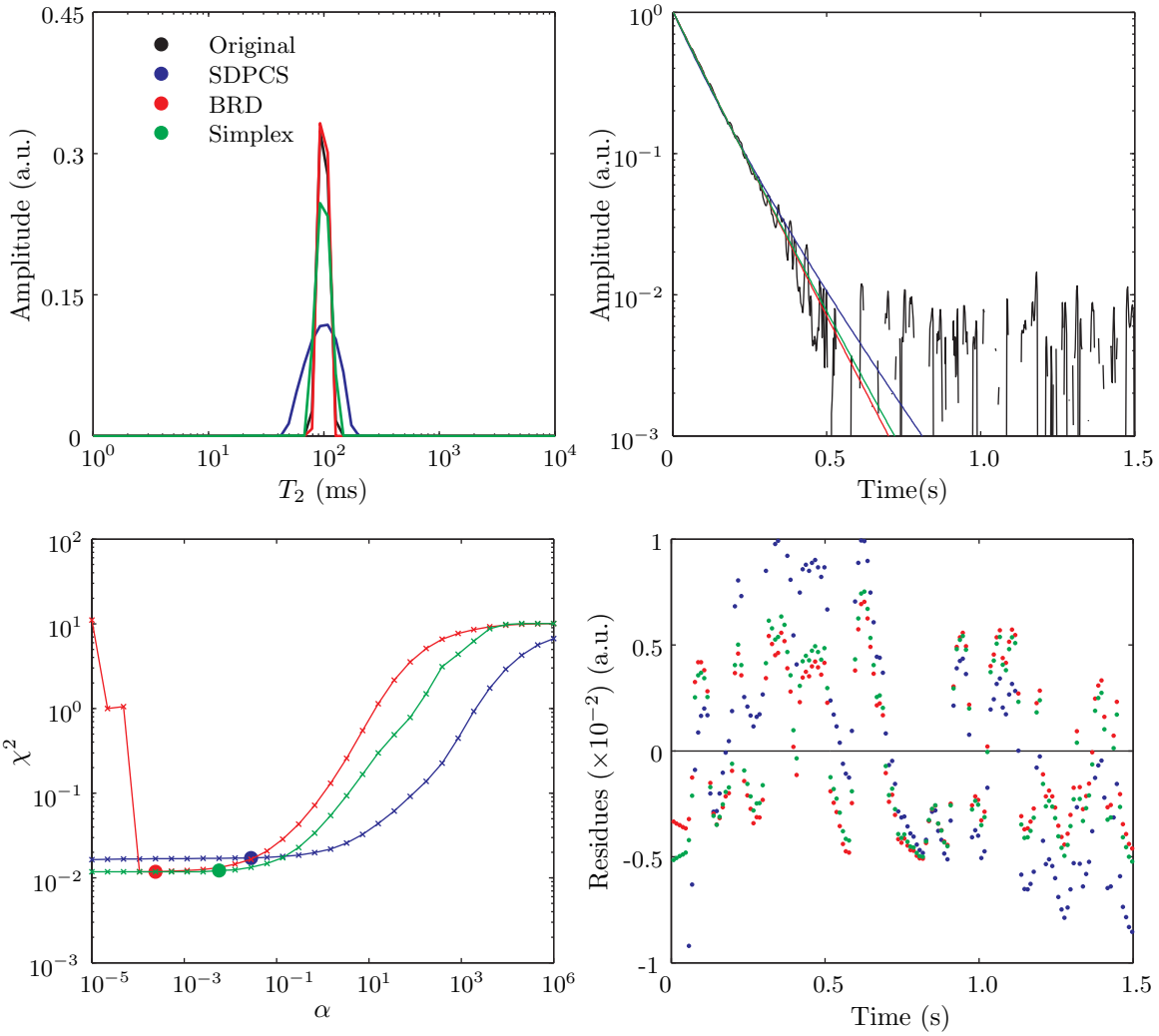

Figure 4.6: *top left:* The original distribution together with the distributions found for the three different regularized inversion methods (SDPCS, BRD and Simplex) for the case of a narrow monodisperse distribution. *top right:* The FID envelopes corresponding to the original distribution together with the corresponding envelopes of the three fits. *bottom left:* The S-curves for every method with the chosen α (dot). *bottom right:* The residual values for all data fits.

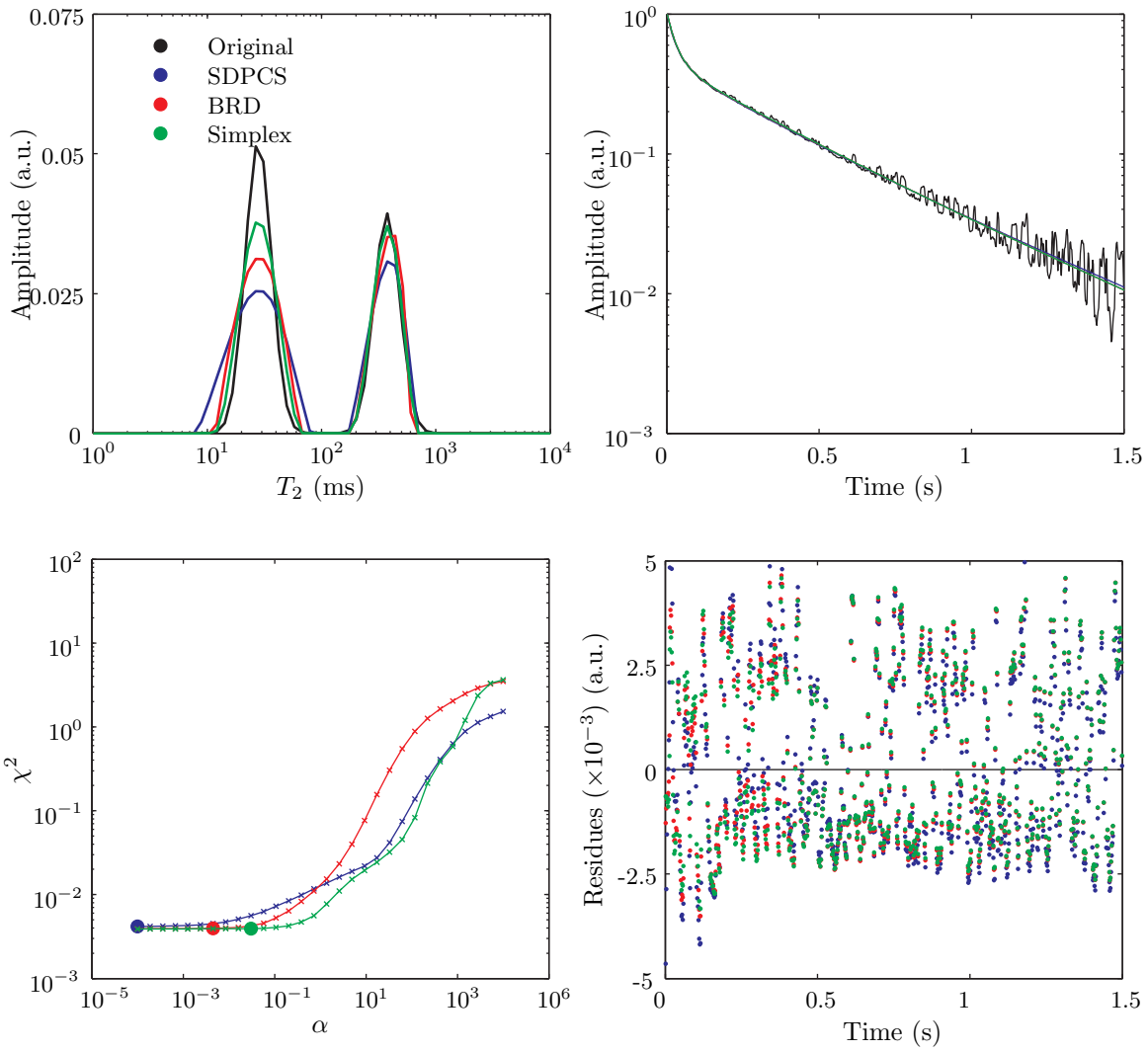

Figure 4.7: *top left:* The original distribution together with the distributions found for the three different regularized inversion methods (SDPCS, BRD and Simplex) for the case of a distribution with two distinct peaks. *top right:* The FID envelopes corresponding to the original distribution together with the corresponding envelopes of the three fits. *bottom left:* The S-curves for every method with the chosen α (dot). *bottom right:* The residual values for all data fits.

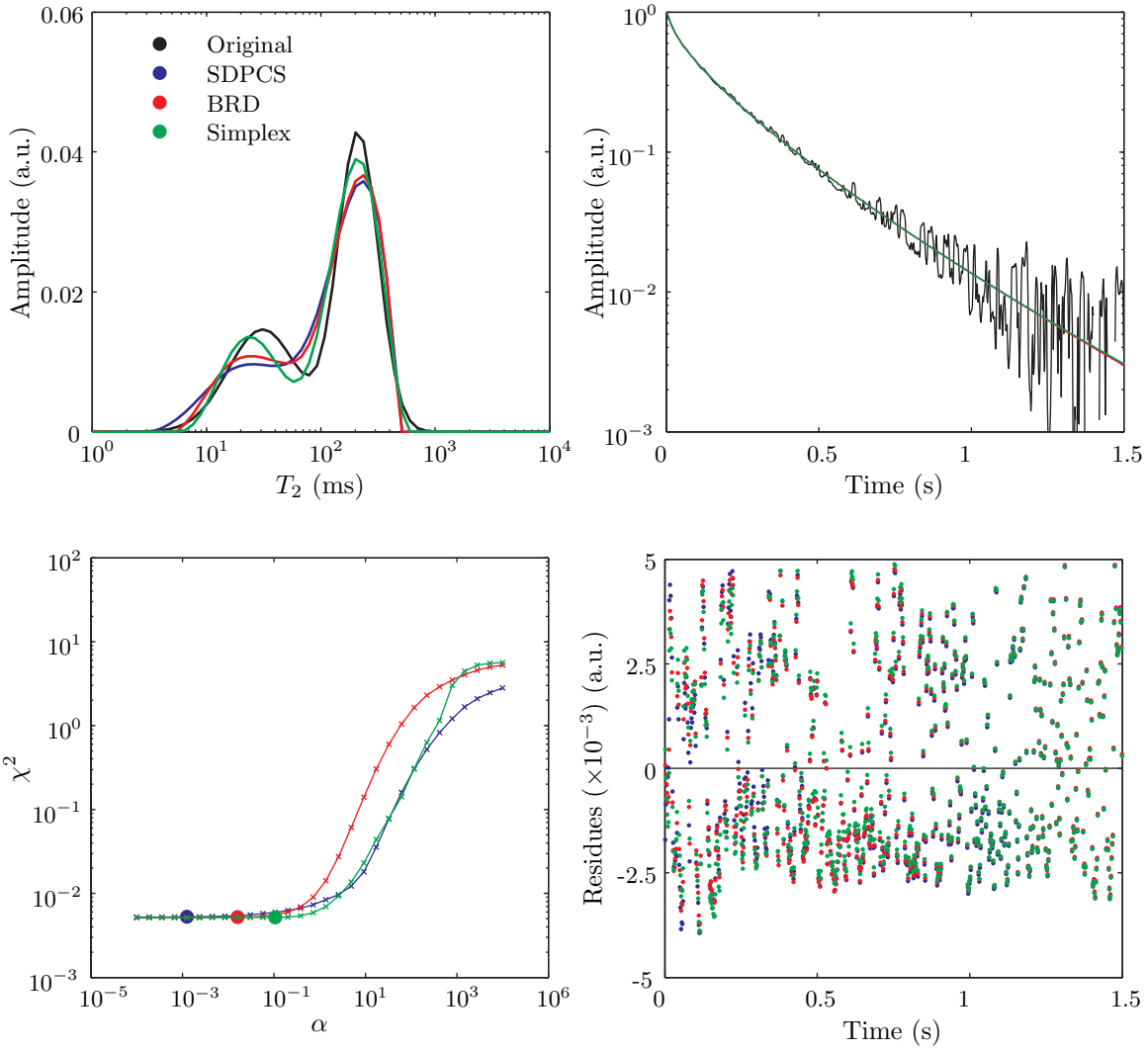

Figure 4.8: *top left:* The original distribution together with the distributions found for the three different regularized inversion methods (SDPCS, BRD and Simplex) for the case of a distribution with two overlapping peaks. *top right:* The FID envelopes corresponding to the original distribution together with the corresponding envelopes of the three fits. *bottom left:* The S-curves for every method with the chosen α (dot). *bottom right:* The residual values for all data fits.

Overall, all three methods are suited to find the general structure of the distributions. The SDPCS method gives too broad distributions for narrow peaks and the Simplex method delivers the best results, followed by the BRD method. Additional to the requirement that the regularization method should find the correct distribution, the computation speed is another important factor that determines the usefulness of the method. The calculation times for the three different methods to derive the four distributions are: 0.6, 2.2 and 56 h for the the

SDPCS, the BRD and the Simplex method respectively. The listed values are the calculation times for the whole set of 30 distributions corresponding with every value of α on a standard PC with a Pentium 4 2.8 GHz processor. As already predicted in the description of the method, the Simplex method is very time consuming and therefore not suitable for routine analysis. The steepest decent method and the BRD method require much less time due to the use of derivatives. Because the latter method was found to give the most stable results, this method was chosen to obtain the relaxation time distributions in this work.

4.1.9 Particular solutions

In the previous sections the general solution for the inversion problem $\boldsymbol{A}x = y + \epsilon$ is discussed. With the techniques described in section 4.1.7 the underlying distribution of the relaxation times responsible for the shape of the detected signal can be found. However, some systems will not have a continuous distribution of relaxation times but are characterized by just one or two relaxation time constants. In such cases the whole formulation of the inversion described above can be replaced by a simple least square fit with one or more time constants. By using this method, it is possible to derive the parameters describing the non-exponential processes as mentioned in section 4.1.1 and derive the exact form of y'.

The theoretical FID signal of simple homogeneous substances such as water is mono-exponential: the signal can be fitted with a model with one relaxation time constant and a corresponding amplitude. Contrary to the inversion technique where the relaxation times are pre-determined and the corresponding distribution function of the amplitudes has to be derived, in this case, the value for the relaxation time constant has to be fitted by a least squares procedure. Once the optimal estimated values for the relaxation time constant is found, the corresponding amplitude (leading to the least squares solution) can be analytically derived. This fully ranked over-determined system will be *well posed* and can be solved by the singular value decomposition. The same procedure can be followed for systems with two or three discrete values of T_2 with the experimentally found limitation that the difference between the relaxation times must be large enough (at least a factor of three) otherwise this procedure will not be able to distinguish between the components which will result in an intermediate relaxation time. The least square fit has experimentally found to be not feasible anymore for more then three components because with increasing number of components, the system will get increasingly ill-posed and no stable solution will be reached without extra *a priori* knowledge (regularization).

This procedure can also be used as an approximation for systems with a continuous distribution of relaxation times. Especially when the distribution has narrow peaks, a least squares fit with discrete time constants corresponding to the peak averages of the distribution gives good approximations.

As already explained in section 4.1.1, the shape of the recorded signal also depends on the response function of the device and the rest inhomogeneity. Taking into account these experimental conditions, the function that models the envelope of the FID signal looks as follows:

$$\left(1 - e^{-\frac{t-t_0}{\tau}}\right) \cdot e^{-DB \cdot t^2} \cdot \sum_{k=1}^{z} A_k \cdot e^{-\frac{t}{T_{2k}}} = G(t_o, \tau, DB, t) \cdot \sum_{k=1}^{z} A_k \cdot e^{-\frac{t}{T_{2k}}} \tag{4.59}$$

To find the values of the unknown parameters, we have to minimize the following function (with the dimensions of y and t equal to n):

$$\sum_{i=1}^{n} \left[y_i - G(t_o, \tau, DB, t) \cdot \sum_{k=1}^{z} A_k \cdot e^{-\frac{t_i}{T_{2k}}} \right]^2 \tag{4.60}$$

Additional to the relaxation, three other parameters have to be fitted: t_0, τ and DB. These three parameters have also to be determined in the case of a continuous distribution (see section 4.1.1). Therefore, before every measurement of a sample with an expected continuous distribution, a sample is measured with only one relaxation time (usually water). From this measurement, the parameters t_0, τ and DB are determined and considered as constants in the minimization of the continuous distribution. The least squares minimization of Eq. 4.60 is done by a self written Matlab program based on the MINUIT routine developed at CERN by James and Roos [1975]. MINUIT is a physics analysis tool for multidimensional nonlinear function minimization in which the user can choose between different minimization algorithms. The minimization in this work is done by a sequence of two algorithms: Migrad and Simplex. Both Migrad and Simplex locate function minima by finding a minimum of the chi-squared fit between the experimental data and the selected model function. Contrary to Simplex (see section 4.1.7), Migrad calculates the differentials first and follows the slope to a minimum and will be therefore more efficient. If Migrad fails, e.g. due to a inaccurate determination of the first derivatives, the routine reverts to Simplex and then calls Migrad again. In this way a stable solutions is found for almost all cases.

The fitting procedure is done by minimizing expression 4.60 for a limited time interval of the detected signal. Because of the dead time and the relatively slow building up of the signal (see section 3.4.3), the first 15 ms are usually excluded from the fit. The initial values of the fit parameters have to be set by the user. Also the upper and lower limits of the individual parameters and the step size can be set (*constrained non-linear fit*). Variables can also be fixed after which MINUIT considers them as constants and not as variables anymore. When MINUIT is running, the parameters are varied iteratively until the result of Eq. 4.60 is minimized. The quality of the fit is analyzed and validated by taking the following criteria into account:

- Convergence of the minimization. Due to the use of Simplex when Migrad fails this will almost always be the case.

- Solutions with unrealistic values for parameters are discarded. Examples for unrealistic values are relaxation times in porous systems that are larger than bulk water relaxation times or amplitudes corresponding to a volume larger than the sample volume.
- The solution must be close to the solution of similar samples.
- The residues (differences between the experimental data and the model function) should be randomly spread around zero without any trend.

Especially the last criterion proved to be very helpful in analyzing the fits. Also for deciding about whether a signal has one, two or three components, these criteria were taken into account. The stability of the fitting routine has been tested extensively by self generated data.

An example of an T_2 analysis is given in figure 4.9. The blue curve represents the accumulated FID envelope (50 accumulations) of 22 ml of 1.56 mmol/L $CuSO_4$ (see section 3.4.3.1). The red curve represents the model described in Eq. 4.59. The values of the parameters are: $t_0 = 10.90 \pm 0.04$ ms, $\tau = 9.06 \pm 0.05$ ms, $DB = (3.52 \pm 0.1) \cdot 10^{-7}$, $A = 21.4 \pm 0.1$ μV and $T_2 = 194 \pm 4$ ms. The green curve represents the decay for the case where there is no delayed signal build up or inhomogeneity effect and where the FID envelope can be described by the transversal relaxation time only. The black line illustrates the influence of the inhomogeneity. It shows the part of the decay that is caused by the inhomogeneity of the measurement field. The graph at the bottom shows the distribution of the residues. The symmetric distribution around zero suggests that the experimental data can be modeled well with Eq. 4.59.

4.2 T_1 analysis

Additional to T_2 measurements, the Earth's field NMR device is also able to measure the longitudinal relaxation time T_1. For a T_1 measurement the FID envelope is measured for different values of the polarization time t_p. The dependence of the initial amplitude of those FID envelopes with varying t_p will then describe the T_1 processes (see figure 3.7). Because the longitudinal time constant describes the time dependence of the magnetization during the polarisation, T_1 can be measured at different field strengths by changing the polarization current. Depending on the magnitude of the polarization current the measurement is done in the *direct mode* or the *relaxometry mode* (see figure 3.7).

A T_1 measurement is much more time consuming than a T_2 measurement since for every data point (the initial amplitude at every polarization time t_p) an FID has to be measured. To derive the initial amplitudes for different values of t_p, two different approaches can be applied. In the first approach the integral from a part of the FID envelope is taken as a measure of the

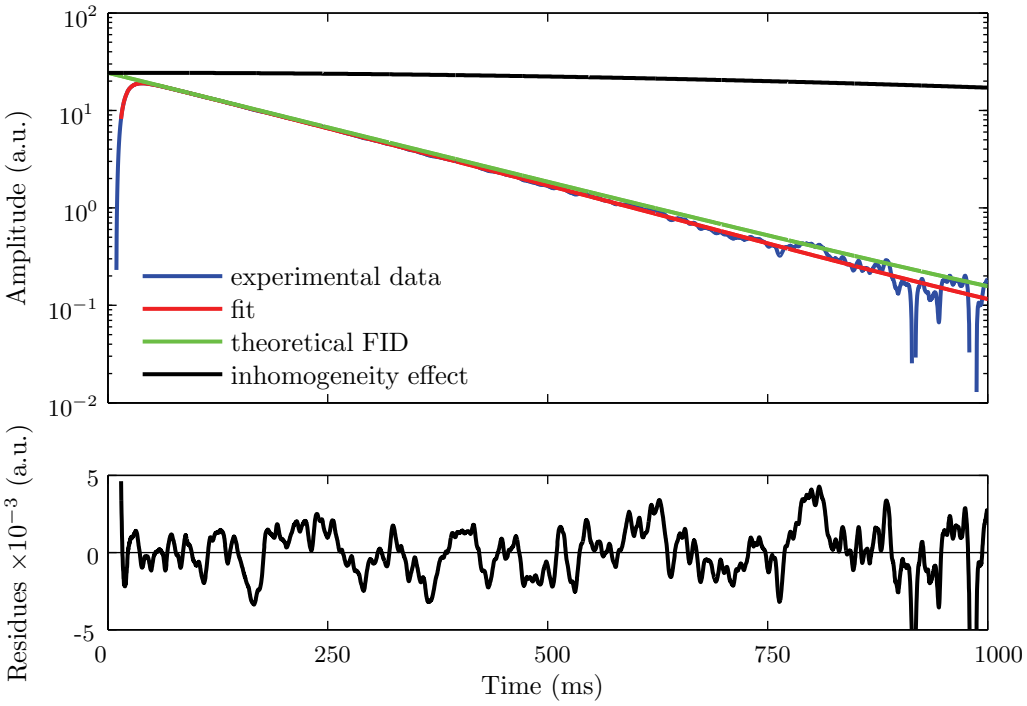

Figure 4.9: Experimental measured FID envelope (blue), the fit using Eq. 4.59 (red), the theoretical FID (green), and the influence of the inhomogeneity (black) together with the residues for the accumulated signal of 22 ml of 1.56 mmol/L $CuSO_4$ (50 accumulations).

initial amplitude. Although this method is still frequently used (e.g. in MRI applications), it is only valid for samples with one time constant. When a sample has multiple time constants, the change of the integral value with t_p will strongly depend on the lower and upper bounds of the integral. In the second method, a T_2 analysis of the sample has to be performed first. From this analysis the values for $T_{2,j}$, DB, τ, t_0 are derived and set as constants in the model describing the FID envelopes for different values of t_p. The only variables are then the weighting factors (initial amplitudes), which can be calculated analytically. Once the time dependence of the initial amplitudes with polarization time has been computed, the further signal analysis is similar to a T_2 analysis. One can again distinguish between a continuous analysis resulting in a relaxation time distribution and in a discrete analysis with few discrete components. Since the longitudinal processes are not influenced by the field inhomogeneity or the imperfect response of the device, the data vector does not have to be transformed as is the case for T_2 measurements (see Eq. 4.5), leading to a less complicated signal analysis.

For the *direct mode* the initial amplitudes in function of the polarization time will follow (see

figure 3.7):

$$M = \sum_{j=1}^{m} a_j \cdot (1 - e^{-\frac{t_p}{T_{1,j}}}), \tag{4.61}$$

and for the *relaxometry mode*:

$$M = \sum_{j=1}^{m} a_j \cdot e^{-\frac{t_p}{T_{1,j}}} + C_0. \tag{4.62}$$

4.3 Reproducibility

The reproducibility of the data analysis (and the NMR device) has been tested by repetitive measurements of the transversal and longitudinal relaxation time of water doped with $CuSO_4$ (7.8 mmol/L). In figure 4.10 the T_2 values (measured at 2050 Hz), and the T_1 values measured at a frequency of 3 kHz and 3 MHz are given for 30 repetitive measurements homogeneously spread over a time period of 5 days. The T_2 values are slightly smaller than the T_1 values. The difference between the longitudinal relaxation times at 3 kHz and 3 MHz is small, indicating a small dependence of T_1 of the Larmor frequency. All relaxation times are quite constant with a standard deviation at around 1 ms (0.99, 1.29 and 1.09 ms for T_2, T_1 at 3 kHz and T_1 at 3 MHz, respectively), proving the very good reproducibility of the measurement data and the data analysis. At the fifth last measurement there seems to be a small but systematic deviation to higher values. This could be due to small temperature deviations.

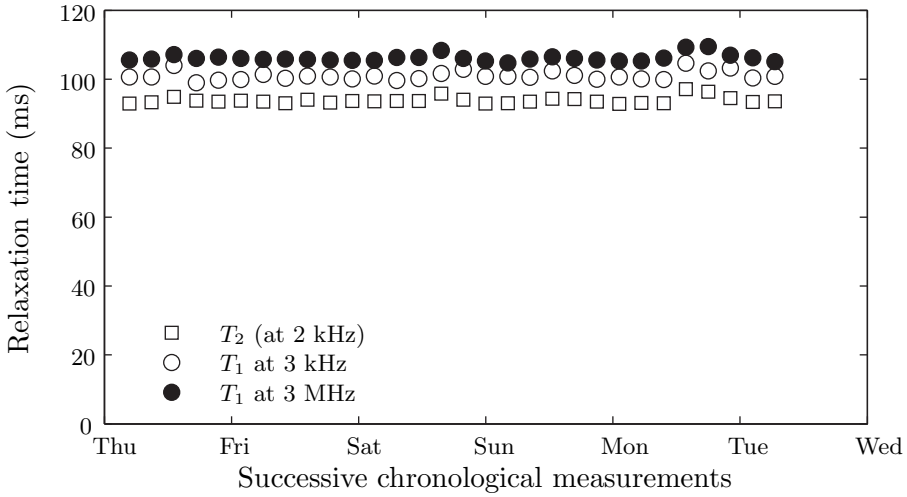

Figure 4.10: 30 successive chronological measurements of T_2 and T_1 at 3 kHz and 3 MHz of a solution of 7.8 mmol $CuSO_4$.

Chapter 5

Results and discussion

5.1 Determination of the water content

5.1.1 In-vitro

Since the magnitude of the detected precessing magnetization vector depends on the amount of spins present in the sample, NMR relaxometry can be used to determine the spin density in a non-invasive way. In this work, the detected signal usually originates from water protons, so that the signal amplitude is proportional to the water content of the sample. An absolute measurement of the water content is possible after calibration with known water volumes.

The signal amplitudes (in μV) in function of the water content (in ml) for pure water are given in figure 5.1. The initial amplitude was derived by fitting the FID envelope to a model with one time constant (see section 4.1.9). Since the signal amplitude increases with the water content, the amount of accumulations was made dependent on the water content, in order to get a comparable signal to noise ratio for every sample:

$$N_{i+1} = (\frac{V_i}{V_{i+1}})^2 \cdot N_i \tag{5.1}$$

with N the amount of accumulations and V the water content.

As can be seen from figure 5.1, there exists an almost perfectly linear relationship between the signal amplitude (in μV) and the water content (in ml):

$$S = (0.91 \pm 0.01)\frac{\mu\text{V}}{\text{ml}} \cdot V_w \quad \text{or} \quad V_w = (1.10 \pm 0.01)\frac{\text{ml}}{\mu\text{V}} \cdot \text{S} \tag{5.2}$$

Because the lateral position of the water in the coil changes with the water content (the first milliliter of water is located closer to the coil windings as the second milliliter), the linear relationship between the signal amplitude and the water content demonstrates that the

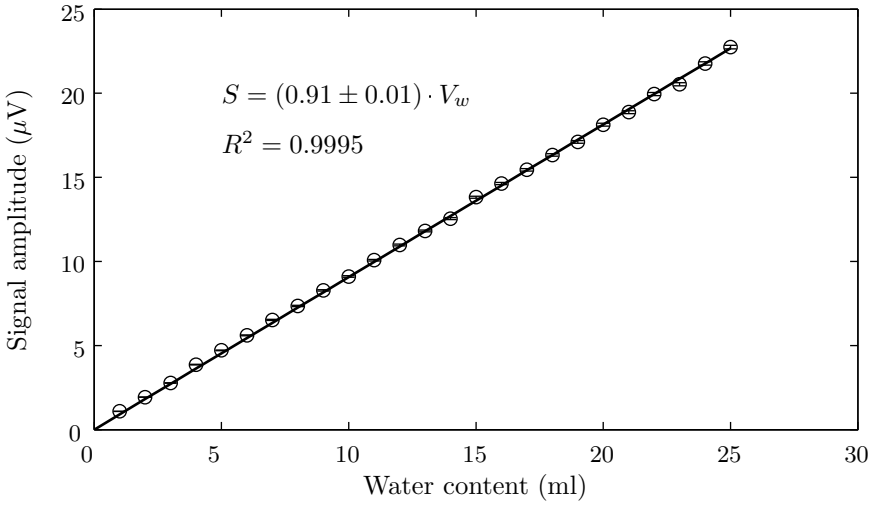

Figure 5.1: The measured signal amplitude for different volumes of bulk water.

sensitivity of the coil is independent of the lateral position of the sample and will only depend on the axial position as already shown in figure 3.10.

In a next experiment the normalized (see Eq. 3.32) initial amplitudes of water confined in the pores of cleaned sand (Sea sand p.a., Applichem) were determined. Ten different volumes of deionized water (1 to 10 ml) were added to about 60 g of the the dried soil sample. 10 ml of water corresponds to 100 % saturation. After a waiting time of several days (to assure an equilibrium state) the FID envelopes of the water confined in the pores of the sand sample were measured. The relaxation times are still long enough ($T_2 > 40$ ms) for the precise determination of the initial amplitudes. The amount of accumulations was made again dependent on the water content to obtain a similar signal to noise ratio for every sample (see Eq. 5.1).

Since the water in the sand is located in pores with different sizes, the FID envelope is not expected to be mono-exponential. This can be clearly seen in figure 5.2 where the relaxation time distributions are plotted for different amounts of water in the sand. Because the relaxation times of porous systems can vary over a wide range, the distributions are usually plotted on a semilogarithmic scale. However, the particular values of the amplitudes must be considered as discrete values. This means that, although a logarithmic plot is used, the *bins* will all have the same width and the integral (the total amount of the water) is reduced to a simple summation over the logarithmically spaced amplitudes.

In figure 5.3 the sum of all amplitudes of the relaxation time distribution are plotted in function of the water content. There is again a very good linear relationship between amplitude and water content:

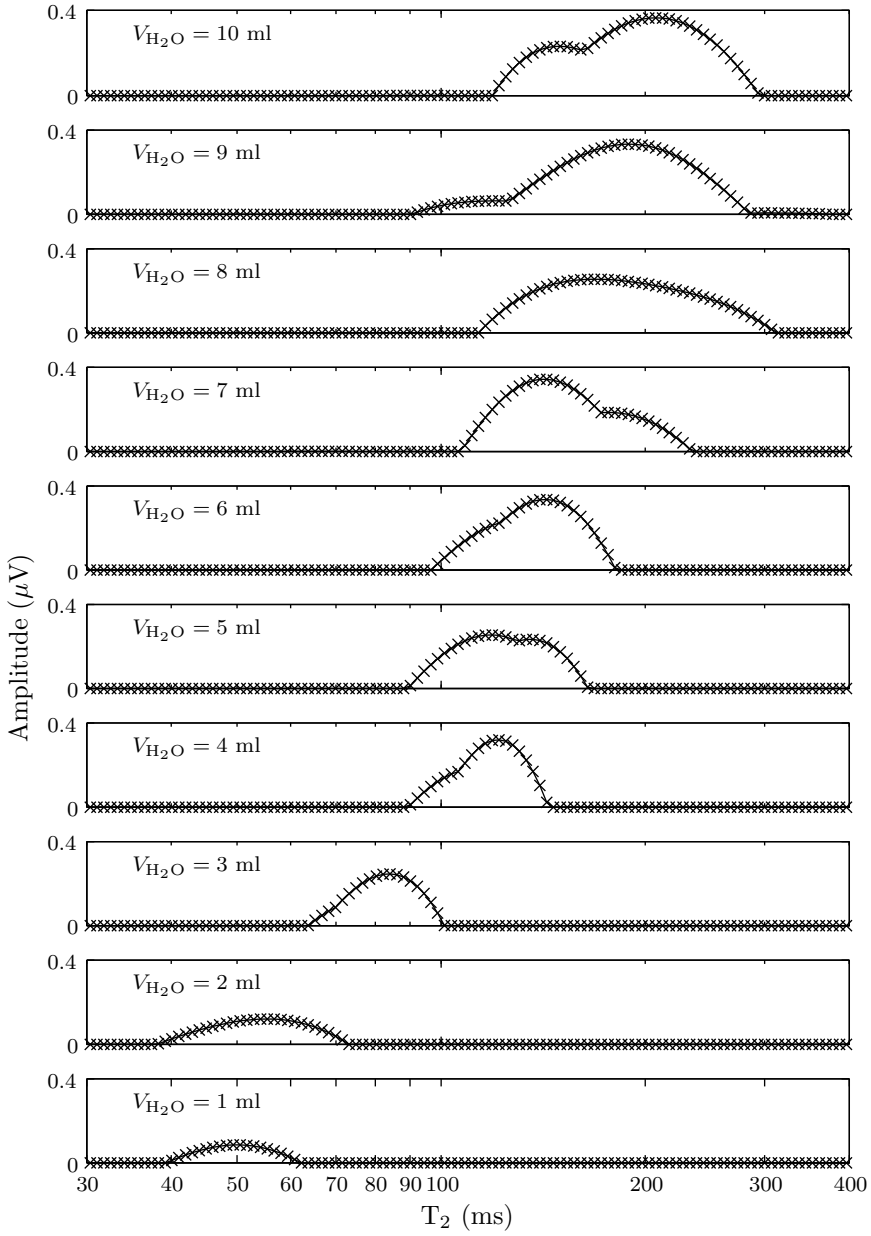

Figure 5.2: Transversal relaxation time distributions of clean sand (Sea sand p.a., Applichem) filled with different amounts of deionised water

$$S = (0.88 \pm 0.01)\frac{\mu\mathrm{V}}{\mathrm{ml}} \cdot V_w \quad \text{or} \quad V_w = (1.14 \pm 0.02)\frac{\mathrm{ml}}{\mu\mathrm{V}} \cdot \mathrm{S} \tag{5.3}$$

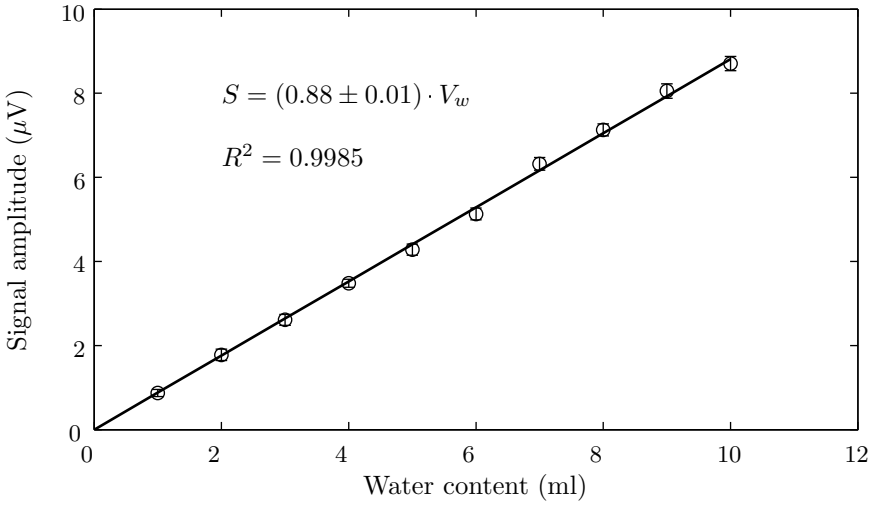

Figure 5.3: The measured signal amplitude for different volumes of water confined in cleaned sea sand analyzed multiexponentially

The value for the calibration factor between water content and signal amplitude for the water confined in the pores of the clean sand is not significant different than for bulk water. Although the relaxation times of the water confined in the cleaned sand have a relatively broad distribution (see figure 5.2), the FID envelopes can be fitted in a first approximation by a mono-exponential fit where the time constant corresponds with the value at the center of the relaxation time distribution. Although a multi-exponential fit is physically more meaningful, a mono-exponential fit is easier to perform (see chapter 4) and also gives useful results. In figure 5.4 the initial amplitudes found by a mono-exponential fit are plotted in function of the water content. Again a perfectly linear relationship between the signal amplitude and the water content is found:

$$S = (0.86 \pm 0.01)\frac{\mu\mathrm{V}}{\mathrm{ml}} \cdot V_w \quad \text{or} \quad V_w = (1.16 \pm 0.01)\frac{\mathrm{ml}}{\mu\mathrm{V}} \cdot \mathrm{S} \tag{5.4}$$

The value for the calibration factor to convert microvolts into milliliter of water is for both cases (multi-exponential and mono-exponential analysis) the same within the experimental error (see Eq. 5.3 and 5.4). This means that in cases where one is only interested in the amplitude, without wanting to have information about the relaxation times, it is sufficient to use a straight forward mono-exponential analysis as long as the relaxation time distribution does not have multiple discrete peaks. In the latter case, a multi-exponential analysis is the only way in finding the right amplitude.

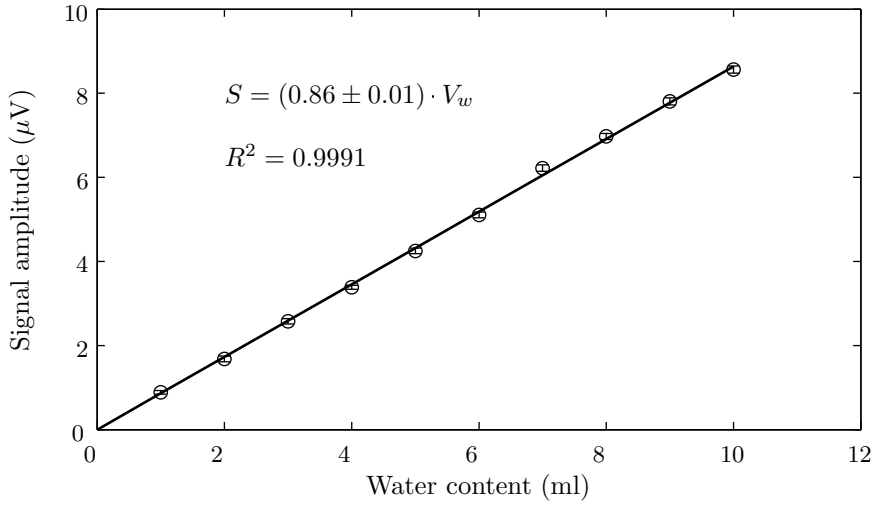

Figure 5.4: The measured signal amplitude for different volumes of water confined in cleaned sea sand analyzed monoexponentially

5.1.2 In-situ

In the previous section it was shown that the Earth's field NMR device can be used to determine the water content of different kinds of samples. It is however necessary to put the sample into a sample holder that fits into the probe head. The *in-situ* probe head has the advantage that the water content of a sample can be measured independent of its dimensions. The only requirements are:

- The relaxation times must be long enough so that the signal can be detected ($T_2 >$ 10 ms).
- The amount of water must be large enough to detect ($> 10\%$).
- One should be able to put the sample close to the coil surface since the sensitivity decreases rapidly with distance (see figure 3.18).
- The water must be homogeneously distributed in the sample. Since water close to the surface will lead to higher signals as water far away from the coil surface, the sensitivity will vary with depth (see figure 3.18) when the water is inhomogeneously distributed.
- The direction of the Earth's magnetic field must be different from the coil axis (see figure 3.20).

When these requirements are fulfilled, the water content of the sample can be derived in a completely non-invasive way. However, an absolute determination of the water content is

only possible after calibration with a sample of the same dimensions and with known water content. Because of those difficulties, the in-situ probe head has only been used to determine the relative water content (e.g. degree of saturation in %).

A comparison between saturation determined gravimetrically and by in-situ Earth's field NMR is given in figure 5.5. A sand layer of about 1 cm thickness was saturated with water. The amount of water added to the dry soil was determined gravimetrically as well as with the Earth's field NMR device. The wet sand was then dried by evaporation and the water content was regularly determined by the two methods and expressed as a function of the water content at saturation.

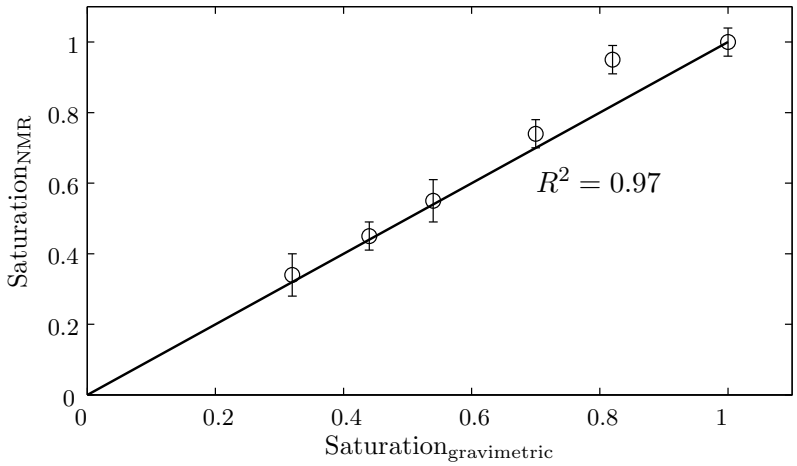

Figure 5.5: Correlation between the saturation determination of a 1 cm thick layer of sand by gravimetry and in-situ Earth's field NMR (100 accumulations)

Although large volumes can be measured, the data quality will be much lower than for the in-vitro probe head, since the in-situ probe head has no shielding or shimming and the geometry is not optimal (the sensitive region does not correspond with the region with the highest magnetic induction (coil axis), but is located outside the coil). The results displayed in figure 5.5 nevertheless show that despite the poor data quality of a single measurement, good results can be obtained by the in-situ probe head.

5.1.3 Temporal variations of the water content

From the previous sections it has become clear that the Earth's field NMR device is capable of measuring the water content of several kinds of systems accurately and in a non-invasive way. Due to the accessibility of the sample (there is no dewar around the sample) and because the sample is temperated with an adjustable air flow, all kinds of drying experiments are possible where the water content of a sample is continuously monitored.

In order to characterize porous systems and better understand the physical properties, the drying rates and drying kinetics of porous systems are frequently studied in the literature (e.g. Laurindo and Prat [1998], Le Bray and Prat [1999], Pel and Landman [2004]). The temporal variation of the water content of five different porous samples was determined by the Earth's field NMR device during a drying process with an air flow of about 1 L/s at 20°C. The porous system used for this experiment consisted of the VitraPOR glass filter discs (ROBU Glasfiltergeräte GmbH, Germany). Each filter disc had a diameter of 25 mm and a height between 2.4 and 3.2 mm. The pore characteristics of the glass filters are given in table 5.1. The pore sizes provided by the manufacturer are based on mercury intrusion porosimetry. The median pore sizes are typical for many building materials such as natural stone and brick. However, in contrast to such materials, the pore size distribution of the glass filters is very narrow, which make them well suited for an investigation of pore size influences (Linnow et al. [2007]).

To perform the drying experiment, six filter plates were saturated with water, stacked together and sealed with Parafilm^{TM} where the top and the bottom of the stack was left open. The sample was placed in the measuring coil and blown with temperated air (20°C). The signal amplitude was continuously measured (about 5 FID measurements per minute) and 10 or 50 FID envelopes were accumulated to improve the S/R ratio. The signal amplitudes were converted to water content by the use of Eq. 5.3 and plotted in figure 5.6.

Table 5.1: Pore sizes of the VitraPOR glass filters

Porosity	Nominal pore size (μm)
1	100 - 160
C	40 - 60
3	16 - 40
4	10 - 16
F	4 - 5.5

Although a complete analysis of the drying behavior of porous systems falls out of the scope of this work, a short qualitative analysis is given below. For the two samples with the largest pores (VitraPOR 1 and C), the saturation decreases roughly linearly with time from maximum moisture until zero moisture content. The saturation level of the other samples also seems to decrease linearly first, but with decreasing water content, the drying rate also starts to decrease and reaches very small values when the sample is almost completely dry. On first sight the saturation level between the constant and the decreasing drying rate seems to be at around 35 %. However, a carefull analysis shows that already at a level of about 60 % the drying rate starts to drop. Moreover the saturation value where the drying rate starts to drop

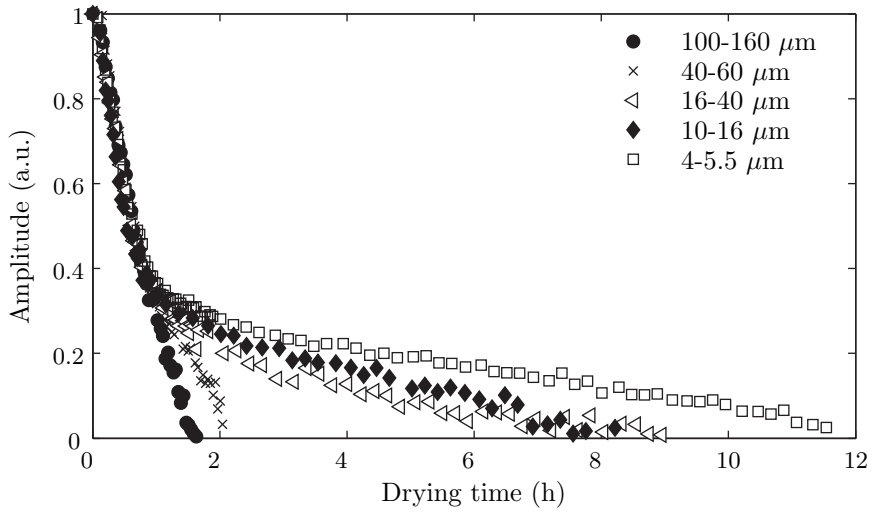

Figure 5.6: The saturation level in function of time for four different VitraPOR filter glasses during a drying experiment with an air flow of 1 L/s at 20°

down seems to depend on the pore size. This can be clearly seen in figure 5.7 where the drying rates are displayed in function of the saturation degree for the three samples with the smallest pore sizes. The drying rates were determined from the differences between consecutive data points.

At the right of the vertical line, the drying rate is constant. This *constant rate period (CRP)* extends over a fairly wide range of the moisture content down to a so-called *critical moisture content*. During the constant rate period the mass transport is governed by capillary flow through complete or partial filled pores. The position of the critical moisture content depends on the pore size: the smaller the pore size, the longer the constant rate period. Beyond this point the drying rate decreases; this is the *falling rate period (FRP)* where the mass transport is governed by evaporation through dry pores. The steepness of the drying rate drop depends on the pore size, since smaller pores lead to a faster drop of the drying rate. The *receding front period (RFP)* begins after the liquid cluster loses contact with the open side of the pore network and is characterized by the receding of the drying front. This particular drying behavior of porous materials has also been described in the literature (e.g. Yiotis et al. [2006], Schlunder [2004], Metzger and Tsotsas [2005]).

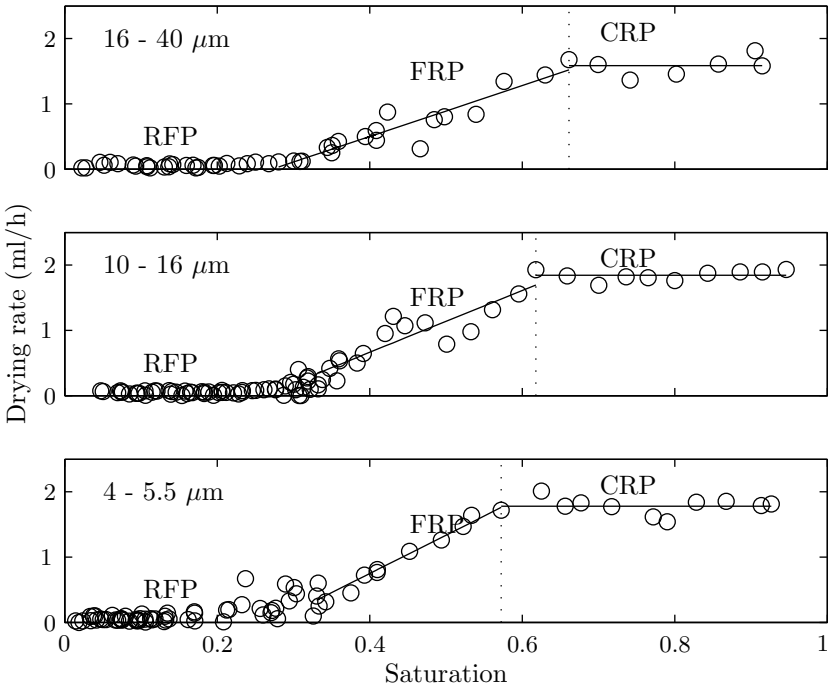

Figure 5.7: The drying rates in function of the moisture content for three different VitraPOR filter glasses during a drying experiment with an air flow of 1 L/s at 20°. The vertical dotted line represents the *critical moisture content* that separates the *constant rate period* (CRP) from the *falling rate period (FRP)*. At low water contents the drying rate is characterized by a *receding front period (RFP)*.

5.2 Relaxation in porous systems

5.2.1 Transversal relaxation

In the previous section it was shown that the amplitude of the FID envelope can be used to derive the water content in the sample. Next to the water content information it is also possible to obtain some information about the *environment* of the water by analyzing the relaxation times. In the literature different models are described that relate the relaxation times for water confined in porous systems to the pore sizes of the sample (see section 2.2). In this chapter the relaxation times of different porous systems will be used to derive the pore size distribution.

The model that will be used to relate the relaxation time to the pore size is the *fast diffusion* regime of the general model of Brownstein and Tarr [1979] (see Eq. 2.36) for $T = T_{1,2}$:

$$\frac{1}{T} = \frac{1}{T_{\text{bulk}}} + \frac{1}{T_{\text{surface}}} = \frac{1}{T_{\text{bulk}}} + \rho\frac{S}{V} \tag{5.5}$$

This equation can also be written as

$$\frac{1}{T} = \frac{1}{T_{\text{bulk}}} + \frac{\alpha\rho}{r} \tag{5.6}$$

with ρ the relaxivity parameter that depends on the surface characteristics of the matrix, α a geometry factor that is equal to 2 for cylindrical pores and 3 for spherical pores, and r the pore radius.

5.2.1.1 Evidence for the fast diffusion limit

Evidence that the *fast diffusion* regime is valid for the clean sand sample can be obtained from figure 5.2. Due to capillary forces the water in the sand will fill the small pores first and then gradually fill the larger pores. Low filling factors correspond therefore to small pores and the largest pores will not be completely filled until the saturation level is reached. A comparison between the distributions of the samples with 4 to 10 ml of water shows that the short relaxation times are only affected moderately whilst components with long relaxation times gradually appear with increasing water content. Due to the capillary forces, this dependence of the relaxation time on the water content corresponds with a dependence on the pore size, as predicted by the fast diffusion limit.

During the first three stages (1 - 3 ml) the relaxation time distributions have components that do not show up in the higher filling levels. This is probably due to the fact that at those filling stages, the small pores are not completely filled and water acts like a film on the surface of the small pores. The thinner the film, the larger the surface to volume ratio and the smaller the relaxation times will be (see Eq. 5.5).

Further evidence in support of the fast diffusion limit hypothesis comes from measurements of the temperature dependence. If NMR relaxation were in the diffusion-limited regime, the relaxation time would depend on the diffusion coefficient of the pore fluid (see section 2.2.2), which is very temperature dependent. To investigate possible temperature influences the relaxation time distribution of 10 ml H_2O in cleaned sand was measured at six different temperatures ($0\pm1, 5\pm1, 20\pm1, 40\pm1, 60\pm3, 80\pm5^\circ$C). These temperatures were obtained by changing the temperature of the pressured air (by the use of a thermostat and heat exchanger, see section 3.4.1.5) flowing through the thin slit between the sample and the measuring coil. To assure that the sample has reached the temperature of the circumfluent air, a waiting time of about half an hour was built in after every temperature increase.

As can be seen from figure 5.8 the position of the peak maximum of the relaxation time distribution is similar for all three temperatures. The values for the relaxation time, derived by a mono-exponential fit and corresponding to the center of the distributions, are given in table 5.2. No significant temperature effect is found. However, the magnitude of the NMR

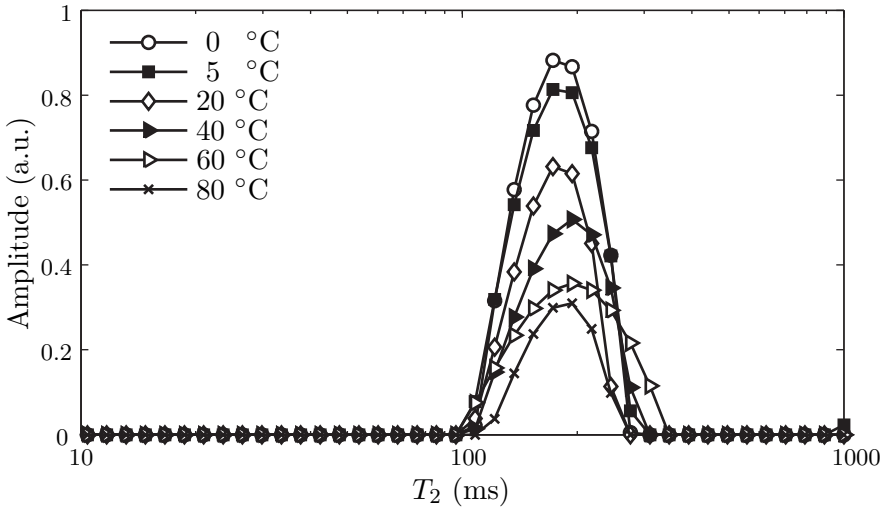

Figure 5.8: The transversal relaxation time distribution for 10 ml of water in cleaned sand at six different temperatures

signal decreases with increasing temperature. This is in accordance with the Curie law (Eq. 2.13):

$$M = N \cdot \frac{\mu^2 \cdot B_0}{kT} \tag{5.7}$$

The magnetization will thus decrease with increasing temperature leading to smaller amplitudes of the detected signal. This temperature effect on the signal amplitude can be taken into account by multiplying the amplitudes with the absolute temperature. Those temperature corrected amplitudes, normalized to 20 °C, are given in table 5.2. For all temperatures, except for the two highest ones (60 and 80 °C) the normalized amplitudes are constant. The lower amplitudes for the two highest temperatures is probably due to evaporation of the pore water. This is confirmed by a repetition of the measurement at 20 °C after the heating to 80 °C. Now the normalized amplitude was 0.79, the same value as for the measurement at 80 °C. The lack of temperature dependence for the relaxation times is a prove for the fast diffusion regime. Previous experiments of the temperature dependence of NMR relaxation of water in natural rocks, with a broad pore size distribution, have also shown a weak or negligible effect (Roberts et al. [1995], Latour et al. [1992]).

For the *fast-diffusion* regime, a porous system with a distribution of pore sizes will lead to a correlated distribution of relaxation times. The challenge of *NMR relaxometry* is to extract the distribution of relaxation times from the FID envelope. As explained in chapter 4, this is an ill-posed problem that needs to be solved by regularization of the solution.

Table 5.2: Variation of T_2 and the temperature corrected amplitude of saturated sand samples

Temperature (°C)	T_2 (ms)	A_{corr} (normalized to 20 °C)
0	177 ± 8	1.01
5	179 ± 8	1.00
20	174 ± 7	1.00
40	193 ± 9	0.98
60	193 ± 9	0.93
80	184 ± 8	0.79

5.2.1.2 Relation between T_2 and pore size

Once the underlying distribution of relaxation times is found, the model described in Eq. 5.5 can be used to relate the relaxation time distribution to the pore size distribution when the relaxivity ρ is known. The relaxivity can be derived by analyzing the relaxation times of a set of porous samples of the same material with known pore sizes. The porous systems used for such a calibration are VitraPOR glass filter discs (ROBU Glasfiltergeräte GmbH, Germany) (see section 5.1.3). Because the relaxivity depends on the surface characteristics of the sample, the calibration will only be valid for systems with similar chemical surface properties. The chemical composition of the VitraPOR filter glasses (as listed in the product specifications) is given in table 5.3.

Table 5.3: Chemical composition of the VitraPOR glass filters

Element	% by weight
Silica (SiO_2)	80.60
Boric oxide (B_2O_3)	12.60
Sodium oxide (Na_2O)	4.20
Alumina (Al_2O_3)	2.20
Iron oxide (Fe_2O_3)	0.40
Calcium oxide (CaO)	0.10
Magnesium oxide (MgO)	0.05
Chlorine (Cl)	0.10

Because small amounts of paramagnetic impurities, like Mn^{2+} and Fe^{3+}, can be very effective relaxants, it is very important to clean the glass filters before measuring. The effect of three different cleaning procedures was tested.

- Initially the filters were cleaned several times with deionised water.

- The second cleaning procedure was based on an exchange reaction. Appelo and Postma [1999] showed that Cs^+ has excellent exchange properties for a broad range of ions on the surface of soil particles. Since the chemical composition of soil is relatively similar to the VitraPOR glass filters (both exist mainly out of SiO_2), Cs^+ is also expected to be able to exchange the paramagnetic ions absorbed on the surfaces of the filters. The filter discs were immersed in a solution of 0.5 M CsCl for a period of about one week. Afterwards the filters were washed repeatedly with deionised water.

- The third cleaning procedure was based on the procedure described in Holly et al. [1998]. The samples were first immersed in a acid solution of 50 % concentrated H_2SO_4 and 50 % concentrated HNO_3 for a 24 h period. To ensure that the acid fills all the pores, the immersed sample is placed in a vacuum three times for 2 min during this 24 h period. After the 24 h immersion period the acid is decanted. Ten successive washing cycles with distilled water, each having a vacuum established several times, ensure that all the remaining acid is washed out. The above process is repeated two times.

From those three methods the third one is of course the most aggressive and can only be applied on inert systems. This method is not applicable to natural systems such as soil samples because the concentrated acids will influence the chemical and physical structure and therefore change the characteristics of the pores. Deionised water and CsCl however, will not change the pore characteristics and can be used for sensitive systems where concentrated acids would affect the pore surfaces.

To measure the relaxation times a stack of seven cleaned filters were saturated with deionized water and sealed with Parafilm^{TM} to prevent evaporation. No weight loss could be detected after a few days. The transversal relaxation time distribution was determined using the BRD method (see section 4.1.7) where the optimal value for the regularization parameter was determined by the S-curve method (see section 4.1.6). The T_2 distributions for the six different filters cleaned with the mixture of concentrated H_2SO_4 and HNO_3 are displayed in figure 5.9.

Because all the filters are mono-disperse and have a relatively narrow pore size distribution, the FID envelopes of the samples can be in a first approximation fitted mono-exponentially. The value obtained by this fit corresponds with the center of the peaks in figure 5.9. The results of the mono-exponential fit for all filters are given in table 5.4 as well as the maximum values for the distribution of relaxation times for the acid cleaned filters.

Applying Eq. 5.6 and assuming spherical pores ($\alpha = 3$) leads to a relationship between the pore size and the transversal relaxation times depending on the bulk relaxation time ($T_{2,bulk}$) and surface relaxivity (ρ) and is displayed in figure 5.10 for the different cleaning procedures. The values for the two parameters are given in table 5.5.

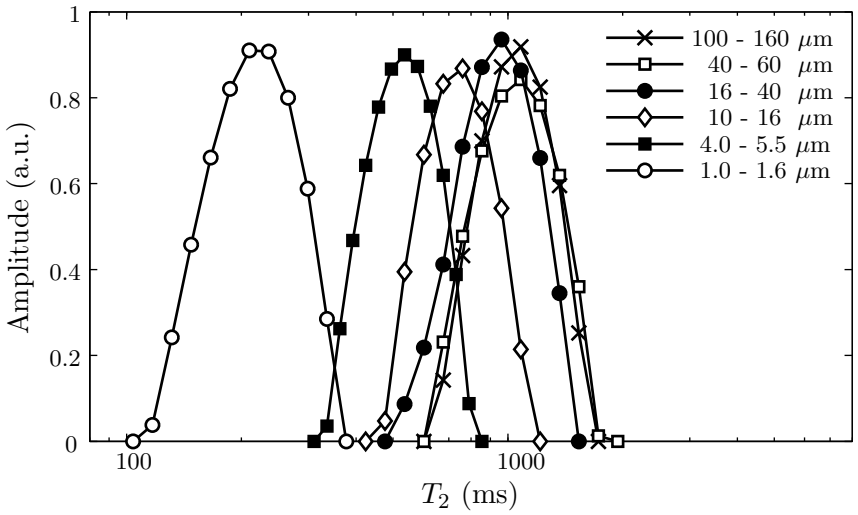

Figure 5.9: T_2 distribution for all VitraPOR glass filters cleaned with concentrated H_2SO_4 and HNO_3.

Table 5.4: Mono-exponential transversal relaxation times of water filled in VitraPOR glass filters after cleaning

Porosity	Nominal pore size (μm)	T_2 (s) after cleaning with			
		deionised H_2O	0.5 M CsCl	concentrated acid	
		mono-exp.	mono-exp.	mono-exp.	multi-exp. (peak max.)
1	100 - 160	0.840	0.890	1.118	1.081
C	40 - 60	0.810	0.894	1.020	1.081
3	16 - 40	0.720	0.730	0.980	0.961
4	10 - 16	0.610	0.627	0.833	0.760
F	4 - 5.5	0.450	0.471	0.533	0.535
5	1.0 - 1.6	0.175	0.208	0.224	0.209

Table 5.5: Fit parameters for the VitraPOR glass filters

Cleaning method	$T_{2,bulk}$ (s)	ρ (μm/s)
deionised H_2O	0.89 ± 0.16	1.97 ± 0.20
0.5 M CsCl	0.89 ± 0.15	1.60 ± 0.19
conc. acid	1.18 ± 0.05	1.56 ± 0.04

The values of the relaxivity parameter show its dependence on the cleaning procedure. The method that removes the most amount of impurities (cleaning with concentrated acid) leads

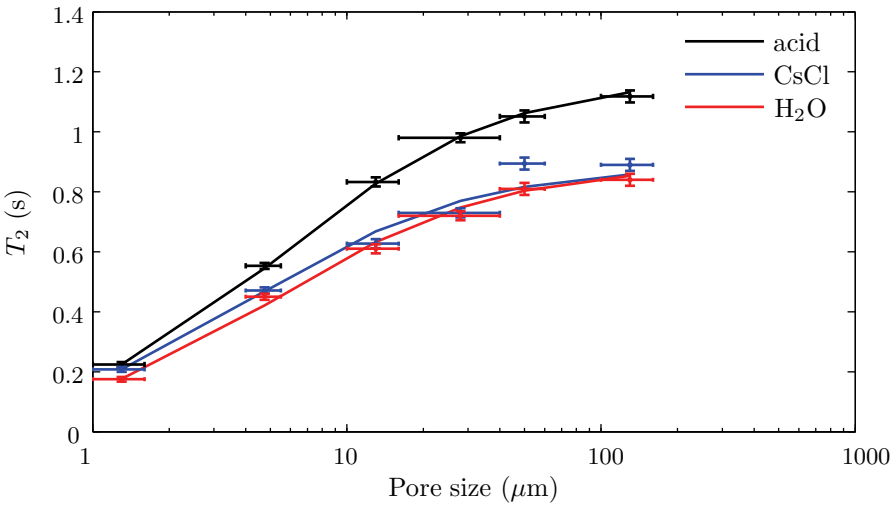

Figure 5.10: T_2 in function of the pore size for VitraPOR glass filters

to the lowest surface relaxivity. This dependence shows the strong effect of small amounts of paramagnetic impurities. In natural systems such as soil with relatively large amounts of ferromagnetic substances, the relaxivity will increase drastically.

Also the bulk relaxation time seems to depend on the cleaning procedure. Even after cleaning with concentrated acid, the bulk value does not reach the value for free water (≈ 1.8 s). To separate the bulk value for fluids confined in porous media from the bulk value of unconfined free fluids, we call the former the *bulk like* relaxation time. For the longitudinal relaxation, the *bulk like* relaxation time is also smaller as the bulk longitudinal relaxation time at low frequencies (see section 5.2.2). Mattea et al. [2004] explained the difference between both relaxation times by the fact that the rotational diffusion could be affected by the confinement even if the molecules are not directly adsorbed.

The T_2 values for the acid cleaned filter glasses are only moderately smaller than the T_1 values (see section 5.2.2), indicating that the additional relaxation processes that play a role in the transversal relaxation such as the dephasing of the magnetization due to the external and internal inhomogeneity do not have a major contribution in the overall relaxation processes after the cleaning procedure. The minor effect of the external inhomogeneity is not surprising because of the excellent homogeneity of the Earth's magnetic field and the extra measures that are taken to compensate the disturbances of the measuring field in the laboratory (see section 3.4.1.3). However, the internal magnetic gradients can not be compensated in the measurement method used in this work, but the strength of those internal inhomogeneities will depend on both the field strength and the difference in susceptibility between the pore fluid and the surface (see section 3.2). A comparison of the T_1 and T_2 values for the VitraPOR glasses ($T_{2,\text{bulk}} \approx 1.2$ s, $T_{1,\text{bulk}} > 1.6$ s) indicates that in the Earth's magnetic field, the effect

of the internal gradients does not play a major role.

Also the relaxivity depends on the cleaning procedure. The strongest cleaning results in the lowest relaxivity parameter. This is not surprising since the cleaning removes the strong relaxing paramagnetic ions from the particle surfaces. From both the changes in relaxation time and relaxivity parameter, it can be concluded that the concentrated acid is the most effective cleaning agent.

5.2.2 Longitudinal relaxation

In chapter 3.3 it was explained that the Earth's field NMR device is not only able to measure the transversal relaxation time, but can also measure the longitudinal relaxation time T_1. Because the latter is measured in the polarizing field, it is even possible to determine T_1 at different field strengths by changing the polarizing current. In this way the T_1 dispersion (T_1 in function of the Larmor frequency) can be measured for Larmor frequencies from about 3 kHz up to 3 MHz. T_1 at four different frequencies (3, 30, 300 and 3000 kHz) were measured for the six different saturated VitraPOR filter glasses and the results are given in figure 5.11. The model that relates pore size to relaxation time and that has been explained in the previous section, is also applied to the T_1 data:

$$\frac{1}{T_1} = \frac{1}{T_{1,\text{bulk}}} + \frac{1}{T_{1,\text{surface}}} = \frac{1}{T_{1,\text{bulk}}} + \rho_1 \frac{S}{V} = \frac{1}{T_{\text{bulk}}} + \frac{\alpha \rho_1}{r} \tag{5.8}$$

The values for the bulk relaxation time ($T_{1,bulk}$) and the surface relaxivity (ρ_1) are plotted versus the Larmor frequency in figure 5.12.

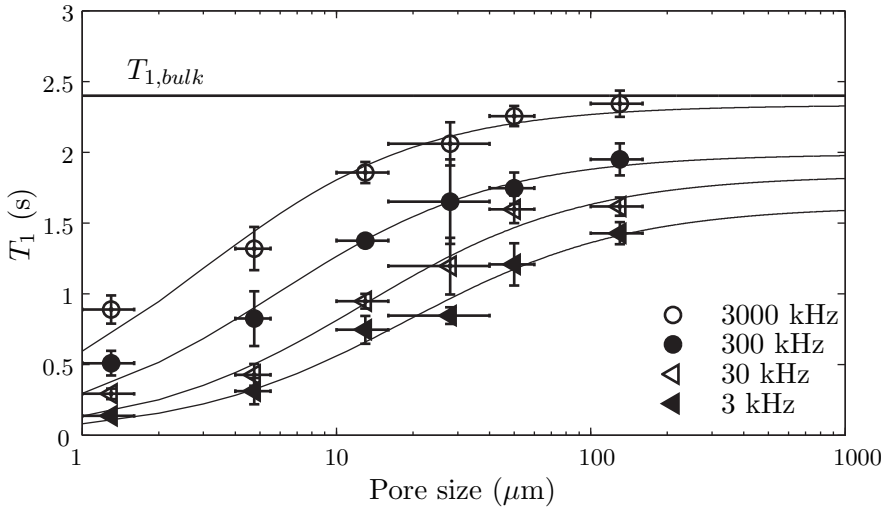

Figure 5.11: T_1 in function of the pore size and Larmor frequency for the VitraPOR glass filters. Solid lines: fit functions according to Eq. 5.8

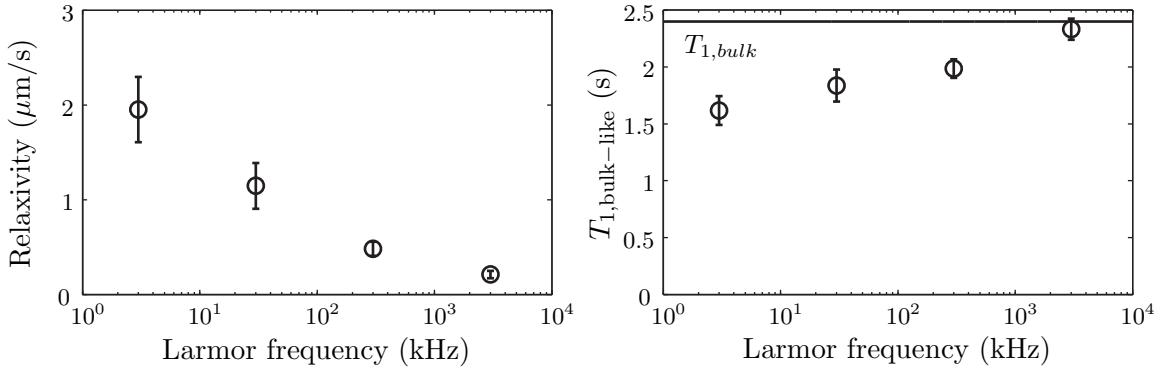

Figure 5.12: Surface relaxivity ρ and bulk-like relaxation time of the VitraPOR glass filters in function of the Larmor frequency

Both the surface relaxivity and the bulk spin-lattice relaxation time depend on the Larmor frequency: the surface relaxivity decreases and the bulk relaxation time increases with increasing Larmor frequency. This is contradictory to the model of Godefroy et al. [2001] where the frequency dependence is attributed solely to the surface relaxation, but corresponds to the model derived by Mattea et al. [2004] where the surface relaxivity as well as the bulk longitudinal relaxation times are frequency dependent. In the latter model the spin-lattice relaxation is predominantly caused by molecular reorientations, especially by *reorientations mediated by translational displacements* (RMTD) at the pore walls. The spin-lattice relaxation is thus interpreted purely on a diamagnetic basis, indicating that the influence of paramagnetic impurities, if still present after the cleaning procedure, is low. The increased relaxation at low fields shows that relaxation in the VitraPOR filter glasses is dominated by processes with relatively long correlation times. Measurements at low frequencies are therefore much more sensitive for the processes occurring at the solid-fluid interface.

Only at the highest Larmor frequency (3 MHz), the bulk relaxation time found for water confined in the porous system (2.33 s) corresponds well to the bulk relaxation time for free water (2.4 ± 0.1 s). For lower frequencies this value is significant lower (≈ 1.6 s), indicating that the molecular dynamics in the bulk like phase are different from the dynamics in bulk unconfined liquids, where no low-frequency dispersion is observed. Therefore it is better to call $T_{1,b}$ the *bulk-like* spin-lattice relaxation time to distinguish it from the bulk relaxation time of unconfined water. A possible reason for the difference between the *bulk-like* and the bulk spin-lattice relaxation time could be the fact that the rotational diffusion is affected by the confinement even if the molecules are not directly adsorbed (Mattea et al. [2004]).

The T_1 values for the VitraPOR filter glasses with the smallest pore sizes (VitraPOR 5) are compared with literature values found in Mattea et al. [2004]. In this work, the glass filters were pretreated by boiling them for 60 min in 30 % H_2O_2. The comparison of the values

in table 5.6 shows that for commercial porous glasses the method used in this work (direct analysis of the FID envelope) gives similar results for T_1 measurements as the traditional CPMG method.

Table 5.6: Comparison between T_1 values found in this work and literature values (Mattea et al. [2004]) for VitraPOR5

Larmor frequency (kHz)	T_1 (s) this work	T_1 (s) (Mattea et al. [2004])
3	0.14 ± 0.02	0.22
30	0.29 ± 0.04	0.28
300	0.51 ± 0.09	0.48
3000	0.89 ± 0.10	0.67

5.2.3 Determination of the pore size distribution by ENMR relaxometry

Using Eq. 5.5 the pore size distribution of a porous sample can be derived from the spectrum of relaxation times when the relaxivity ρ is known. Although the relaxivity is sample specific, we will use the values found for the VitraPOR glass filters for two unknown porous systems because both the glass filters and the unknown samples exists mainly of silica (> 80 %) and have a low concentration of (paramagnetic) impurities.

The porous samples were produced by the Ceramic working group (Department of Production Engineering at the University of Bremen) using the *freeze cast* method in which an aqueous slurry of alumina (87 %) and silica sol (13 %) is cast and freezed in a metallic cylindrical mold with diameter of 24 mm and a length of 50 mm. Since freezing of aqueous sols or powder suspensions include the nucleation and growth of ice crystals, the evolving microstructure, in particular the pore characteristics which are left behind after elimination of the solvent, can be controlled by the freezing process (Koch et al. [2003]). As the cooling/freezing front proceeds from the cooled surface to the interior of the slurry, a strong gradient evolves in the factors that affect the porosity. With increasing distance from the cooled surface, the pore sizes increase. The generation of the corresponding macropores appears to be very sensitive to the freezing parameters. This can be seen clearly in figure 5.13 where two electron microscopy images from the inner and the outer region of the first freeze cast sample (FC1) are displayed. The pores at the inner region of the sample are clearly larger then the pore at the outer regions. In this way the freeze cast method allows to produce porous systems with adjustable ranges of pore size.

After drying and sintering of the two freeze cast samples by the Ceramic working group, the samples were transferred to the EFNMR laboratory and saturated with water under a

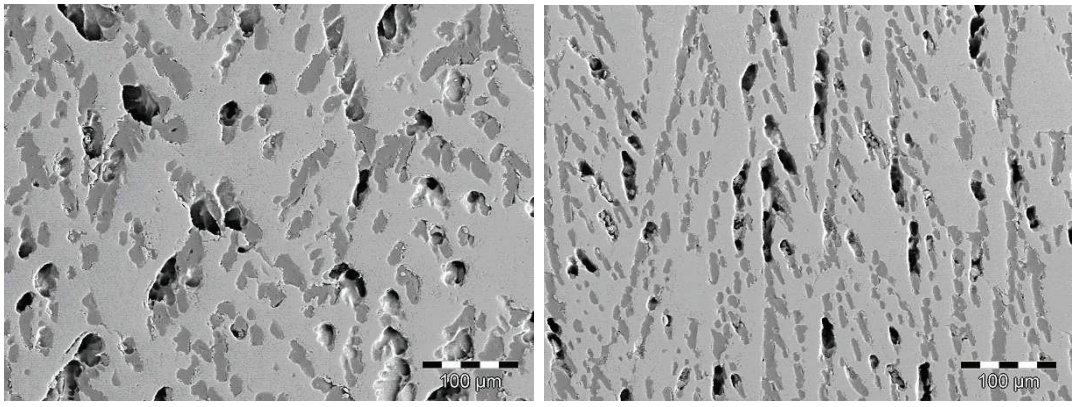

(a) inner pores (b) outer pores

Figure 5.13: Scanning electron microscopy image of the inner and outer pores of freeze cast sample FC1

vacuum followed by sealing with Parafilm^{TM} to prevent evaporation. No weight loss could be detected after a few days. From the measured FID envelope of the saturated porous systems, the relaxation time distributions are derived by the use of the BRD method (see section 4.1.7) where the optimal regularization parameter α is determined by S-curve method. The relaxation time distributions of the two freeze cast samples are given in figure 5.14. The samples have two distinct T_2 distributions. Sample FC1 has one very narrow peak around 850 ms and sample FC2 has two broader peaks, a larger one around 500 ms and a smaller one at around 30 ms.

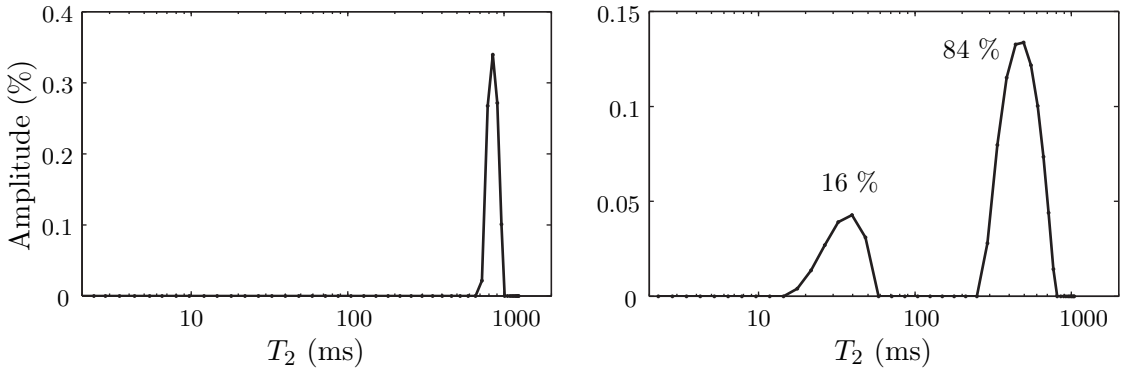

Figure 5.14: T_2 distribution of the two freeze cast samples FC1 and FC2

This distribution of transversal relaxation times is converted to a pore size distribution with the use of Eq. 5.6 where T_b and ρ are replaced by the values found for the VitraPOR glass filters cleaned with the concentrated acid. The pore size distributions of both samples is compared with mercury intrusion porosimetry (MIP) data in figure 5.15. The MIP measurements

were performed on both freeze cast samples after the FID measurements (MIP is a destructive method) by the Ceramics working group. As already explained in chapter 2.2.3, the pore size distribution found by NMR relaxometry can be quite different from the distribution found by MIP due to the fact that in relaxation measurements *size* tends to correspond to pore dimensions, while in mercury intrusion porosimetry *size* corresponds to the dimensions of the pore *throats*, the channels connecting the pores. From figure 5.15 it can be seen that for both samples both methods give quite similar results, which indicates that the size of the pore throats have the same order of magnitude as the pores, which can also be seen from figure 5.13.

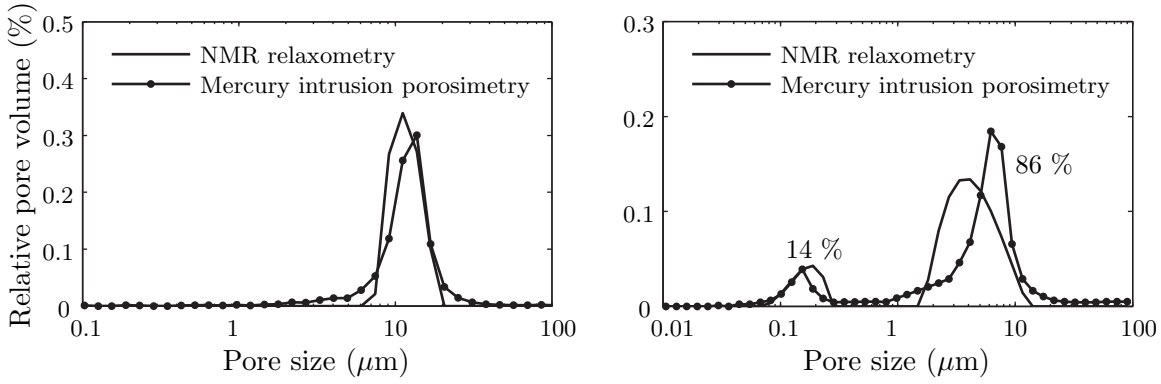

Figure 5.15: Pores size distribution derived by Earth's field NMR relaxometry and mercury intrusion porosimetry of the two freeze cast samples FC1 (left) and FC2 (right)

The good agreement between the two methods for both porous systems also shows that the surface relaxivity of the VitraPOR glasses can be applied to the freeze cast samples. However, when this is not the case, i.e. when there is no information about the relaxivity, the NMR relaxation data can still be used to analyze the porous system. In figure 5.14 the distribution has not been converted yet to the pore radius size, but it allows to derive some conclusions about the distributions of the pores: mono-modal porous systems can clearly be discriminated from multi-modal systems, just by looking at the T_2 distribution. For a weighting between the different pores, a scaling from T_2 to pore sizes is also not necessary. The relative weights of the two peaks of the bimodal sample in the T_2 distribution spectrum correspond very well to the weights found by mercury intrusion porosimetry (see figure 5.14 and 5.15).

5.3 Earth's field NMR of natural soil samples

In the previous sections, the longitudinal and transversal relaxation times of different porous systems with a more or less known chemical composition and a low content of paramagnetic impurities were determined. In a next experiment the relaxation times of a natural soil

sample are analyzed. The soil was selected from the reference soils (RefeSol) provided by the Fraunhofer Institute for Molecular Biology and Applied Ecology, Schmallenberg, Germany. The soil 04-A was chosen, a sandy soil (85 % sand) with a relatively low iron concentration (Fe_{ox} = 0.63 mmolc/kg). The air dried soil was saturated and filled into a sample bottle of 25 ml. The FID envelope measured by the Earth's field NMR device is given in figure 5.16 together with the corresponding T_2 distribution.

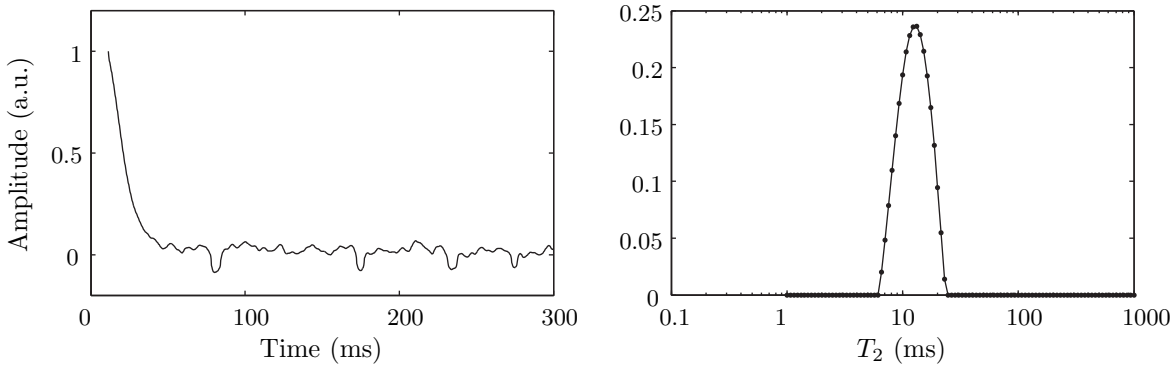

Figure 5.16: FID envelope and corresponding T_2 distribution of the sand sample 04A measured with the Earth's field NMR device (at 2050 Hz)

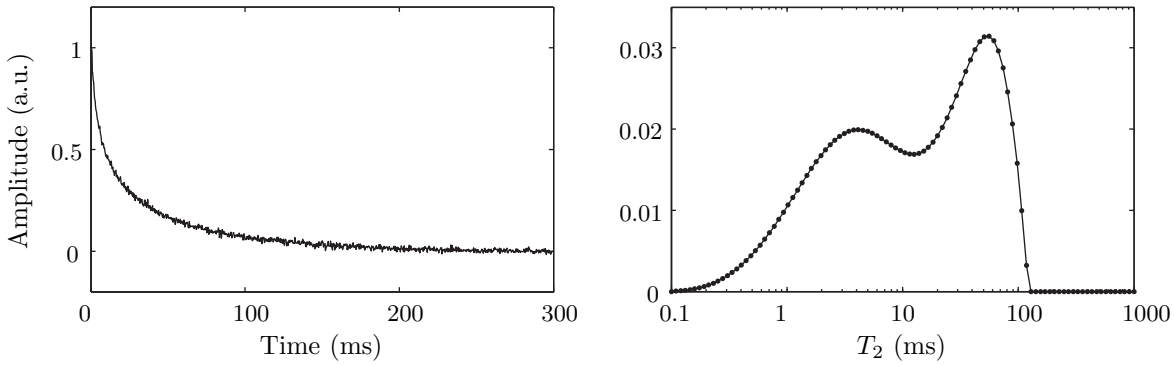

Figure 5.17: CPMG magnetization decay and corresponding T_2 distribution of the sand sample 04A measured with a 2 MHz relaxometer (Maran 2, Resonance, UK)

The magnetization decreases very rapidly and a narrow spin-spin relaxation time distribution around about 10 ms was determined by the regularization method. Although the measured soil sample consists mainly of sand, the relaxation times are more than one order of magnitude smaller than the relaxation times of the clean sand sample (see figure 5.2). This indicates that the soil sample 04A contains a lot of paramagnetic centers enhancing the relaxation dramatically. However, a comparison with the magnetization decay measured by a CPMG pulse sequence measured with a 2 MHz relaxometer (Maran 2, Resonance, UK) (Jaeger et al.

[2006], personal communication) shows that the T_2 distribution derived by this method is much broader and also contains components with much longer relaxation times.

The narrow distributions derived by the direct analysis of the FID envelope and located at the center of the distribution found by the CPMG sequence, indicates that the paramagnetic impurities play a major role in the magnetization decay. The difference between the distribution found by the EFNMR method and by the CPMG method could be explained by the fact that the gradients induced by the paramagnetic impurities have a length scale that exceeds the diffusion length scale (Kleinberg et al. [1994]). Due to the applied pulses during a CPMG experiment, the effect of the impurities can be canceled out and the relaxation time distribution will only depend on the pore size. In contrast, during the FID experiment, this inhomogeneity effect is not canceled out and the resulting relaxation time distribution will mainly depend on the concentration of paramagnetic impurities and not on the pore size.

The overall relaxation in a pore can be written as the sum of the relaxation due to the interactions between the pore fluid and the solid material and the extra decay due to the internal inhomogeneities:

$$1/T_2^* = 1/T_2 + 1/T_{2inhom}. \tag{5.9}$$

In Eq. 5.9 we write explicitly T_2^* as is usual in NMR to distinguish the overall transversal decay from the purely spin-spin relaxation without internal inhomogeneity effect ($1/T_2$). This internal inhomogeneity effect is compensated in the CPMG method, but not in the method used in this work. This means that, even in the Earth's magnetic field, where the internal inhomogeneity is expected to be much smaller than in high fields (see section 3.2), the FID decay is influenced considerably by the internal field inhomogeneity for samples that contain paramagnetic impurities. This shows that the possibility to decrease the effect of the internal inhomogeneity by lowering the field strength is limited. Unlike for samples with very low paramagnetic impurities (see section 5.2), no exact information about the pore size can be derived from the FID envelope of real soil samples measured by the EFNMR device.

Implementing spin-echo techniques in the experimental set up of the Earth's field NMR device would be a possible way to deal with this problem. But due to the technical complexity of such a modification (it is very difficult to implement pulses with short pulse intervals due to the long dead time), we will concentrate on systems that do not have large amounts of paramagnetic impurities, i.e. systems with small susceptibility differences, such as porous glasses (see previous sections) and gel systems (see following sections). Moreover, further experiments with soils that contain even more iron, showed to have even shorter relaxation times. Since the EFNMR device has a dead time of about 8 ms (see section 3.4.3), it becomes very difficult to analyze systems with such short relaxation times because most of the magnetization has already decayed before the signal is recorded. Even with pulse sequences it would be impossible to derive the T_2 distribution as displayed in figure 5.17 because the

EFNMR device can only detect relaxation times larger than 5 ms. Therefore, the EFNMR device will only be applicable to systems with very low paramagnetic impurities.

5.4 Earth's field NMR relaxometry of polymer gels

5.4.1 Relation between polymerization degree and relaxation time

In the previous sections, the relaxation times of saturated and unsaturated porous systems were analyzed. For systems with no or very low amounts of paramagnetic impurities, the relaxation time depends directly on the pore geometry and the relaxometry data can be used to determine the pore size characteristics qualitatively. When the relaxivity is known, the pore size characteristics can even be determined quantitatively. In a similar way the polymerization degree of a polymer might be determined.

According to the BPP theory (see section 2.2) proton spin-spin relaxation and spin-lattice relaxation is governed by the rate of molecular tumbling and Brownian motion of the molecules which results in a change of the efficiency of dipolar coupling between neighboring protons. The relaxation rates are thus correlated with the mobility of the protons. Physical or chemical processes that influence the mobility will therefore also influence the relaxation times. E.g. when a large molecule is formed by a polymerization reaction in an aqueous environment, the mobility of the surrounding water molecules will decrease with increasing polymerization and the relaxation times of the water molecules will decrease.

To illustrate the changes in relaxation times during a polymerization reaction, the spin-spin relaxation time during the formation of silica gel was continuously measured. The silica gel was produced at the Ceramic working group (Department of Production Engineering at the University of Bremen) by a condensation reaction of alkoxysilanes particles in an aqueous environment leading to an irregular, branched three-dimensional network of the polymer. Together with the confined water, this three-dimensional network will form a gel structure. The closer the network, the lower the mobility of the enclosed water molecules and the lower the relaxation time. During this gelation process, two reactions are taking place in parallel:

$$\text{hydrolysis}: \quad \begin{matrix}\backslash\\ -\text{Si}-\\ /\end{matrix}\text{OR} + \text{H}_2\text{O} \quad \xleftrightarrow{\text{acid or base}} \quad \begin{matrix}\backslash\\ -\text{Si}-\\ /\end{matrix}\text{OH} + \text{ROH} \tag{5.10}$$

$$\text{condensation}: \quad \begin{cases} \begin{matrix}\backslash\\ -\text{Si}-\\ /\end{matrix}\text{OH} + \text{HO}-\text{Si}\begin{matrix}/\\ -\\ \backslash\end{matrix} \longleftrightarrow \begin{matrix}\backslash\\ -\text{Si}-\\ /\end{matrix}\text{O}-\text{Si}\begin{matrix}/\\ -\\ \backslash\end{matrix} + \text{H}_2\text{O} \\ \begin{matrix}\backslash\\ -\text{Si}-\\ /\end{matrix}\text{OR} + \text{HO}-\text{Si}\begin{matrix}/\\ -\\ \backslash\end{matrix} \longleftrightarrow \begin{matrix}\backslash\\ -\text{Si}-\\ /\end{matrix}\text{O}-\text{Si}\begin{matrix}/\\ -\\ \backslash\end{matrix} + \text{ROH} \end{cases} \tag{5.11}$$

Parameters which influence the position of the equilibrium of the hydrolysis and condensation reactions, such as the pH, will influence the kinetics of the overall polymerization reaction and

can be used for materials design (Hüsing and Schubert [1998]). Acidic conditions will favor hydrolysis and the condensation will be the rate determining step. In contrast, hydrolysis is the rate-determining step under basic conditions. The influence of the pH on the kinetics of the polymerization reaction can be visualized by a continuous measurement of the transversal relaxation time distribution during the chemical reaction (see figure 5.18). Those figures are produced by measuring the FID envelope about every 10 s. For every envelope the corresponding relaxation time distribution is calculated. The whole set of relaxation time distributions is then stacked next to each other in function of the time of the FID envelope measurement. In this way, the temporal change of the relaxation time distribution can be made visible. Plotting the temporal variation of the relaxation time distribution is sometimes called *NMR relaxography* (Bruvold et al. [2007]).

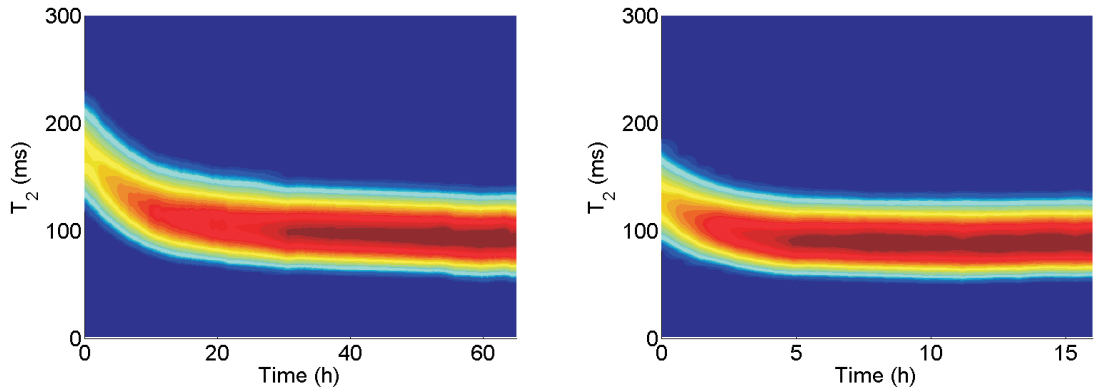

(a) pH=10.0 (b) pH=6.9

Figure 5.18: Evolution of the transversal relaxation time during the polymerization of silica gel for two different pH values. Mind the different time scales.

NMR relaxography performed in the Earth's magnetic field can thus be used to visualize chemical reactions that have an influence on the mobility of protons in a non-invasive way. By analyzing the time dependence of the relaxation time distribution, the progress of the polymerization reaction can be monitored in real time and information about the kinetics can be derived. The decrease in the relaxation time in figures 5.18(a) and 5.18(b) illustrates the increasing immobility of the enclosed water molecules when the polymerization reaction proceeds. Both cases presented in figure 5.18 result in the same distribution of relaxation times: a relatively narrow distribution between 60 and 140 ms. However, the polymerization reaction at a pH of 10 is much slower than the the polymerization at pH of 6.9. In the first case the polymerization reaction is even not fully completed after 60 hours, while in the second case the distribution has reached its final value already after 8 hours. Both distributions are getting slightly narrower at the end of the reaction (visible by the increased (dark red) intensities of the amplitude) which indicates that the branched three-dimensional network is

getting denser. The decreasing relaxation time of the surrounding water is thus a measure for the increasing polymerization degree of the silica gel and the relaxation time distribution is a relative representation of the molecular weight distribution in the polymer. Absolute values of the molecular weight distribution would be possible after calibration with standards of a known molecular weight.

To determine the molecular weight distribution of polymers by commercially available measurement methods such as viscosimetry or laser light scattering, a separation of the different molecular weight fractions (usually done by Gel Permeation Chromatography (GPC)) before the actual determination of the molecular mass is necessary. Since NMR relaxometry allows to determine the complete underlying distribution of relaxation times with a single measurement (by the inverse Laplace transformation, see chapter 4), the time consuming separation of the different fractions is not necessary. The only prerequisite to use NMR relaxometry to determine the molecular weight distribution is that the polymer has to be surrounded by a proton rich fluid which mobility changes with increasing polymerization degree.

Gels are very suitable systems to be measured with Earth's field NMR with a direct analysis of the FID envelope. Since gels consist mainly of water (usually $> 80\%$) immobilised by a thin skeleton of polymers and forming one homogeneous phase, the susceptibility differences in the sample will be negligible. Furthermore, the chemcial composition of the gel is in most cases perfectly known so that unwanted effects by paramagnetic impurities can be excluded. Therefore, the difficulties that arise for soil samples or other porous systems (susceptibility differences, paramagnetic impurities) are not a major issue anymore when gels are measured.

5.4.2 Earth's field NMR gel dosimetry

Because some polymerization reactions can be induced by irradiation (see below) and the relaxation times of the water protons enclosed by the polymer network are directly correlated to the polymerization degree, the relaxation times can be used to determine the dose after irradiation (e.g. Gore et al. [1984], Maryanski et al. [1993]). In standard gel dosimetry experiments, the absorbed dose after irradiation is determined in a phantom filled with a gel by the measurement of the spatial distribution of relaxation times by magnetic resonance imaging (MRI). By such a gel dosimetry experiment it can be checked (after calibration) if the target region receives the wanted energy dose and if the surrounding regions are saved from too high absorbed doses.

To relate the relaxation time to the absorbed dose, other parameters that influence the relaxation time such as pH, temperature, monomer concentration have to be constant. The most frequently used gels in gel dosimetry contain water, gelatin and acrylamide or methacrylic acid (e.g. Maryanski et al. [1994], De Deene et al. [2002]). Because oxygen inhibits the radiation

induced free-radical chain polymerization, also an oxygen scavenger is added (usually THP, bis-tetrakis(hydroxylmethyl)phosphonium sulphate) (De Deene et al. [2006]). The gelatin is used to prevent diffusion and makes the system spatially and temporally stable so that spatial information can be stored, making 3D dosimetry possible. The gelatin also shortens the relaxation times of the water protons significantly by forming a three-dimensional network where the polymerization of the monomer (e.g. methacrylic acid) will take place.

The gel used in this work is a nMAG gel (normoxic methacrylic acid gel based on the formula given in De Deene et al. [2006]: 86 % water, 8 % gelatin, 6 % methacrylic acid and 2 mM THP). Since the major part of the gel exists out of water, the water protons will be the main source of contribution to the NMR signal. Furthermore, measurements with pure gelatine and pure methacrylic acid showed that the relaxation times of the protons of the gelatin and the polymer are too short to be detectable with the Earth's field NMR device. When in the following sections the term *water protons* is used, it refers to the protons of the immobilized water-monomer solution in the gel.

The gelatin was added to 60 % of the water, heated to 45°C and stirred until the gelatine is completely solved in the water (after about 15 minutes). The gelatin-water solution was then cooled to 35°C and added to the methacrylic acid that was solved in the rest of the water. 2 mM THP was added under strong stirring and the mixture was transferred to 25 ml sample bottles. To further cool down, the samples were placed in the refrigerator where the gelation reaction took place.

To visualize the gelation reaction, one sample bottle was not stored in the refrigerator but placed in the EFNMR device and the FID envelopes were measured continuously for a period of several hours (see figure 5.19). To have the same conditions as in the refrigerator, the air flow around the sample was kept at 7°C. At the beginning of the gelation reaction the water in the sample still behaves like free water with a transversal relaxation time at around 1.5 s. Soon, the relaxation time starts to decrease because the gelatin immobilizes the water molecules and a gel structure is formed. After about 30 minutes most of the water has been immobilized in the gelatin structure and the relaxation has decreased to about 450 ms. To assure that the gel has reached its final structure before the irradiation, the samples were stored during 24 hours in the refrigerator.

The polymerization reaction of the methacrylic acid in the gel will be initiated by ionizing radiation. The samples were irradiated by a Theratron 780-C ^{60}Co unit at the Pius Hospital in Oldenburg, Germany. Just before the radiation the samples were warmed up to 20°C by placing them in a water bath. During radiation and all following steps (transport and relaxation time determination) the temperature was kept constantly at 20°C. By the use of a plexiglass sample holder that was especially constructed for this work, three samples could be irradiated simultaneously. More information about the radiation of the samples can be found

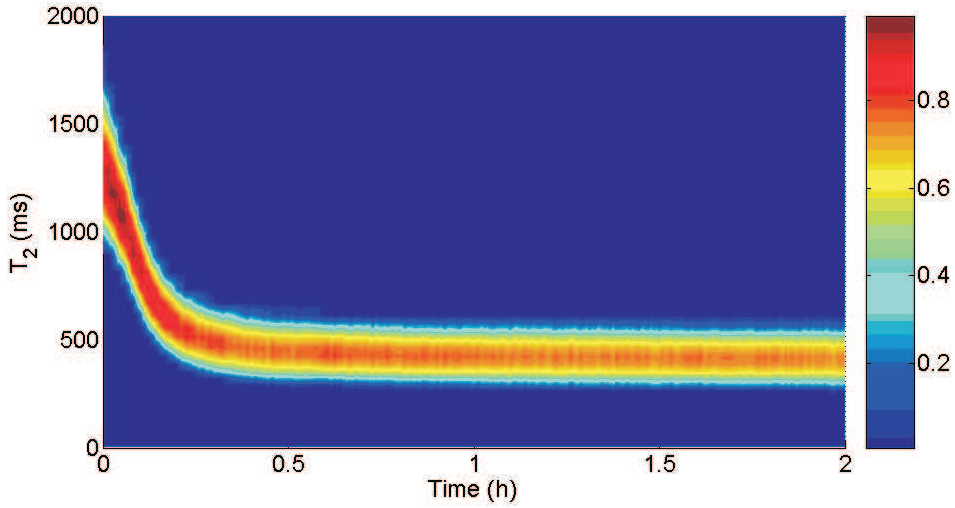

Figure 5.19: Evolution of the transversal relaxation time of the water molecules during the gelation process of the nMAG gel (normoxic methacrylic acid gel: 86 % water, 8 % gelatin, 6 % methacrylic acid and 2 mM THP) at 7°C

in Bislich [2007].

The ionizing radiation splits the water molecules into radicals (*initiation reaction*):

$$H_2O \longrightarrow {}^{\bullet}H + {}^{\bullet}OH \tag{5.12}$$

The concentration of those radicals depends on the applied dose. The radiation unit had a dose rate of 0.268 Gy/min. By changing the irradiation time different doses can be applied. To achieve a dose of e.g. 5 Gy the samples had to be irradiated for 18.66 minutes. The hydroxyl radicals induced by the irradiation will react with the double bound of the monomer and the reactive radical will be transfered:

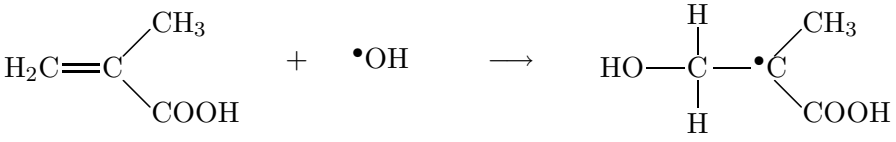

(5.13)

The reactive monomer will react with other monomers and long linear chains are formed

(*propagation reaction*):

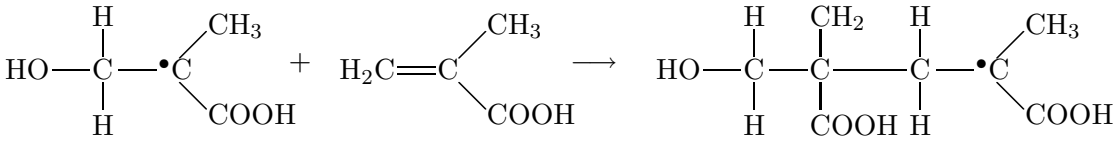

(5.14)

This reaction will proceed until no monomer is available anymore or two radical molecules recombine to form a non radical product (*termination reaction*). The polymerization degree will thus depend on the concentration of radicals which depends on its turn on the applied radiation dose. After the radiation by the Theratron 780-C ^{60}Co unit, the samples were transferred to the EFNMR laboratory where the FID envelopes of the samples were measured. In figure 5.20 the accumulated (20 accumulations) FID envelopes of 10 samples irradiated with doses varying from 0 to 5.0 Gy are displayed. It can be clearly seen that higher doses lead to shorter relaxation times due the increased polymerization that enhances the immobilization of the water molecules enclosed in the polymer network. The signals of the gels having received

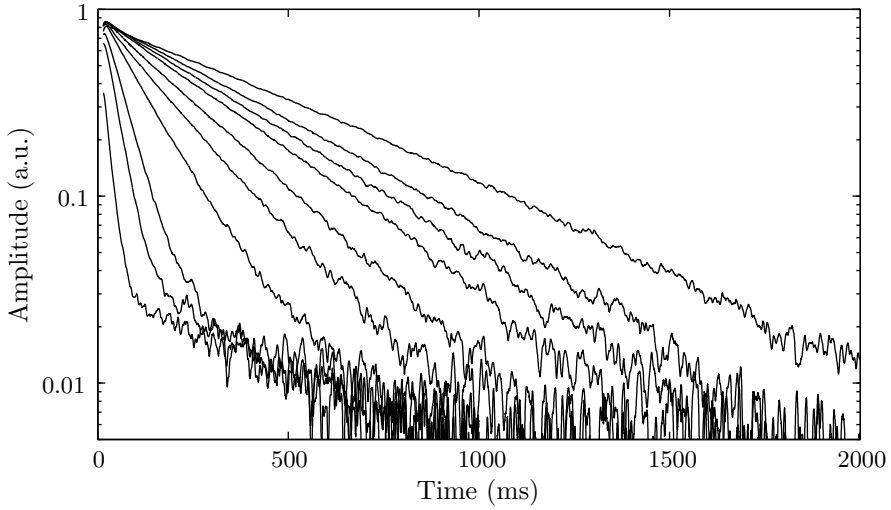

Figure 5.20: The FID envelopes of a nMAG gel irradiated with different doses: from top to bottom 0, 0.1, 0.2, 0.3, 0.5, 0.7, 1.0, 2.0, 3.0 and 5.0 Gray

the lowest dose (0, 0.1, 0.2 and 0.3 Gy) are perfectly linear over a range of two orders of magnitude. The values of the relaxation times are given in table 5.7. The residues of a mono-exponential fit of the non-irradiated sample are displayed at the top of figure 5.21. The mono-exponential model can fit the experimental data very well as can be seen from the small and symmetrically distributed residues around zero. The mono-exponential behavior is also seen in figure 5.22 where the distributions of the relaxation times are displayed. The distributions are derived by the BRD regularization method (see section 4.1.7) where the right

level of regularization is carefully determined by the S-curve method so that the broadness of the peaks can be attributed to the physical properties behind the data and not to an improper choice of the regularization level. The mono-exponentiality of the first gels is reflected by the very narrow single peaks in the relaxation time distribution. The peaks are shifting to lower relaxation times with increasing dose.

Table 5.7: Transversal relaxation times in function of the applied dose

Dose (Gy)	T_2 (ms)				
	Mono-exponential	Bi-exponential			
0	512 ± 20				
0.1	392 ± 12				
0.2	324 ± 36				
0.3	276 ± 4				
0.5	215 ± 8				
0.7	157 ± 7				
1.0	125 ± 5	113 ± 3	(92.6 %)	343 ± 54	(7.3 %)
2.0	64 ± 2	51 ± 2	(95.2 %)	388 ± 44	(4.8 %)
3.0	41 ± 1	32 ± 1	(95.7 %)	454 ± 26	(4.3 %)
5.0	28 ± 1	19 ± 1	(95.9 %)	467 ± 25	(4.1 %)

At intermediate doses (0.5 - 1.0 Gy) the magnetization decay can not be fitted perfectly by a straight line. The residues of a mono-exponential fit for the sample irradiated with 0.5 Gy are displayed in the second graph of figure 5.21. The residues are not symmetrically spread around zero indicating multi-exponentiality. A discrete fit with more components resulted in unstable solutions with similar values for the different T_2 components. This suggests a broad but mono-modal distribution and is confirmed by the distributions in the relaxation times in figure 5.22. The center of the peak shifts to lower values with increasing dose as can be seen from the values of the discrete mono-exponential fit listed in table 5.7.

The gels with the highest dose (1.0, 2.0, 3.0 and 5.0 Gy) show two clearly separable components: a large fast component and a small slow component. Due to the large differences between the two components, they can be fitted by a discrete bi-exponential model. The residues for such a bi-exponential fit for a sample irradiated with 5 Gy are given at the bottom of figure 5.21. The bi-exponential model clearly fits the experimental data much better than the mono-exponential model. Although the weighting factors of the components with long relaxation time is small (around 5 %, see table 5.7), large errors are made when this component is neglected as can be seen from the difference between the values of the mono- and bi-exponential fit in table 5.7 and from the residues of the mono-exponential fit at the bottom of figure 5.21. The fast component seems strongly dose dependent, while the dose

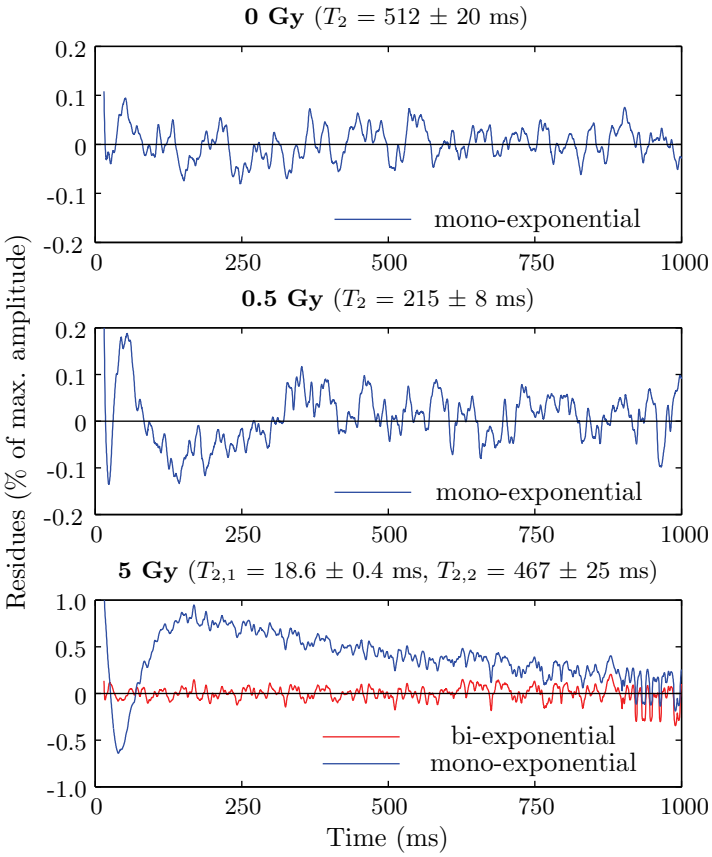

Figure 5.21: The residues of mono- and bi-exponential fits for the nMAG gel irradiated with 0 Gy (top), 0.5 Gy (center) and 5 Gy (bottom)

dependence of the slow component is much smaller. From figure 5.22 it can be seen that the large dose dependent peak is broader than the peak for the gels at the low doses, but narrower than the peaks at intermediate doses.

It seems that the component with a long relaxation time that was measured at small doses, disappears at intermediate doses and appears again at high doses. This unexpected behavior could be an artifact of the data analysis. However, also when a component with a relaxation time at around 400 ms was explicitly searched (by a fit with a fixed relaxation time) for the gels with intermediate doses, the unsymmetrical distribution of the residues of such a fit did not suggest the presence of this component. Altogether, three regimes can thus be distinguished:

- At low doses, the gels are characterized by relatively large mono-exponential relaxation times (small rates) that are dose dependent. The mono-exponential behavior suggests that all water molecules are immobilized in the same way and that there are no isolated

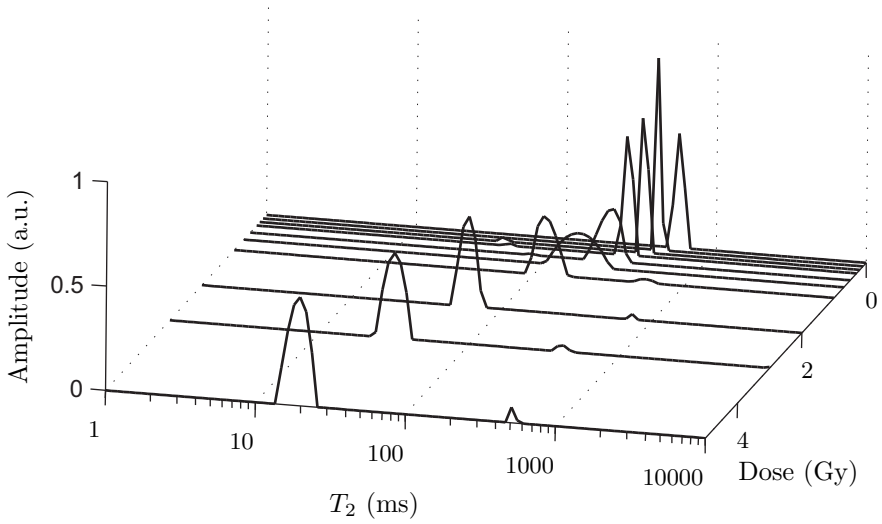

Figure 5.22: The distributions of the transversal relaxation times for nMAG gel in function of the dosis

regions that are leading to a distribution of the degree of immobility. A schematic picture of the structure of the polymer gel in this regime is given in figure 5.23a.

- At intermediate dose levels, the broad distributions of relaxation times indicates that the polymerization has formed a denser homogeneous network with some isolated regions, each with a specific immobilization of the enclosed water molecules. The mean value of this peak is dose dependent. A schematic picture of the structure of the polymer gel in this regime is given in figure 5.23b.

- At high doses, the distributions of the relaxation times have two clearly separated peaks, suggesting that two pools of water protons have developed. The broad and strongly dose dependent peak originates probably from a very dense network of polymer chains that form narrow distributed isolated regions, each with a specific immobilization of the enclosed water molecules. The mean value of this peak correlates very well with the applied dose, while the correlation with the applied dose of the mean value of the small peak is much smaller. The location of the latter peak corresponds well with the peak at zero dose, indicating that, in contrast to the previous regime where the polymer network is homogeneously distributed over the sample, the polymer chains are now forming clusters and between those clusters a small amount of relatively mobile water is situated. A schematic picture of the structure of the polymer gel in this regime is given in figure 5.23c.

The three regimes can be distinguished by their relaxation times: the low dose regime has relaxation times larger than 200 ms, while relaxation times in the high dose regime are smaller or equal to about 100 ms. The absolute values of the relaxation times are probably strongly

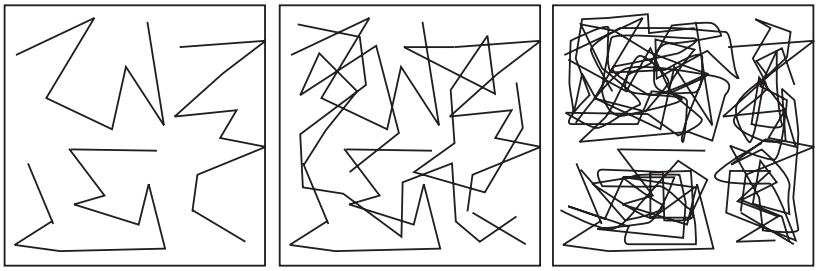

(a) low dose (b) intermediate dose (c) high dose

Figure 5.23: Schematic view of the polymer gel in the three different regimes

depending on the gel and could vary from batch to batch. However, the different physical processes during the polymerization, as displayed in figure 5.23, will be probably generally valid and a distinction between the different regimes by analyzing the shape of the relaxation time distribution can be used for different kinds of gels. All regimes have clearly discernible features: the low dose regime has one single dose dependent and very narrow peak, the intermediate regime has one broad dose dependent peak and the high dose regime has two clearly separated peaks, a large broad peak that is strongly dose dependent and a small peak with much lower dose dependence.

Although being complex over the whole dose range, the relationship between the dose and the relaxation rate is linear within each regime (see figure 5.24). To get an idea about the reproducibility of the data, the average together with the lower and upper extreme values from three independent gel samples (from the same batch) are displayed. In table 5.8 the sensitivity (the increase in relaxation rate per Gray) is given for every regime. The accuracy of the gel dosimeter is analyzed by taking the highest difference between the lower and the upper value within each regime as a measure for the uncertainty of the method.

Table 5.8: Sensitivity of the different dose regimes for a nMAG gel

Dose	T_2 distribution	Sensitivity (s^{-1}/Gy)	R^2	Accuracy (Gy)
low	mono-exponential	5.4 ± 0.3	0.992	0.06
intermediate	one broad peak	7.6 ± 1.1	0.970	0.10
high	two components			
	large, dose dependent	11.3 ± 0.3	0.999	0.11
	small, dose independent			

Due to the separation in three different regimes, a linear correlation between the dose and the relaxation rate with high correlation coefficients can be found for the whole dose range. The sensitivity increases from 5.4 for low doses till 11.3 s^{-1}/Gy for high doses. This is a factor

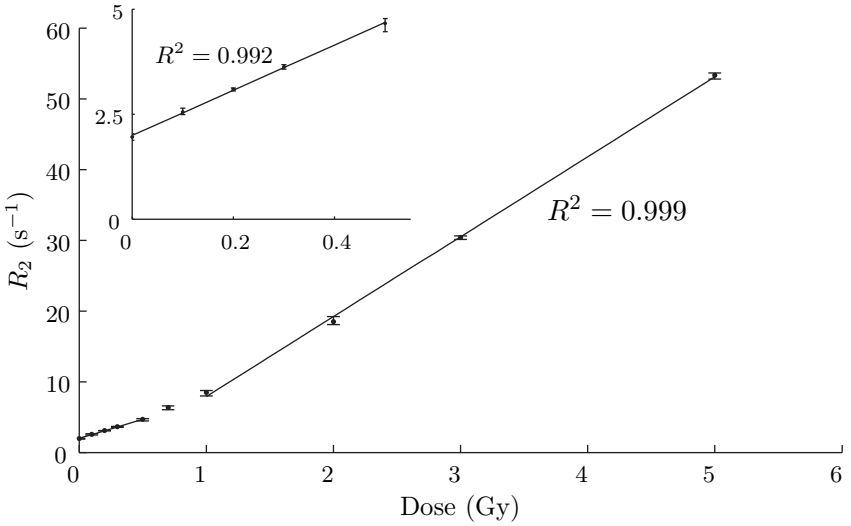

Figure 5.24: The transversal relaxation rates of the dose dependent components of the nMAG gel in function of the dosis. The average (dots) and the upper and lower extreme values (errorbars) out of three samples are displayed. The line represents the linear relation (see Table 5.8). The inlet shows an enlargement at the low doses.

4 to 5 times larger as for the same gel in high magnetic fields (De Deene et al. [2006]). This enlarged sensitivity is due to the more effective relaxation at low magnetic field strengths (see section 3.2) and is similar with the effect found in porous systems were the relaxation rates also increase with decreasing Larmor frequency (see section 5.2.2). Although the dispersion for R_2 (=$1/T_2$) will be less pronounced, the R_1 (=$1/T_1$) dispersions in figure 5.25 are giving a good impression of the advantage of using ultra low fields in gel dosimetry. The difference in relaxation rates between samples irradiated with low and high doses increases rapidly with decreasing Larmor frequency. This figure makes clear that the increased relaxation due to the increased polymerization is much more efficient at low fields. The use of the Earth's magnetic field in gel dosimetry makes it therefore possible to apply the polymer gel dosimeter already at very low doses. At those low doses, the relaxation rate at high magnetic fields is hardly changing.

The components with short and long relaxation times can also be better distinguished when they are measured in low magnetic fields. The absolute differences between both components increases with decreasing Larmor frequency (about 71.5 s^{-1} at 3 kHz and about 5.5 s^{-1} at 3 MHz for a dose of 5 Gy). The relative difference between the short and long component at 5 Gy is about 2.5 larger at 3 kHz than at 3 MHz. A comparison between the expected longitudinal relaxation rates at 2 kHz displayed in figure 5.25 and the transversal relaxation rates displayed in figure 5.24 (measured in the Earth's magnetic field, 2050 Hz), shows that $R_1 > R_2$. This is due to the fact that the R_1 dispersions have been measured one month after the T_2 measurements. As shown by Bislich [2007] the relaxation rates of the polymer gels are

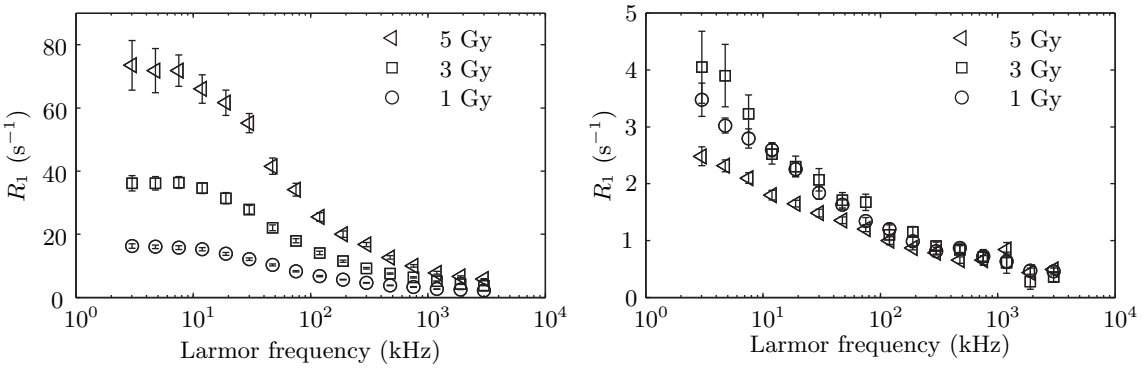

(a) dose dependent component

(b) dose independent component

Figure 5.25: R_1 ($=1/T_1$) in function of the Larmor frequency for the two components of the nMAG gel for 1, 3 and 5 Gy

changing (increasing) slowly with time.

Although not applied in this work, the relaxation dispersion displayed in figure 5.25 could be used to derive the frequency spectrum of the molecule mobility (Fischer [1990]). This could give even more insight into the internal structure of the gel and the processes occurring after irradiation.

Next to the advantage of measuring at very low fields, the good quality of the measurement data obtained by the Earth's field NMR device allows an advanced analysis of the magnetization decays. In the literature, usually a NMR tomograph is used to measure the relaxation times in gel dosimetry applications (e.g. Gore et al. [1984], Maryanski et al. [1993], Maryanski et al. [1994], De Deene et al. [2002], De Deene et al. [2006]). This device is constructed to make contrast rich images, but the accuracy of the relaxation time measurements is not optimal and the data quality does not allow a multi-exponential analysis. A multi-exponential analysis of the data however, makes it possible to distinguish between different regimes in the polymerization and also allows to separate strong from weak dose dependent components. Even if the amplitudes of one component is very small in comparison with the amplitudes of the other one (see figure 5.22), a mono-exponential analysis would lead to completely different results. In figure 5.26 the transversal relaxation data that are analyzed mono-exponentially are compared with the data from the dose dependent component after a multi-exponential analysis. For the mono-exponential analysis, the dose-R_2 sensitivity decreases with increasing dose, and there is no longer a linear relation at larger doses.

In the literature, the decreasing linearity between the applied dose and the relaxation rate at very high doses ($>$ 10 Gy, De Deene et al. [2006]) is usually attributed to the increased termination reactions due to the high concentration of radicals leading to a decreasing dose

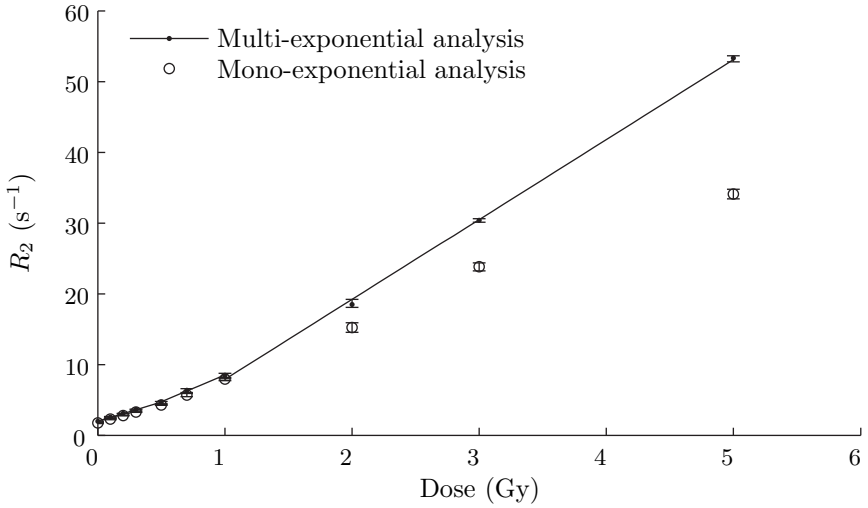

Figure 5.26: R_2 in function of the applied dose for the dose dependent component of a multi-exponential analysis and for a mono-exponential analysis

response. The advanced (multi-exponential) data analysis in this work shows however, that this decreasing linearity could also be magnified by the increasing bi-exponential character of the gel at high doses. Multi-exponential data analysis at low magnetic fields increases thus the region of linearity between the applied dose and the relaxation rate.

Chapter 6

Conclusions and outlook

The experiments in the previous chapter showed that the Earth's field NMR (EFNMR) device can be used in a wide range of applications. Two different sets of experiments were performed: experiments where the measured signal amplitude is analyzed and experiments where the relaxation times are used to derive some information about the environment of the protons.

Because the measured signal amplitude is directly proportional to the spin density within the sample (protons in the case of water), the EFNMR device can be used to determine the water content of bulk water as well as water confined in porous systems. The accuracy of the signal amplitude determination depends on the transversal relaxation time of the system. Using the in-vitro experimental setup the accuracy of the water content determination is very good when $T_2 > 40$ ms; the errors are below 1 % (see figures 5.1, 5.3 and 5.4). With decreasing relaxation times the errors increase due to the dead time of the device of about 8 ms. For samples with $T_2 < 5$ ms it is impossible to derive the correct amplitude (and relaxation time). Not only accuracy but also the signal amplitude itself depends on the relaxation time. This dependence was overcome by normalizing the amplitudes (see Eq. 3.32 to 3.32).

With the in-situ probe head the water content of a sample can be measured independently of its geometry. For a good data quality a few requirements are necessary:

- the water content must be large enough (above 10 %)
- the relaxation times must be large enough (> 10 ms)
- the water must be homogeneously distributed and located close to the coil surface
- the angle between the coil axis and the Earth's magnetic field must be close to 90°

When those requirements are fulfilled, the water content can be determined with an accuracy of about 5 % (see figure 5.5). Although large volumes can be measured, the data quality is

much lower than for the in-vitro probe head because the in-situ probe head has no shielding or shimming and the geometry is not optimal: the sensitive region does not correspond with the region with the highest magnetic induction (coil axis), but is located outside the coil. By moving the in-situ probe head parallel with the coil front side, information about the lateral distribution of the protons below the coil surface can be derived and the NMR device can be used as a surface scanner for proton rich fluids. However, the dependence of the signal amplitude on the direction of the magnetic field makes the signal analysis complicated (see figure 3.19 and 3.20).

By continuously measuring the water content of a sample during a drying process, its drying behavior can be monitored. In this work, Earth's field NMR was used for the first time to study the drying behavior of porous systems. The drying experiments performed with the VitraPOR glass filters showed that the EFNMR device is a very suitable tool to study the drying process in porous systems. Different drying regimes (constant rate, falling rate and receding front period) were distinguished and the dependence of those regimes on the pore size was observed. By using the in-situ coil, drying experiments are not limited to cylindrical geometries, but could be conducted in future experiments with all kinds of samples that fulfill the requirements listed above. Furthermore, by varying the temperature and humidity of the air temperating the sample, the effect of those factors on the drying rate could also be analyzed easily with the EFNMR device.

Next to the water content it is also possible to obtain some information about the environment of the water by analyzing the relaxation times. The EFNMR device is equipped with some unique features such as first order gradiometer polarization and detection coils, shimming coils and a shielding box that make it possible to directly derive the relaxation times from the free induction decay (FID) signal inside a laboratory building with a signal to noise ratio of about 100. The device is able to measure the relaxation times over a wide range, from about 10 ms up to more than 2 s. This is however only true for samples with negligible internal inhomogeneities. Because the relaxation times are directly derived from the FID envelope and no CPMG pulse sequences are applied, the effect of the internal inhomogeneities can not be canceled out and the correct relaxation times can only be derived for systems with low paramagnetic impurities.

For porous samples with a low amount of impurities, the EFNMR technique was used to relate the pore size to the relaxation time. The dependence of the relaxation time on the pore size of water confined in porous systems is predicted by the model of Brownstein and Tarr [1979]. This model was applied to express the transversal and longitudinal relaxation times of porous glasses in function of the pore size, the bulk relaxation time and the relaxivity. Once the latter two parameters are found, the pore size can be derived from the measured relaxation time. The transversal bulk relaxation and surface relaxivity of a set of porous glasses (VitraPOR glass filters) were derived. Those two parameters were then used to determine the pore size

distribution of two unknown porous systems with a chemical composition similar to the glass filters. The pore size distributions that were found by this method were very similar with the pore size distribution determined by mercury intrusion porosimetry (see figure 5.15). Although the relaxivity and bulk relaxation time have to be known in advance, determining the pore size distribution by EFNMR relaxometry has some advantages over mercury intrusion porismetry: it is a non-destructive method that directly determines the surface to volume ratio (no dependence on the pore throats as is the case for mercury intrusion porosimetry). When the bulk relaxation time and the relaxivity are not known, the absolute values of the pore size distribution can not be determined. However, it is still possible to obtain some valuable information about the pore characteristics in this case. Mono-modal porous systems can clearly be discriminated from multi-modal systems and the weighting of different pore fractions can be determined directly from the relaxation time distribution.

The EFNMR device is also capable of measuring the longitudinal relaxation times. By varying the polarization current, T_1 can be measured at different Larmor frequencies (from 3 kHz up to 3 MHz). The determination of the longitudinal relaxation times of the VitraPor filter glasses as a function of the pore size and the Larmor frequency showed that both the relaxivity and the bulk relaxation time of the filter glasses are frequency dependent. The values of the longitudinal relaxation times were only slightly larger then the transversal relaxation time, indicating that the influence of paramagnetic impurities is small for those samples.

The limitations of the measurement method presented in this work, became clear when samples with a high amount of paramagnetic impurities (such as soil samples) were measured. Comparison of the EFNMR data with measurements performed in high magnetic fields (with CPMG pulse sequences) showed that, although lower in low magnetic fields, the influence of paramagnetic impurities within the soil samples are not negligible. The decay of the magnetization in those samples is mainly due to the local inhomogeneities and will strongly depend on the concentration of the paramagnetic impurities. Applying CPMG pulses, which is technically complex in the Earth's magnetic field due to the low Larmor frequencies, would only partially solve the problem since, due to the relatively long dead time (≈ 8 ms) of the EFNMR device, a substantial fraction of the relaxation times ($T_2 < 10$ ms) would be still "invisible" (see figure 5.17) even with CPMG pulses. The EFNMR method is thus only applicable for samples with a low amount of paramagnetic impurities that have relaxation times longer than about 10 ms.

The results of the experiments of the soil samples showed that the original aim of this work, namely analyzing the pore size characteristics of real soil samples, is not possible with the described experimental setup. However, EFNMR can still be used to derive the fluid content accurately in soil samples, as long as $T_2{}^*$ (the time constant describing the signal decay due to relaxation and internal inhomogeneity) is large enough (> 10 ms).

The experiments with polymer gels probably exploited the advantages of Earth's Field NMR in an optimal way:

- Due to the increased relaxation at low fields, the EFNMR is very sensitive for relaxation depending processes (e.g. dose-R_2 sensitivity).
- The good data quality allows a multi-exponential analysis.
- Samples can be temperated with an accuracy of about $\pm 1°C$ so that the temperature influence during the relaxation time measurement can be neglected. By varying the temperature, the influence of the temperature could also be investigated in future experiments.

In this work *NMR relaxography* was used for the first time in the Earth's magnetic field. The transversal relaxation time during a polymerization reaction of two silcagels was continuously measured and the proceeding of the polymerization reaction was visualized in real time. In this way the influence of the pH on the kinetics of the reaction was quantified. The relaxation time is a measure for the mobility of the surrounding water molecules and therefore depends on the polymerization degree of the polymer. The relaxation time distribution could thus be used to obtain information about the molecular weight distribution of polymers solved in proton rich fluids. Absolute values of the molecular weight distribution would be possible after calibration with standards of a known molecular weight.

Especially the first two advantages listed above are very useful in gel dosimetry. Due to the increased relaxation at low fields, it has become possible to measure the effect of relatively low irradiation accurately for the first time by NMR relaxometry. Due to the multi-exponential data analysis, it has become possible to expand the standard data analysis as used at high field applications by distinguishing different dose regimes. By this new analysis method a linear relationship over the whole dose range was obtained. Due to those advantages, EFNMR could be used as an absolute dosimeter that is also capable of measuring relatively low irradiation levels. Furthermore, the main disadvantages that was encountered during the experiments with porous systems (the effect of the paramagnetic impurities on the signal decay) do not play a role anymore since the gel is a chemical pure system, without any unknown substances (impurities). Furthermore, the capability of the EFNMR device to measure T_1 dispersions could be used in future experiments to get a better insight into the internal structure of the gel and the processes occurring after irradiation by analyzing the frequency spectrum of the molecule mobility.

Appendix A

Communication between PC and Earth's field NMR device

The Earth field NMR device can be controlled by a PC via a serial port connection (RS232). For the communication between the device and a PC ASCII character strings (capitals) are used. Such a control string has the following parts:

1. Earth's Field NMR device identification: `MR`
2. A basic command
   - `S`: Set
   - `R`: Read
   - `D`: Do
3. Specific assignation to the basic command (two capitals)
4. Parameter value corresponding to the assignation (only for the basic command `S`)
5. Carriage return ($\langle$`CR`$\rangle = 0A_{hex}$) (optional) and line feed ($\langle$`LF`$\rangle$=$0D_{hex}$)(necessary)

After every correctly received `S`-command, the NMR device executes the command and sends the character string `OK`$\langle$`CR`$\rangle\langle$`LF`$\rangle$to the PC. When the `S`-command with could not be interpreted, the NMR device sends `ER`$\langle$`CR`$\rangle\langle$`LF`$\rangle$.

After every correctly received `R`-command, the NMR device sends the requested parameter together with the comment text, numerical value, unit and the character string $\langle$`CR`$\rangle\langle$`LF`$\rangle$. When the `R`-command could not be interpreted, the NMR device sends the character string `ER` $\langle$`CR`$\rangle\langle$`LF`$\rangle$.

After every correctly received D-command, the NMR device confirms with WT ⟨CR⟩⟨LF⟩. Immediately afterwards the device starts with the execution of the command. When the command is executed (which can take a long time), the NMR device sends OK⟨CR⟩⟨LF⟩. When a D-command could not be interpreted, the device immediately sends ER ⟨CR⟩⟨LF⟩without execution.

The NMR device is ready to receive commands by the serial port when it is in the input mode (i.e. the device is switched on and the last digit of the display is blinking). No commands should be transmitted when the device is not in the input mode, nor should further commands be sent before receiving the return information of the device (OK⟨CR⟩⟨LF⟩or ER⟨CR⟩⟨LF⟩).

When the Earth's field NMR device was built by Goedecke [1993], the controlling and data acquiring was done directly by the microprocessor firmware without the need of an external PC. In this work, a self-written software is used that takes over a part of the calculations and data processing and some parameters are not used anymore. In the following tables the different assignments for the different commands are listed. Commands with * were only used in Goedecke [1993] and are not used in the NMR controlling software in this work:

1. Commands with S to set variables

	MRSNR_ _ _ _	Measurement number
	MRSDT_ _ _ _ _ _	Measurement date (YY/MM/DD)
*	MRSUR _ _ . _ _	Measurement time (HH.MM)
	MRSPO _	Output port (scalar between 0 and 3, always 3 in this work)
	MRSSF _ _ _ _ . _ _	Signal frequency (Hz)
	MRSEF _ _ _ _ . _ _	Calibration frequency (Hz)
	MRSIV _ _ _ _ . _ _	Pre-polarization current (mA)
	MRSTV _ _ . _ _	Pre-polarization time (s)
	MRSIP _ _ _ _ . _ _	Polarization current (mA)
*	MRSPI _	Polarization current table (0 or 1)
	MRSRB _ _ _ _ . _ _	Cut off value for relaxometry mode (mA)
	MRSPD _ _ . _ _	Polarisation time (s)
*	MRSPT _	Polarization time factor table (number between 0 and 4)
	MRSRD _ _ . _ _	Waiting time (s) (Only used by Controlling software)
	MRSBB _	Band width (number between 0 and 2)
	MRSAC _ _ _ _	Output C
	MRSAF _ _ _ _	Output F
*	MRSPU _	Pulse time interval
*	MRSAZ _ _ _ _ _ _	Accumulations per cycle
*	MRSNZ _ _ _ _	Number of accumulations
	MRSNP _ _ _ _ _ _	Number of data points

	MRSDP _ _ . _ _	data point distance (ms) (multiple of 0.25 ms)
*	MRSPA _	T_1 start point (ms)
*	MRSPE _	T_1 end point (ms)
	MRSGA _ _ _ _	Gain
*	MRSTM _	Temperature (°C)
*	MRSAD _ _ _ _	Time before main program A starts (s)
*	MRSI0 _ _ _ _ . _ _	Polarization time 0 (mA)
*	MRSI1 _ _ _ _ . _ _	Polarization time 1 (mA)
*	MRSI2 _ _ _ _ . _ _	Polarization time 2 (mA)
*	MRSI3 _ _ _ _ . _ _	Polarization time 3 (mA)
*	MRSI4 _ _ _ _ . _ _	Polarization time 4 (mA)
*	MRSI5 _ _ _ _ . _ _	Polarization time 5 (mA)
*	MRSI6 _ _ _ _ . _ _	Polarization time 6 (mA)
*	MRSI7 _ _ _ _ . _ _	Polarization time 7 (mA)
*	MRSI8 _ _ _ _ . _ _	Polarization time 8 (mA)
*	MRSI9 _ _ _ _ . _ _	Polarization time 9 (mA)
*	MRSIA _ _ _ _ . _ _	Polarization time 10 (mA)
*	MRSIB _ _ _ _ . _ _	Polarization time 11 (mA)
*	MRSIC _ _ _ _ . _ _	Polarization time 12 (mA)
*	MRSID _ _ _ _ . _ _	Polarization time 13 (mA)
*	MRSIE _ _ _ _ . _ _	Polarization time 14 (mA)
*	MRSIF _ _ _ _ . _ _	Polarization time 15 (mA)
*	MRST0 _ _ _ _ . _ _	Estimated T_1 value 0 (s)
*	MRST1 _ _ _ _ . _ _	Estimated T_1 value 1 (s)
*	MRST2 _ _ _ _ . _ _	Estimated T_1 value 2 (s)
*	MRST3 _ _ _ _ . _ _	Estimated T_1 value 3 (s)
*	MRST4 _ _ _ _ . _ _	Estimated T_1 value 4 (s)
*	MRST5 _ _ _ _ . _ _	Estimated T_1 value 5 (s)
*	MRST6 _ _ _ _ . _ _	Estimated T_1 value 6 (s)
*	MRST7 _ _ _ _ . _ _	Estimated T_1 value 7 (s)
*	MRST8 _ _ _ _ . _ _	Estimated T_1 value 8 (s)
*	MRST9 _ _ _ _ . _ _	Estimated T_1 value 9 (s)
*	MRSTA _ _ _ _ . _ _	Estimated T_1 value 10 (s)
*	MRSTB _ _ _ _ . _ _	Estimated T_1 value 11 (s)
*	MRSTC _ _ _ _ . _ _	Estimated T_1 value 12 (s)
*	MRSTD _ _ _ _ . _ _	Estimated T_1 value 13 (s)
*	MRSTE _ _ _ _ . _ _	Estimated T_1 value 14 (s)
*	MRSTF _ _ _ _ . _ _	Estimated T_1 value 15 (s)

2. Commands with `R` to read variables

```
    MRRNR  gives:  MESSUNG NR.                  =  XXXX
    MRRDT  gives:  DATUM                        =  TT/MM/JJ
*   MRRUR  gives:  UHRZEIT                      =  HH.MM
    MRRPO  gives:  AUSGABEPORT                  =   X
    MRRSF  gives:  SIGNALFREQUENZ               =  XXXX.XX HZ
    MRREF  gives:  EICHFREQUENZ                 =  XXXX.XX HZ
    MRRIV  gives:  VORPOLARISATIONSSTROM        =  XXXX.XX MA
    MRRTV  gives:  VORPOLARISATIONSZEIT         =    XX.XX S
    MRRIP  gives:  POLARISATIONSSTROM           =  XXXX.XX MA
*   MRRPI  gives:  POLSTROM-TABELLE             =     X
    MRRRB  gives:  RELAXOMETERBETRIEB BEI       <  XXXX.XX MA
    MRRPD  gives:  POLZEIT / T1-SCHAETZWERT     =    XX.XX S
*   MRRPT  gives:  POLZEIT-FAKTOR-TABELLE       =     X
    MRRRD  gives:  WARTEZEIT                    =    XX.XX S
    MRRBB  gives:  BANDBREIDTE                  =   XXX.XX HZ
    MRRAC  gives:  AUSGABE C                    =  XXXX
    MRRAF  gives:  AUSGABE F                    =  XXXX
*   MRRPU  gives:  PULSZEITINTERVAL             =    XX    MS
    MRRAZ  gives:  AKKUMULATIONEN/ZYKLUS     = XXXXXX
    MRRNZ  gives:  ZAHL DER AKKUM./ZYKLEN    =   XXXX
    MRRNP  gives:  ZAHL DER MESSPUNKTE       = XXXXXX
    MRRDP  gives:  ABSTAND DER MESSPUNKTE    =     XX.XX MS
*   MRRPA  gives:  T1-ANFAENGSPUNKT             =  XXXX
*   MRRPE  gives:  T1-ENDPUNKT                  =  XXXX
    MRRGA  gives:  HAUPTVERSTAERKER-GAIN        =  XXXX
    MRRTM  gives:  PROBENTEMPERATUR             =    XX   GRD C
    MRRRL  gives:  RAUSCHLEISTUNG            = XXXXXXXX
*   MRRAD  gives:  A-VORLAUFZEIT                =  XXXX

    MRRI0  gives:  I0 = _ _ _ _ . _ _ MA     [Polarizationcurrent 0]
*   MRRI1  gives:  I1 = _ _ _ _ . _ _ MA     [Polarizationcurrent 1]
*   MRRI2  gives:  I2 = _ _ _ _ . _ _ MA     [Polarizationcurrent 2]
*   MRRI3  gives:  I3 = _ _ _ _ . _ _ MA     [Polarizationcurrent 3]
*   MRRI4  gives:  I4 = _ _ _ _ . _ _ MA     [Polarizationcurrent 4]
*   MRRI5  gives:  I5 = _ _ _ _ . _ _ MA     [Polarizationcurrent 5]
*   MRRI6  gives:  I6 = _ _ _ _ . _ _ MA     [Polarizationcurrent 6]
*   MRRI7  gives:  I7 = _ _ _ _ . _ _ MA     [Polarizationcurrent 7]
*   MRRI8  gives:  I8 = _ _ _ _ . _ _ MA     [Polarizationcurrent 8]
```

*	MRRI9	gives:	I9 = _ _ _ _ . _ _ MA	[Polarizationcurrent 9]
*	MRRIA	gives:	IA = _ _ _ _ . _ _ MA	[Polarizationcurrent 10]
*	MRRIB	gives:	IB = _ _ _ _ . _ _ MA	[Polarizationcurrent 11]
*	MRRIC	gives:	IC = _ _ _ _ . _ _ MA	[Polarizationcurrent 12]
*	MRRID	gives:	ID = _ _ _ _ . _ _ MA	[Polarizationcurrent 13]
*	MRRIE	gives:	IE = _ _ _ _ . _ _ MA	[Polarizationcurrent 14]
*	MRRIF	gives:	IF = _ _ _ _ . _ _ MA	[Polarizationcurrent 15]
*	MRRT0	gives:	T0 = _ _ . _ _ S	[Estimated T_1 value 0]
*	MRRT1	gives:	T1 = _ _ . _ _ S	[Estimated T_1 value 1]
*	MRRT2	gives:	T2 = _ _ . _ _ S	[Estimated T_1 value 2]
*	MRRT3	gives:	T3 = _ _ . _ _ S	[Estimated T_1 value 3]
*	MRRT4	gives:	T4 = _ _ . _ _ S	[Estimated T_1 value 4]
*	MRRT5	gives:	T5 = _ _ . _ _ S	[Estimated T_1 value 5]
*	MRRT6	gives:	T6 = _ _ . _ _ S	[Estimated T_1 value 6]
*	MRRT7	gives:	T7 = _ _ . _ _ S	[Estimated T_1 value 7]
*	MRRT8	gives:	T8 = _ _ . _ _ S	[Estimated T_1 value 8]
*	MRRT9	gives:	T9 = _ _ . _ _ S	[Estimated T_1 value 9]
*	MRRTA	gives:	TA = _ _ . _ _ S	[Estimated T_1 value 10]
*	MRRTB	gives:	TB = _ _ . _ _ S	[Estimated T_1 value 11]
*	MRRTC	gives:	TC = _ _ . _ _ S	[Estimated T_1 value 12]
*	MRRTD	gives:	TD = _ _ . _ _ S	[Estimated T_1 value 13]
*	MRRTE	gives:	TE = _ _ . _ _ S	[Estimated T_1 value 14]
*	MRRTF	gives:	TF = _ _ . _ _ S	[Estimated T_1 value 15]

3. Commands with D to execute commands. (The programs used in this work are explained in section 3.4.4)

	H9	Main program 9	single FID with recording of the amplitude
*	HA	Main program A	T_1/T_2 measurement
	HB	Main program B	continuous determination of the Larmor frequency
*	HD	Main program D	output of the measurement parameter
	HE	Main program E	tuning
	HF	Main program F	determination of the Larmor frequency
*	Z3	Sub program 3	data output after main program A
	Z4	Sub program 4	data output after main program B
	Z5	Sub program 5	noise determination
	Z9	Sub program 9	data output after main program 9

Bibliography

Abragam, A. (1973). *The principles of nuclear magnetism*. International series of monographs on physics. Clarendon Press, Oxford, reprinted edition.

Appelo, C. A. J. and Postma, D. (1999). *Geochemistry, groundwater and pollution*. Balkema, Rotterdam, 4., corr. print edition.

Appelt, S., Hasing, F. W., Kuhn, H., Perlo, J., and Blumich, B. (2005). Mobile high resolution xenon nuclear magnetic resonance spectroscopy in the Earth's magnetic field. *Physical Review Letters*, 94(19):197602 – 4.

Appelt, S., Kuhn, H., Hasing, F. W., and Blumich, B. (2006). Chemical analysis by ultrahigh-resolution nuclear magnetic resonance in the Earth's magnetic field. *Nature Physics*, 2(2):105 – 109.

Bene, G. J. (1980). Nuclear magnetism of liquid systems in the Earth field range. *Physics Reports*, 58(4):213 – 267.

Berckhemer, H. (2005). *Grundlagen der Geophysik*. Institut für Meteorologie und Geophysik, Frankfurt a.M.

Berger, W. and Butterweck, H. (1956). Die Berechnung von Spulen zur Erzeugung homogener Magnetfelder und konstanter Feldgradienten. *Electrical Engineering (Archiv für Elektrotechnik)*, 42(4):216 – 222.

Bislich, O. (2007). NMR-Polymergeldosimetrie ionisierender Strahlung im Erdmagnetfeld. Master's thesis, University of Bremen, Germany.

Bloch, F., Hansen, W. W., and Packard, M. (1946). The nuclear induction experiment. *Physical Review*, 70(7-8):474.

Bloembergen, N. (1957). Proton relaxation times in paramagnetic solutions. *The Journal of Chemical Physics*, 27(2):572 – 573.

Bloembergen, N., Purcell, E., and Pound, R. (1948). Relaxation effects in nuclear magnetic resonance absorption. *Physical Review*, 73(7):679 – 712.

Bloom, A. and Mansir, D. (1954). Measurement of nuclear induction relaxation times in weak magnetic fields. *Physical Review*, 93:941.

Bronstein, I. and Semendjajew, K. (1981). *Taschenbuch der Mathematik*. Verlag Harri Deutsch, Frankfurt am Main, Thun, 20. edition.

Brown, R. J. S. and Fantazzini, P. (1993). Conditions for initial quasilinear $1/T_2$ versus τ for Carr-Purcell-Meiboom-Gill NMR with diffusion and susceptibility differences in porous media and tissues. *Physical review B*, 47:14823 – 14834.

Brownstein, K. and Tarr, C. (1979). Importance of classical diffusion in NMR studies of water in biological cells. *Physical Review A*, 19(6):2446–2553.

Bruvold, M., Seland, J., Brurok, H., and Jynge, P. (2007). Dynamic water changes in excised rat myocardium assessed by continuous distribution of T_1 and T_2. *Magnetic Resonance in Medicine*, 58(2):442–447.

Butler, J., Reeds, J., and Dawson, S. (1981). Estimating solutions of first kind integral equations with nonnegative constraints and optimal smoothing. *SIAM Journal on Numerical Analysis*, 18(3):381–397.

Callaghan, P., Dykstra, R., Eccles, C., Haskell, T., and Seymour, J. (1999). A nuclear magnetic resonance study of Antarctic sea ice brine diffusivity. *Cold regions Science and Technology*, 29(2):153–171.

Callaghan, P., Eccles, C., Haskell, T., Langhorne, P., and Seymour, J. (1998). Earth's field NMR in Antarctica: a pulsed gradient spin echo NMR study of restricted diffusion in sea ice. *Journal of Magnetic Resonance*, 133:148–154.

Callaghan, P., Eccles, C., and Seymour, J. (1997). An Earth's field nuclear magnetic resonance apparatus suitable for pulsed gradient spin echo measurements of self-diffusion under Antarctic conditions. *Review of Environmental Scientific Instruments*, 68(11):4263–4270.

Callaghan, P. and Le Gros, M. (1982). Nuclear spins in the Earth's magnetic field. *American Journal of Physics*, 50(8):709 – 713.

Carr, H. and Purcell, E. (1954). Effects of diffusion on free precession in nuclear magnetic resonance experiments. *Americal Journal of Physics*, 94(3):630–638.

Chen, Q., Gingras, M., and Balcolm, B. (2003). A magnetic resonance study of pore filling processes during spontaneous imbibition in Berea sandstone. *The Journal of Chemical Physics*, 119(18):9609–9619.

Chen, Q., Marble, A. E., Colpitts, B. G., and Balcom, B. J. (2005). The internal magnetic field distribution, and single exponential magnetic resonance free induction decay, in rocks. *Journal of Magnetic Resonance*, 175(2):300 – 308.

De Deene, Y., Hurley, C., Venning, A., Vergote, K., Mather, M., Healy, B., and Baldock, C. (2002). A basic study of some normoxic polymer gel dosimeters. *Physics in Medicine and Biology*, 47(19):3441–3463.

De Deene, Y., Vergote, K., Claeys, C., and Wagter, C. D. (2006). The fundamental radiation properties of normoxic polymer gel dosimeters: a comparison between a methacrylic acid based gel and acrylamide based gels. *Physics in Medicine and Biology*, 51(3):653 – 673.

D'Orazio, F., Tarczon, J., Halperin, W. P., Eguchi, K., and Mizusaki, T. (1989). Application of nuclear magnetic resonance pore structure analysis to porous silica glass. *Journal of Applied Physics*, 65(2):742–750.

Doskocilova, D., Tao, D., and Schneider, B. (1975). Effects of macroscopic spinning upon linewidth of NMR signals of liquid in magnetically inhomogeneous systems. *Czechoslovak Journal of Physics*, 25(2):202 – 209.

Eidmann, G., Savelsberg, R., Blümler, P., and Blümich, B. (1996). The NMR MOUSE: A mobile universal surface explorer. *Journal of Magnetic Resonance A*, 122:104–109.

Fantazzini, P., Salem, A., Timellini, G., Tucci, A., and Viola, R. (2003). Microstructure changes in fired ceramics quantified by magnetic resonance relaxation and imaging. *Journal of Applied Physics*, 94(8):5337 – 5342.

Farrar, T. C. and Becker, E. D. (1974). *Pulse and fourier transform NMR.* Academic Press, New York, 2 edition.

Favre, B., Bonhe, J., Mehier, H., and Peyrin, J. (1990). Environmental optimization and shielding for NMR experiments and imaging in the Earth's magnetic field. *Magnetic Resonance in Medicine*, 13(2):299 – 304.

Fischer, H. (1990). *NMR - Relaxationsspektroskopische Untersuchungen von tierischen und menschlichen Gewebeproben.* Univ. Bremen, Diss., Bremen.

Florokowski, Z., Hennel, J., and Blicharska, B. (1969). An apparatus for measuring proton spin relaxation time in low magnetic fields. *Nukleonika*, 14:563–569.

Fordham, E., Sezginer, A., and Hall, L. (1995). Imaging multiexponential relaxation in the (y, $\mathrm{Log_e T_1}$) plane, with application to clay filtration in rock cores. *Journal of Magnetic Resonance, Series A*, 113(2):139 – 150.

Fukushima, E. and Roeder, S. B. (1981). *Experimental pulse NMR*. Addison-Wesley, Reading, Mass.

Godefroy, S., Korb, J.-P., Fleury, M., and Bryant, R. (2001). Surface nuclear magnetic relaxation and dynamics of water and oil in macroporous media. *Physical Review E*, 64(2):021605.

Goedecke, R. (1993). *Entwicklung und Optimierung einer Kernresonanzapparatur unter Verwendung des Erdmagnetfeldes für biophysikalische und medizinische Fragestellungen*. Univ. Bremen, Diss., Bremen.

Goedecke, R. and von Boetticher, H. (1999). Erdfeld-NMR: Apparative Entwicklungen zur in-vivo Analyse von Körperflüssiggkeiten und weichem Gewebe. *Zeitschrift für Medizinische Physik*, 9:130–138.

Gore, J., Kang, Y., and Schulz, R. (1984). Measurement of radiation dose distributions by nuclear magnetic resonance nmr imaging. *Physics in Medicine and Biology*, 29(10):1189–1197.

Gultekin, D. H. and Gore, J. C. (2005). Temperature dependence of nuclear magnetization and relaxation. *Journal of Magnetic Resonance*, 172(1):133–141.

Halperin, W., D'Orazio, F., Bhattacharja, S., and Tarczon, J. (1989). *Magnetic Resonance Relaxation Analysis of Porous Media*. John Wiley & Sons, New York.

Halse, M. E., Coy, A., Dykstra, R., Eccles, C., Hunter, M., Ward, R., and Callaghan, P. T. (2006). A practical and flexible implementation of 3D MRI in the Earth's magnetic field. *Journal of Magnetic Resonance*, 182(1):75 – 83.

Hansen, P. C. (1994). REGULARIZATION TOOLS: A Matlab package for analysis and solution of discrete ill-posed problems. *Numerical Algorithms*, 6(1):1 – 35.

Heckman, J. J., Ledbetter, M. P., and Romalis, M. V. (2003). Enhancement of SQUID-detected NMR signals with hyperpolarized liquid ^{129}Xe in a 1 μT magnetic field. *Physical Review Letters*, 91(6):067601.

Holly, R., Peemoeller, H., Choi, C., and Pintar, M. M. (1998). Proton rotating frame spin-lattice relaxation study of slow motion of pore water. *The Journal of Chemical Physics*, 108(10):4183 – 4188.

Hurlimann, M. D. (1998). Effective gradients in porous media due to susceptibility differences. *Journal of Magnetic Resonance*, 131(2):232 – 240.

Hüsing, N. and Schubert, U. (1998). Aerogels - airy materials: chemistry, structure, and properties. *American Journal of Physics*, 37(1-2):22–45.

Jackson, A. (2000). Critical time for fluid dynamos. *Nature*, 405(6790):1003 – 1004.

Jaeger, F., Grohmann, E., and Schaumann, G. (2006). 1H NMR relaxometry in natural humous soil samples: Insights in microbial effects on relaxation time distributions. *Plant and Soil*, 280(1):209 – 222.

James, F. and Roos, M. (1975). Minuit - a system for function minimization and analysis of the parameter errors and correlations. *Computer Physics Communications*, 10(6):343 – 367.

Kimmich, R. (2002). Strange kinetics, porous media, and NMR. *Chemical Physics*, 284(1-2):253 – 285.

Kleinberg, R., Kenyon, W., and Mitra, P. P. (1994). Mechanism of NMR relaxation of fluids in rock. *Journal of Magnetic Resonance, Series A*, 108(2):206 – 214.

Kleinberg, R. L. (1996). Utility of NMR T_2 distributions, connection with capillary pressure, clay effect, and determination of the surface relaxivity parameter ρ_2. *Magnetic Resonance Imaging*, 14(7-8):761 – 767.

Kleinberg, R. L. and Horsfield, M. A. (1990). Transverse relaxation processes in porous sedimentary rock. *Journal of Magnetic Resonance (1969)*, 88(1):9 – 19.

Koch, D., Andresen, L., Schmedders, T., and Grathwohl, G. (2003). Evolution of porosity by freeze casting and sintering of sol-gel derived ceramics. *Journal of Sol-Gel Science and Technology*, 26(1):149 – 152.

Lagarias, J. C., Reeds, J. A., Wright, M. H., and Wright, P. E. (1998). Convergence properties of the Nelder-Mead Simplex method in low dimensions. *SIAM Journal on Optimization*, 9(1):112 – 147.

Latour, L. L., Kleinberg, R. L., and Sezginer, A. (1992). Nuclear magnetic resonance properties of rocks at elevated temperatures. *Journal of Colloid and Interface Science*, 150(2):535 – 548.

Laurindo, J. and Prat, M. (1998). Numerical and experimental network study of evaporation in capillary porous media. Drying rates. *Chemical Engineering Science*, 53(12):2257 – 2269.

Le Bray, Y. and Prat, M. (1999). Three-dimensional pore network simulation of drying in capillary porous media. *International Journal of Heat and Mass Transfer*, 42(22).

Linnow, K., Juling, H., and Steiger, M. (2007). Investigation of NaCl deliquescence in porous substrates using RH-XRD. *Environmental Geology*, 52(2):317 – 327.

Manalo, F., Kantzas, A., and Langford, C. (2003). Soil wettability as determined from using low-field nuclear magnetic resonance. *Environmental Science and Technology*, 37(12):2701–2706.

Manz, B., Coy, A., Dykstra, R., Eccles, C.D.and Hunter, M., Parkinson, B., and Callaghan, P. (2006). A mobile one-sided NMR sensor with a homogeneous magnetic field: The NMR-MOLE. *Journal of Magnetic Resonance*, 183(1):25–31.

Maryanski, M., Gore, J., Kennan, R., and Schulz, R. (1993). NMR relaxation enhancement in gels polymerized and cross-linked by ionizing radiation: A new approach to 3D dosimetry by MRI. *Magnetic Resonance Imaging*, 11(2):253–258.

Maryanski, M., Schulz, R., Ibbott, G., Gantenby, J., Xie, J., Horton, D., and Gore, J. (1994). Magnetic resonance imaging of radiation dose distributions using a polymer-gel dosimeter. *Physics in Medicine and Biology*, 39(9):1437–1455.

Mattea, C., Kimmich, R., Ardelean, I., Wonorahardjo, S., and Farrher, G. (2004). Molecular exchange dynamics in partially filled microscale and nanoscale pores of silica glasses studied by field-cycling nuclear magnetic resonance relaxometry. *The Journal of Chemical Physics*, 121(21):10648 – 10656.

Meiboom, S. and Gill, D. (1958). Modified spin-echo method for measuring nuclear relaxation times. *Review of Scientific Instruments*, 29(8):688 – 691.

Metzger, T. and Tsotsas, E. (2005). Influence of pore size distribution on drying kinetics: A simple capillary model. *Drying Technology*, 23(9):1797 – 1809.

Meyer, C. (2000). *Matrix Analysis and Applied Linear Algebra*. SIAM, Philadelphia, PA.

Meyer, H.-J. (1984). Schirmungsprobleme bei der medizinischen Anwendung der magnetischen Kernresonanz unter Anwendung des Free Induction Decay und der Spin-Echo-Methoden in schwachen Magnetfeldern. Master's thesis, University of Bremen, Germany.

Mohoric, A., Stepisnik, J., Kos, M., and Planinsic, G. (1999). Self-diffusion imaging by spin echo in Earth's magnetic field. *Journal of Magnetic Resonance*, 136(1):22 – 26.

Nelder, J. and Mead, R. (1965). A Simplex-method for function minimization. *Computer Journal*, 7(4):308–313.

Packard, M. and Varian, R. (1954). Free nuclear induction in the Earth's magnetic field. *The Physical Review*, 93:941.

Pel, L. and Landman, K. A. (2004). A sharp drying front model. *Drying Technology*, 22(4):637 – 647.

Planinsic, G., Stepisnik, J., and Kos, M. (1994). Relaxation-time measurement and imaging in the Earth's magnetic field. *Journal of Magnetic Resonance, Series A*, 110(2):170–174.

Powles, J. G. and Cutler, D. (1957). Audio-frequency nuclear-resonance echoes. *Nature*, 180(4598):1344 – 1345.

Press, W. H., Teukolsky, S. A., Vetterling, W. T., and Flannery, B. P. (2002). *Numerical Recipes in C - The Art of Scientific Computing*. Cambridge University Press, Cambridge, second edition.

Provencher, S. W. (1982a). A constrained regularization method for inverting data represented by linear algebraic or integral equations. *Computer Physics Communications*, 27(3):213 – 227.

Provencher, S. W. (1982b). CONTIN: A general purpose constrained regularization program for inverting noisy linear algebraic and integral equations. *Computer Physics Communications*, 27(3):229 – 242.

Purcell, E. M., Torrey, H. C., and Pound, R. V. (1946). Resonance absorption by nuclear magnetic moments in a solid. *Physical Review*, 69(1-2):37.

Roberts, P., McDonald, P., and Pritchard, T. (1995). A bulk and spatially resolved NMR relaxation study of sandstone rock plugs. *Journal of Magnetic Resonance, Series A*, 116(2):189 – 195.

Robinson, J. N., Coy, A., Dykstra, R., Eccles, C. D., Hunter, M. W., and Callaghan, P. T. (2006). Two-dimensional NMR spectroscopy in Earth's magnetic field. *Journal of Magnetic Resonance*, 182(2):343 – 347.

Rocard, J. (1957). Contribution a l'étude de la résonance paramagnétique nucléaire dans les champs très faibles. *Archives des sciences de la Société de Physique et d'Histoire naturelle de Genève*, 10(3):377–428.

Schlunder, E. U. (2004). Drying of porous material during the constant and the falling rate period: A critical review of existing hypotheses. *Drying Technology*, 22(6):1517 – 1532.

Slijkerman, W. F. J. and Hofman, J. P. (1998). Determination of surface relaxivity from NMR diffusion measurements. *Magnetic Resonance Imaging*, 16(5-6):541 – 544.

Song, Y.-Q., Venkataramanan, L., and Burcaw, L. (2005). Determining the resolution of Laplace inversion spectrum. *The Journal of Chemical Physics*, 122(10):104104 – 8.

Stapf, S., Kimmich, R., and Seitter, R.-O. (1995). Proton and deuteron field-cycling NMR relaxometry of liquids in porous glasses: Evidence for Levy-walk statistics. *Physical Review Letters*, 75(15):2855.

Stepisnik, J. (2006). Spectroscopy: NMR down to Earth. *Nature*, 439(7078):799 – 801.

Stepisnik, J., Kos, M., Planinsic, G., and Erzen, V. (1994). Strong non-uniform magnetic field for self-diffusion measurement by NMR in Earth's magnetic field. *Journal of Applied Magnetic Resonance, Series A*, 107(2):167–172.

Thiele, C. (2007). Magnetic resonance at or below the Earth's magnetic field. *Angewandte Chemie International Edition*, 46(26):4820 – 4824.

Torrey, H. C. (1956). Bloch equations with diffusion terms. *Phys. Rev.*, 104(3):563–565.

Wilkinson, D., Johnson, D., and Schwartz, L. (1991). Nuclear magnetic relaxation in porous media: The role of the mean lifetime. *Physical Review B*, 44(10):4960–4973.

Yiotis, A., Tsimpanogiannis, I., Stubos, A., and Yortsos, Y. (2006). Pore-network study of the characteristic periods in the drying of porous materials. *Journal of Colloid and Interface Science*, 297(2):738 – 748.

Zavada, T. and Kimmich, R. (1998). The anomalous adsorbate dynamics at surfaces in porous media studied by nuclear magnetic resonance methods. The orientational structure factor and Levy walks. *The Journal of Chemical Physics*, 109(16):6929 – 6939.

.